CORROSION OF COPPER IN DEAERATED DEIONIZED WATER AND
GEOMETRY INDUCED FREQUENCY DISPERSION OF THE RING ELECTRODE

By

CHRISTOPHER N. CLEVELAND

A DISSERTATION PRESENTED TO THE GRADUATE SCHOOL
OF THE UNIVERSITY OF FLORIDA IN PARTIAL FULFILLMENT
OF THE REQUIREMENTS FOR THE DEGREE OF
DOCTOR OF PHILOSOPHY

UNIVERSITY OF FLORIDA

2017

I dedicate this to my family and friends.

ACKNOWLEDGMENTS

TABLE OF CONTENTS

CHAPTER

LIST OF TABLES

7

LIST OF FIGURES

Abstract of Dissertation Presented to the Graduate School
of the University of Florida in Partial Fulfillment of the
Requirements for the Degree of Doctor of Philosophy

CORROSION OF COPPER IN DEAERATED DEIONIZED WATER AND
GEOMETRY INDUCED FREQUENCY DISPERSION OF THE RING ELECTRODE

By

Christopher N. Cleveland

May 2017

Chair: Mark E. Orazem
Major: Chemical Engineering

Copper is commonly regarded to be immune to corrosion in deaerated deionized electrolytes. The present work shows that, in the absence of hydrogen, copper will corrode on the order of 1 nm/day in deionized water with an O_2 concentration on the order of, or less than, 1 ppb. While a corrosion rate of this magnitude can normally be neglected, it may be catastrophic for nanoscale copper structures utilized in emerging applications to enhance energy transport at the solid-electrolyte interface, such as in cooling advanced electronics. This conclusion is supported by a set of experimental and analytical studies that encompass impedance spectroscopy, slow-scan linear sweep voltammetry, thermodynamic calculations for the environment under study, and kinetic simulations. The studies provide a comprehensive insight on details of the corrosion mechanism for copper in deaerated water.

An extended kinetic model is developed and used to study the cumulative corrosion rate of copper after 15 years for a microelectrode and for bulk copper. The parameters varied for this study were the area to volume ratio, copper and hydrogen mass-transfer coefficients, equilibrium potentials and exchange current densities. After less than 60 days, the bulk copper in a closed system reached a limiting hydrogen partial pressure of 0.096 atm; whereas, the microelectrode continued to evolve hydrogen over the 15 years, reaching a value of 0.0013 atm. The corrosion rate for the bulk copper was calculated to be 0.35 nm/day and dropped precipitously to zero in less than 60 days; whereas, the

calculated corrosion rate for the microelectrode was 1.1 nm/day and gradually reached a value of 0.74 nm/day after 15 years.

Simulations performed using a refined kinetic model for a microelectrode,[1] validate the assumption that the hydrogen oxidation reaction can be neglected for the small electrode area to volume ratio and short times considered. The hydrogen oxidation reaction played an essential role in simulating the behavior of the bulk copper experiments[2] with its larger electrode area to volume ratio and longer exposure time. For both the open and closed systems, the cumulative corrosion was reduced for larger electrode area to volume ratios. The difference in estimated corrosion rates between the copper microelectrode[1] and the Hultquist et al.[2] bulk copper experiments is shown in the present work to be the natural consequence of the manner in which kinetics, mass transfer, and electrode area to volume ratio influence the progression towards the equilibrium condition.

A 2-D axisymmetric mathematical model was developed to investigate frequency dispersion in a ring electrode. The finite element software COMSOL Multiphysics was used to solve Laplace's equation in cylindrical coordinates for the ring electrode with an applied perturbation potential as the boundary condition. Due to the singularities that arise near the ring electrode's edges, a nonuniform meshing scheme was implemented near the surface of the ring electrode. The presence of frequency dispersion is seen at frequencies greater than the dimensionless frequency equal to unity. The characteristic length for the ring electrode is shown to be a function of the geometric ratio of the inner to outer radius.

CHAPTER 1
INTRODUCTION

Managing the thermal dissipation in microelectronics found in consumer PCs, laptops, radar systems and satellites has become increasingly more difficult as the size transistor decreases and the proximity to one another becomes more compact. Traditional heat sinks such as the one seen in Figure 1-1 perform well, providing a sufficient heat flux removal for the microelectronic devices to maintain operation,[3] but are simply too large for the spatially constrained microelectronic packaging schemes of today. Innovations are required that dissipate the same power density but with less thermal resistance.[4] Over the past decade, a number of microstructures, nanostructures and various combinations of both have been implemented as wicks to address the heat generated from high-powered electronics.

Copper micro/nanowicks hybrid structure accomplish this by providing a significant pressure drop, lowering the permeability and resulting in a greater heat removal when compared to traditional heat sinks. A schematic representation of a two-phase heat sink is provided in Figure 1-2. The electronic component acting as a heat source is located at the bottom of the system seen in Figure 1-2. The coolant passively wicks the fluid towards hot electronic source by capillary forces. As the coolant is heated it begins to evaporate. The vapor phase is forced away from the central heating source where it begins to cool and eventually condenses.

Copper nanostructures structures are known to degrade in performance with time. Since the cooling performance of a copper surface is intricately related to how the liquid-vapor interface forms and how well the fluid flows through a structure,[5] preventative measures must be taken to ensure corrosion-based structural degradation does not occur. Report by Ju,[6] microfluidic channels used in a two-phase cooling system became less effective over time due to corrosion of the channel wall. The tendency for corrosion to
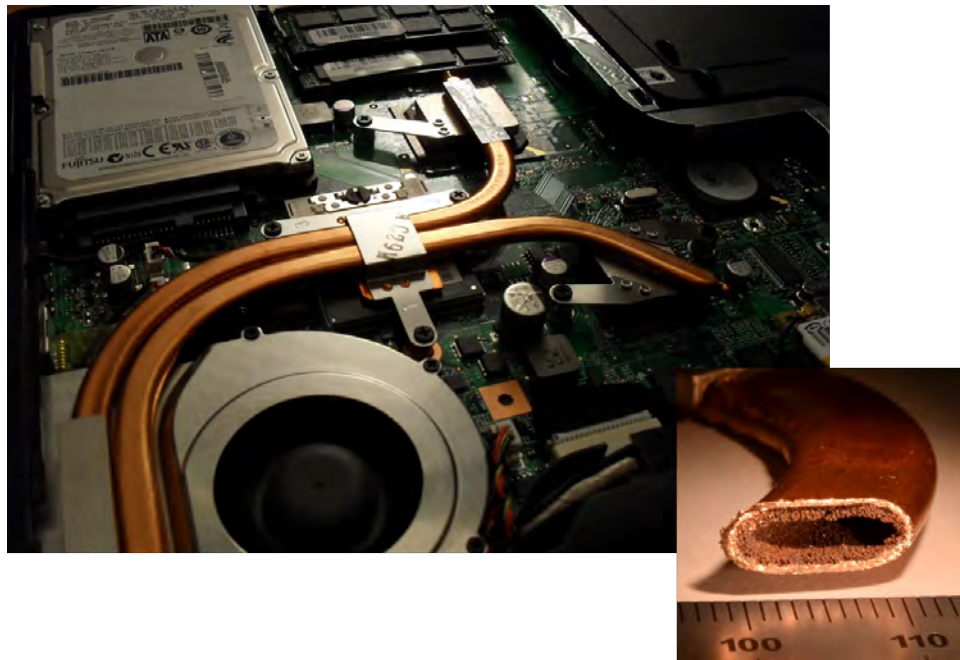
Figure 1-1. Heat sink found in consumer personal computers. Cross-sectional area depicting the copper sponge matrix within the heat pipe. *(Source: Kristoferb, en.wikipedia.org/wiki/Heat_pipe)*
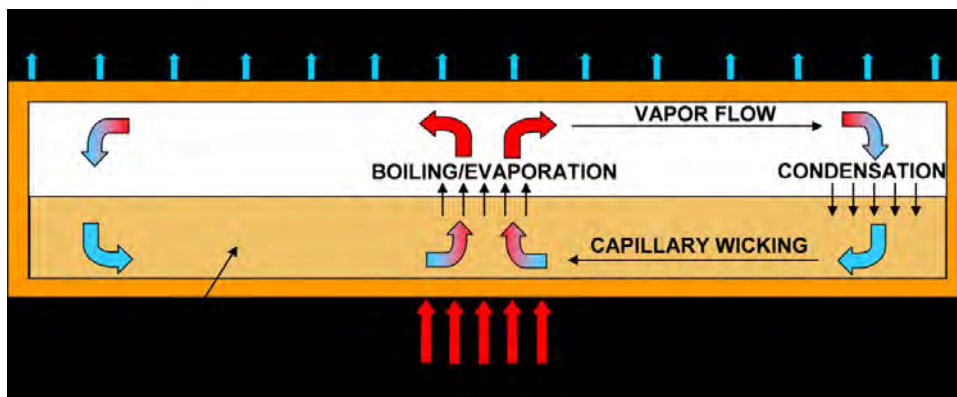
Figure 1-2. Schematic of a hybrid micro/nano wick cooling system. *(Source: School of Mechanical Engineering, Purdue University)*

occur in these copper cooling systems can be detrimental to performance and could eventually lead to a catastrophic failure if not considered outright.

The motivation for this work arises from the need for a better understanding of copper corrosion in deaerated deionized water and is the primary focus of this work discussed in Chapters 2 through 6. In Chapter 2, potential modes of copper corrosion are introduced for the nanowick heat sink. Next, is a literature review describing the role different media has on how quickly copper corrodes. Relevance to the nuclear waste industry with some of the prevailing controversy surrounding the issue is raised at final pages of Chapter 2.

A better understanding of copper corrosion has been gained with the aid of electrochemical techniques. Of particular importance is the application of a technique known as electrochemical impedance spectroscopy (EIS). Chapter 3 provides an overview of the theory behind EIS. An example is presented to demonstrate the need to distinguish the Faradaic and charging current when interpreting the impedance response.

The experimental procedure, electrochemical techniques to quantify corrosion of copper in pure deaerated water, thermodynamic simulations, kinetic simulations, and interpretation of impedance response are presented in Chapter 4. The experimental techniques employed in this study include impedance spectroscopy and linear sweep voltammetry. From these measurements, corrosion rates were determined and further validated with the use of kinetic modeling, and thermodynamic simulations.

A refined kinetic model is presented in Chapter 5 to explore the influence mass transfer, surface area to volume ratio, exchange current density and equilibrium potential have on the corrosion of copper in deaerated water. To explore the influence of system parameters, the simulations presented in Chapter 5 are extended in Chapter 6 to include the oxidation of hydrogen and diffusion of dissolved hydrogen away from the electrode surface.

Electrode geometry has been demonstrated to cause frequency dispersion in the electrochemical impedance response for various systems of different electrode geometry. Chapter 6 provides development of a relation for the characteristic dimension associated with the impedance response of a ring electrode. Emphasis on the frequency dispersion that is caused by the ring electrode and the characteristic dimension will allow prediction of the frequency at which dispersion is seen. Edge effects from a nonuniform current distribution will be considered for primary resistance and impedance. Identification of a characteristic dimension can be used to avoid frequency dispersion in a carefully chosen system matching a set of parameters.

Chapter 7 contains concluding remarks for each of the chapters presented. In Chapter 8 future work is proposed that can be carried out for copper corrosion and geometry induced frequency dispersion.

CHAPTER 2
REVIEW OF COPPER CORROSION

2.1 Copper Nano-Structures at Risk of Corrosion

Copper nanowicks, in the presence of an ion-free deaerated electrolyte, is often considered to be thermodynamically stable and therefore should not corrode. However, it has been reported[7] that copper microcrystalline and nanocystalline structures will corrode under various conditions. In fact, deaerated water may play a larger role in copper corrosion than previous thought. Using electrochemical impedance spectroscopy this chapter explores the extent to which corrosion is occurring, under what conditions it occurs, and then proposes a novel method for minimizing or eliminating the corrosion while maintaining or improving upon the thermal and capillary efficiency of the copper nanowicks.

2.1.1 Copper Nano Wicks

Managing the thermal dissipation in microelectronic processors found in consumer PCs, laptops, radar systems and satellites has become increasingly more difficult. Traditional heat sinks perform well, providing a sufficient heat flux removal for the microelectronic devices to maintain operation, but are simply too large.[3] Innovations are required that dissipate the same power density but with a resistance less thermal resistance.[4] Nanowicks accomplish this by producing a significant pressure drop, lowering the permeability and resulting in an increased heat removal when compared to traditional heat sinks. Hybrid micro/nanoscale wick structures can be used to provide ample heat flux removal by their two phase cooling system.

Figure 2-1A depicts a micropillar array attached to a plate in contact with the liquid phase fluid. Helical hybrid structures used to achieve enhanced heat removal A) 3D CAD rendered side view of Cu nano wicks; and B) SEM side view of regular helical Si grown on a tungsten surface.[3] Attached to each micropillar is a helical structure. It is
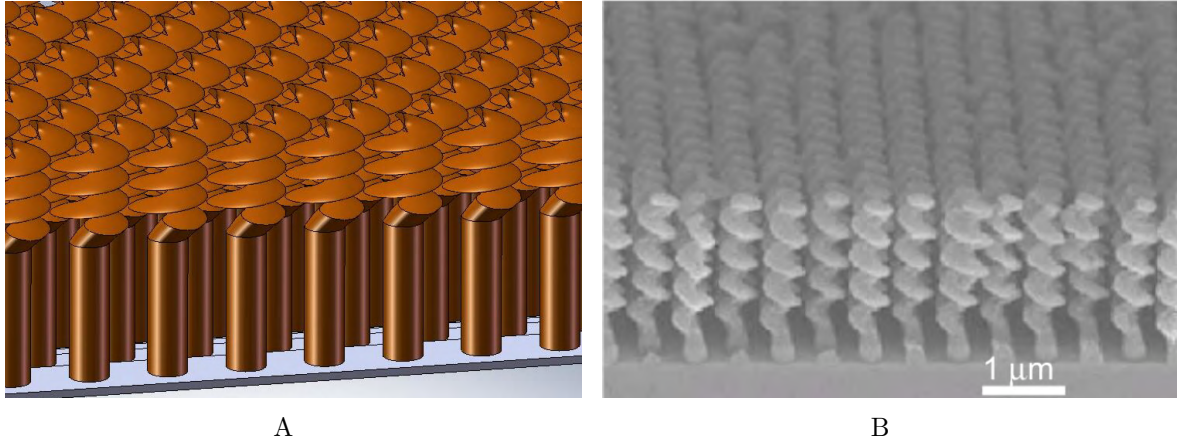
Figure 2-1. Helical hybrid structures used to achieve enhanced heat removal: A) 3D CAD rendered schematic side view of Cu nano wicks; and B) SEM side view of regular helical Si grown on a tungsten surface.[3] *(Source: Photo courtesy of author.)*

generally understood that a hybrid wick structure will achieve superior mass transport when compared to that of homogenous micropillar array wicks.

2.1.2 Uniform Corrosion

Uniform corrosion occurs when the metal is not immune but partially resistant to attack at the surface. In this mode of corrosion, the metal surface undergoes corrosion at a uniform rate. As a result, all of the exposed area of the metal is equally susceptible to corrosion. At the surface of the metal there are spatially separated local anodic and cathodic sites where both oxidation and reduction occur simultaneously. The net current of the system is equal to zero but the reaction is not equilibrated which provides a sufficient potential difference for the electrochemical reaction to occur. In the absence of oxygen, the reactions involve anodic dissolution of copper

$$Cu \rightarrow Cu^{2+} + 2e^{-} \tag{2-1}$$

and water reduction at the cathode,

$$H_2O + e^{-} \rightarrow \frac{1}{2}H_2 + OH^{-} \tag{2-2}$$

These equations represent the two competing reaction required for uniform copper corrosion.

2.1.3 Galvanic (Coupling) Corrosion

It is commonly observed that when two or more metals are electrically connected in an electrolyte, the less noble metal corrodes rapidly.[8] This phenomena is known as galvanic corrosion and occurs when there exists a potential difference between the two or more dissimilar metals. Galvanic corrosion is frequently observed in places such as chemical plants, residential homes and offshore platforms. A notable example is described by Fontana[9] where a yacht containing a Monel hull affixed by steel rivets undergoes rapid corrosion of the rivets.

Not as commonly observed is the potential difference occurring between two of the same metals having nearly the same composition yet different metallurgical properties. Pantazopoulos[10] attributes the leakage of a copper water tube at the elbow to fatigue cracking induced by stress.

2.1.4 Electrokinetic-Current Corrosion

The erosivity of the components found in high pressure hydraulic systems of airplanes was initially attributed to simple wear and tear. It was later discovered that when fluids are forced through channels a streaming potential is formed. The streaming potential provides an adequate driving force for corrosion at the fluid-surface interface. The Electric double layer streaming potential shown on a nanowick. As the fluid moves up by capillary forces (wicking), the depletion of cations at the base of the device results in a corrosion reaction necessary to replenish the cations. Copper nanowicks have a (-) charge is provided in Figure 2-2. As the fluid traverses the diffuse double layer, ions are swept away to the bulk faster than they can be replenished by the walls surface. The depletion of ions resulting from shear variation is sufficient to produce an electrical current at the metal-fluid interface thus corroding the metal surface.

$$\text{Cu}^{2+} + 2\text{e}^- \rightarrow \text{Cu}$$

Excess of Cations

Depletion of Cations

$$\text{Cu} \rightarrow \text{Cu}^{2+} + 2\text{e}^-$$
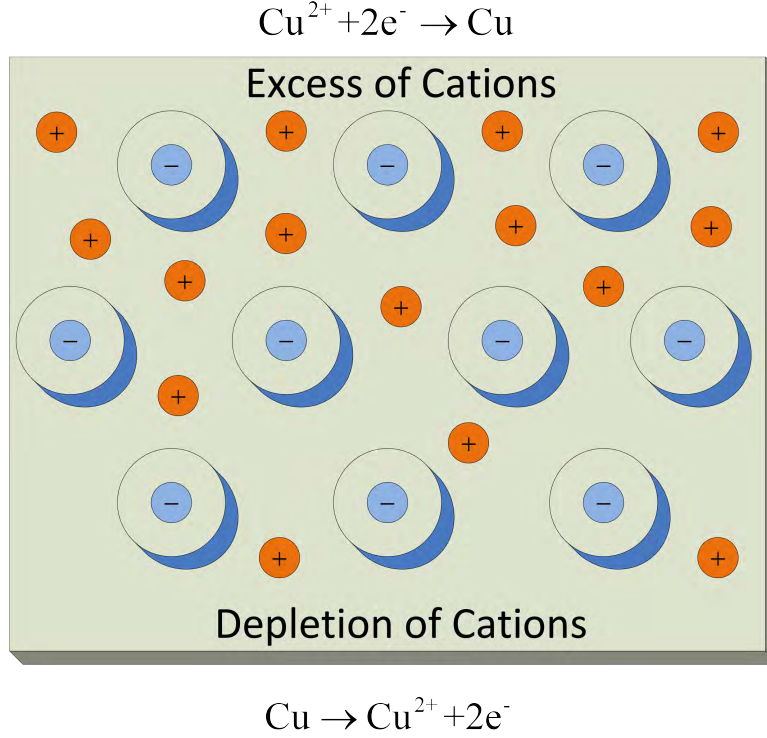
Figure 2-2. Electric double layer streaming potential shown on a nanowick. As the fluid moves up by capillary forces (wicking), the depletion of cations at the base of the device results in a corrosion reaction necessary to replenish the cations. Copper nanowicks have a (-) charge.

Nano devices, by design, cool themselves by the capillary force driving the fluid through the nanostructured posts. The potential driving force is the electric field E_z as a function of the pressure gradient $\frac{dp}{dz}$,

$$E_z = \frac{I_2(R_0)}{I_1(R_0)} \frac{\lambda q_2}{\mu \kappa_{\text{eff}}} \left(\frac{dp}{dz} \right) \tag{2--3}$$

Where I_1 and I_2 are the modified Bessel function of the first and second kind, respectively.[11] R_0 is the ratio of capillary radius to Debye length λ. Pure water at 25 °C has a Debye length of $\lambda = 0.96 \mu m$. Assuming a surface charge of $q_2 = 0.01 \frac{\mu C}{cm^2}$ with an effective conductivity $\kappa = 5.5 \times 10^{-8} \frac{S}{cm}$ and a viscosity of $\mu = 0.01 \frac{g}{cm \dot{s}}$, the electric field can be determined by

$$E_z = 4.375 \times 10^{-6} \frac{I_2(R_0)}{I_1(R_0)} \left(\frac{dp}{dz} \right) \tag{2--4}$$

Furthermore, if the system is assumes to have a pore radius of 100nm which corresponds to the ratio of the Bessel functions in the above express, $I_2(R_0)/I_2(R_0)$, of 0.0025 then the following relation between the the voltage potential ΔV and the pressure drop Δp across a channel size of Δz,

$$\Delta V = E_z dz = 4.375 \times 10^{-6} dp \tag{2--5}$$

As can be seen from this linear relation a pressure drop of 10 kPa results in a voltage potential of 4.375 V.

2.1.5 Thermogalvanic Corrosion

Thermogalvanic corrosion occurs when one part of a metal is maintained at a higher temperature relative to the other parts. In the presence of a temperature gradient of 20°C Rushing[12] describes how copper solubility in the[13] varies sufficiently to induce corrosion.

2.2 Influence of Solution Chemistry

The corrosion of copper in aerated media has been thoroughly studied and is now relatively well understood. Copper in the presence of acid chloride[14,15,16,17] takes places by a mechanism that involves formation of $CuCl_2^{-1}$ with no evidence indicating the presence of a protective oxide layer CuO_2.[18] The reaction process is diffusion controlled rather than activation controlled which demonstrates a Tafel behavior with corresponding Tafel slopes of 2.303RT = F. Acidic sulphate media[19,20,21,22] result in the anodic dissolution of copper which is also diffusion controlled, albeit a different diffusing species. Additional electrochemical studies[23,24,25] demonstrate the effects of alkaline environments on copper. Of particular interest to US Navy, ships using copper and copper alloys as heat exchangers are subject to corrosion under high flow marine environments.[26,27,28,29] Copper corrosion in an alkaline chloride media involves erosion-corrosion reaction whereby hydrodynamic shear disrupts the copper oxide protective layer thus rendering the copper exposed and susceptible to corrosion.

2.2.1 Acidic Chloride Media

Much of the literature discusses the corrosion of copper in an acidic media containing corrosive species such as sulphate or chloride ions. Anodic dissolution of copper in an acidic chloride solution has been extensively discussed in the literature.[14,15,16,17] Much of this work aims to obtain kinetic expressions based on Nerst's equation and Fick's first law. For constant anodic current at varying chloride concentrations up to 1M, Lal and Thirsk[14] show polarization curves based on the Tafel equation,

$$\frac{dV}{d\log\left[Cl^-\right]} = 2\left(\frac{2.303RT}{F}\right) \tag{2--6}$$

where the temperature dependent, T, change in potential, V, with respect to the log of the chloride concentration is related to Avogadro's constant, R and Faraday's constant, F.

Chloride concentration higher than 1M changes the coefficient 2 seen in Eq. (2–6) to 3. Bacarella and Griess[18] consider the anodic dissolution of copper in acid with chloride concentration ranging from 0.124M to 1.24M. Their results show that this process is diffusion controlled rather than activation controlled which demonstrates a Tafel behavior with corresponding Tafel slopes of 2.303RT/F. Furthermore, the Tafel behavior consistent as high as 175 °C which is pH independent on this chloride concentration range. The formation of $CuCl_2^-$ was the primary product obtain with no evidence indicating the presence of the protective oxide layer CuO_2.

2.2.2 Acidic Sulphate Media

When sulphides are present in solution copper is seen to corrode at faster rates. The oxide film that is seen on the copper surface becomes susceptible to reduction of oxygen in the presence of sulphides.[19] Copper dissolution in acid solution under various stirring conditions, acid strength and O_2 saturation level is presented by Andersen.[20] In this work it is found that the anodic dissolution of Cu occurs faster in an O_2 saturated solution than in a N_2 saturated solution. Under weakly acidic conditions they compare the fast rate-determining diffusion controlled step for the anodic dissolution of Cu in the presence

of HCl to that of H_2SO_4. Slightly acid sulfate solution reduce the stability of the Cu^+ and are removed by forming the CuO_2 precipitate.

A study of copper dissolution in an acidic sulphate media was used to investigate whether copper dissolution occurs through a monovalent or divalent state.[21] Using a quartz crystal microbalance, impedance spectroscopy and electrocoulometry it was found that copper dissolves to the monovalent Cu^+ at low current densities $10^{-5}A/cm^2$ and to Cu^{2+} at higher current densities $10^{-2}A/cm^2$. The instability of the Cu^+ in solution transforms the monovalent copper by the following disproportionation reaction,

$$2Cu^+ \rightarrow Cu^{2+} + Cu \qquad\qquad (2\text{--}7)$$

Where the dominating species of Cu and Cu^{2+} are disproportionately favored.

2.2.3 Alkaline Media

In extreme alkaline environments electrochemically formed anodic films act as a barrier on the copper surface protecting the copper from corrosion. In-situ Raman spectroscopy was used to study[22] the passivating films of copper in 1M and 6M KOH at different potentials. Based on the anodic voltammetric peaks in conjunction with in-situ Raman spectroscopy, the authors were able to identify the copper surface film products as Cu_2O, $Cu(OH)_2$ and CuO respectively. Once formed, the anodic surface films become more difficult to reduce and doing so requires a high cathodic potential. Alternatively, one could lower the pH of the electrolyte to facilitate in the dissolution of the passive film to recover the copper surface.

Additional electrochemical studies[23,24,27] demonstrate the effects of alkaline environments on copper metal. Several studies of copper containing intrauterine (IUD) devices[31,32] discuss the pH dependent copper corrosion of simulated uterine solution over a physiologically relevant pH range of 6.3 to 8.0.[25] In this study the characterization of the corrosion products is obtained using absorption spectroscopy. For the simulated uterine sample, the highest corrosion rate was found at a pH = 5.0. Here the presence hydrogen

Table 2-1. Reactions were adopted from Mayer[22] and thermodynamic values were calculated based on Pourbaix's[30] work.

RedOx Potential (V vs. Hg/HgO)	Coupled Reaction at Equilibrium
-0.87	$2H_2O + 2e^- \rightleftarrows H_2 + 2OH^-$
-0.496	$2Cu + 2OH^- \rightleftarrows Cu_2O + H_2O + 2e^-$
-0.340	$Cu_2O + 6OH^- \rightleftarrows 2Cu_2O^{2-} + 3H_2O + 2e^-$
-0.220	$Cu_2O + 2OH^- \rightleftarrows 2CuO + 3H_2O + 2e^-$
-0.189	$Cu_2O + 2OH^- + H_2O \leftrightarrow 2Cu(OH)_2 + 2e^-$
0.32	$4OH^- \rightleftarrows H_2O + O_2 + 4e^-$

ions play an important role in promoting the corrosion of copper as,

$$2Cu + 4H^+ + O_2 \rightarrow 2Cu^{2+} + 2H_2O \qquad (2\text{–}8)$$
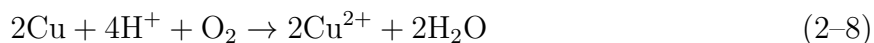
At higher pH they observe a similar passivating behavior as is reported by Mayer,[22] attributing cupric oxide Cu_2O as the primary film product. A proposed mechanism for copper corrosion in a UID is,

$$8Cu + O_2 + 2H_2O \rightarrow 4Cu_2O + 4H^+ + 4e^- \qquad (2\text{–}9)$$

$$Cu_2O + 2H^+ \rightarrow 2Cu^{2+} + H_2O + 2e^- \qquad (2\text{–}10)$$
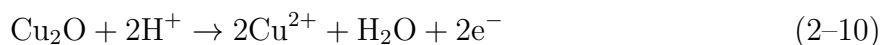
The film product observed for the copper intrauterine device agrees with the anodic copper film described by.[22]

2.2.4 Alkaline Chloride Media

Of particular interest to the US Navy are their ships which utilize copper and copper alloys as heat exchangers. These heat exchangers become subject to corrosion under high flow marine environments.[24,26,27,28,29] Copper corrosion in an alkaline chloride media involves erosion-corrosion reaction whereby hydrodynamic shear disrupts copper protecting layer. Using an axisymmetric impinging jet coupled with a scanning ellipsometer, the authors use electrochemical techniques to compare the high flow conditions to those under static conditions of 3.5%wt NaCl in solutions having pH 8.5 and 9.8. Specifically, the

surface shear stress was isolated from other corrosion-erosion mechanisms and found not to be the primary source for copper erosion-corrosion under alkaline chloride conditions.

Neutral Media. It has been reported[19] that water at pH $= 7$ and 25ºC with dissolved O_2 concentrations as low as 8 ppb can contribute to a redox potential of $+0.76$ (vs SHE). For the following coupled redox reaction oxygen is being reduced

$$O_2 + 2H_2O + 4e^- = 4OH^- \qquad\qquad (2\text{–}11)$$

On the copper surface the reduction of O_2 will be dependent on both the number catalytic sites available and the potential. It has been observed at neutral conditions that the reduction of O_2 can result in an increase in the interfacial pH as high as $10 - 11^{33}$ from the formation of OH^-.

Electrochemical experiments[29] show that pure copper in a neutral solution results in the formation of an oxide film works to protect the copper from corrosion. As time progresses the authors report that the oxide film on the electrode surface increases based on the increase in the polarization resistance. The importance of the self-forming oxide layer is apparent when comparing the results of neutral pH to an acidic environment. At pH $= 1$, with increased immersion time, the dissolution of the native oxide film at the copper surface occurs exposing the copper surface. Once exposed, the copper surface is susceptible to corrosion where solution composition, pH and potential can all play a role in the interfacial electrochemistry.

Once such case, involving the corrosion of copper in aerated neutral tap water solution, is reported to be controlled by the diffusion of copper ions in the cuprous oxide film.[34] Diffusion controlled Warberg impedance observed in their EIS results indicate that the anodic process dictates the net rate of copper corrosion. From the Warberg impedance one can obtain the polarization resistance which increases with immersion time. The authors attribute the increasing polarization resistance to the proliferation of the natant copper oxide film. Furthermore, if exposed to flow conditions induced by a rotating

disc electrode the authors observe an increase in anodic current and lower polarization resistance which can be attributed to the thinning of the oxide layer. At pH lower than 5 the authors suggest that mixed diffusion (diffusion of copper ions in oxide film and in solution) occurs. Unfortunately, this claim,under acidic conditions, lack the support XPS and cyclic voltammetry data that was present for the neutral and alkaline studies.

2.3 Nuclear Waste Storage

Corrosion in deaerated deionized water is less well understood. The equilibrium potential for the copper dissolution reaction is 0.377 V with reference to the hydrogen reaction, therefore, in neutral deaerated media, copper is commonly believed to be immune to corrosion in pure water. The stability of copper in deaerated environments motivated proposed storage of nuclear waste[33,35,36,37,38,39,40] in copper-lined containers to be placed in underground vaults. Hultquist[2] showed, however, that copper foil stored for 15 years in a Erlenmeyer flask with permeable membrane selectively permitting the egress of hydrogen revealed significant corrosion. This was in contrast to a flask that was hermetically sealed and showed no corrosion.

CHAPTER 3
OVERVIEW OF ELECTROCHEMICAL IMPEDANCE SPECTROSCOPY

Electrochemical Impedance Spectroscopy (EIS) is a powerful non-invasive technique used for studying interfacial electrochemistry. Having gained tremendous popularity in recent years, EIS has become widely used in elucidating the corrosion processes of various metals and alloys. EIS measurements are obtained by applying a small amplitude sinusoidal perturbation signal and measuring the systems response at modulated frequency. The output signal is measured in the frequency domain and therefore contains both real and imaginary components. Impedance is defined as the ratio of the change in potential ΔV to the change in current ΔI,[41]

$$Z = \frac{|\Delta V|}{|\Delta I|} e^{j\phi} = Z_r + jZj \qquad (3\text{--}1)$$

where ϕ is the phase difference between potential and current, j is a complex number and Z_r and Z_j are the real and imaginary components of the measured impedance. When current and potential are in phase, the impedance contains only the real component and is expressed as resistance,

$$Z_{res} = R \qquad (3\text{--}2)$$

If there exists a phase shift of 90 degrees between the current and potential corresponds to a pure imaginary component and is oftentimes defined as the capacitance,

$$Z_{cap} = \frac{1}{j\omega C} \qquad (3\text{--}3)$$

Figure 3-1 shows the potential versus current plot and illustrates the small-amplitude sinusoidal perturbation applied to the system during a typical EIS measurement. EIS measurements can be used to directly investigate the electrochemistry occurring on the electrode surface. Nyquist plots showing real versus imaginary are used to represent the impedance data. EIS Measurements are taken sweeping from high frequency (LHS of Nyquist plot) to low frequency (RHS of Nyquist plot). Consider the impedance
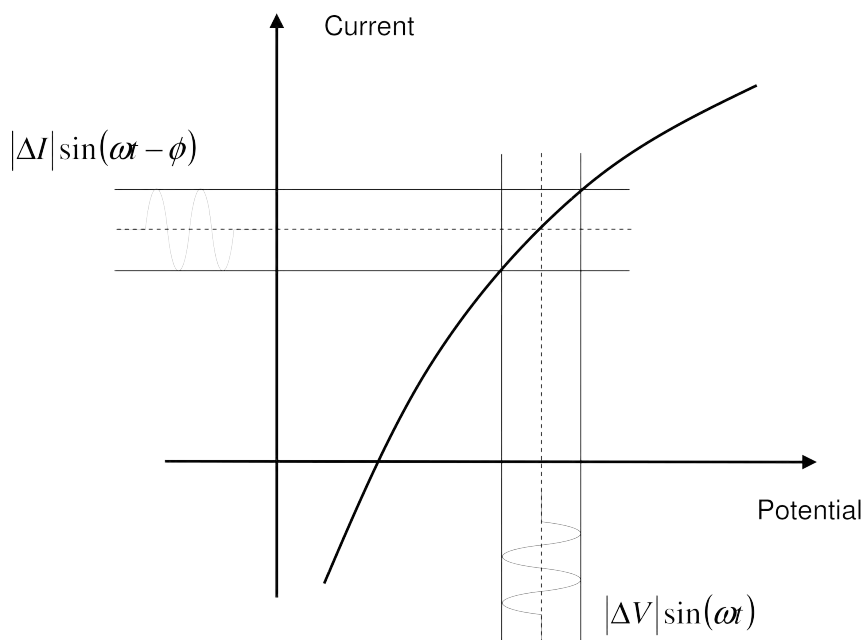
Figure 3-1. Sinusoidal perturbation of an electrochemical system at steady state, where ΔV and ΔI represent the potential and current oscillating at the frequency ω with a phase difference of ϕ.[42]

results obtained for Pt, W, and Au (plated w/W) shown in Figure 3-2. The response of the Pt electrode is linear when compared to the semicircular impedance of tungsten. Electrochemically, the linear behavior of the impedance suggests that the Pt electrode is inert to any cathodic or anodic reaction at open circuit which is classified as blocking electrode behavior. Alternatively, the finite value of impedance observed at low frequencies for the tungsten microelectrodes suggests the presence of Faradaic reactions. The impedance response for the Pt electrode shows the behavior one would expect if no corrosion were occurring in the Cu nanowick.

Electrical circuit analogs are frequently used to illustrate the distribution of potential in an electrochemical system. The type of electrochemistry being considered dictates how one constructs the analogous circuit. For example, a system having contributions from only the Ohmic resistance of the electrolyte R_e and interfacial impedance Z_0 correspond to an in series analog circuit as seen in Figure 3-3A. In series circuits are mathematically
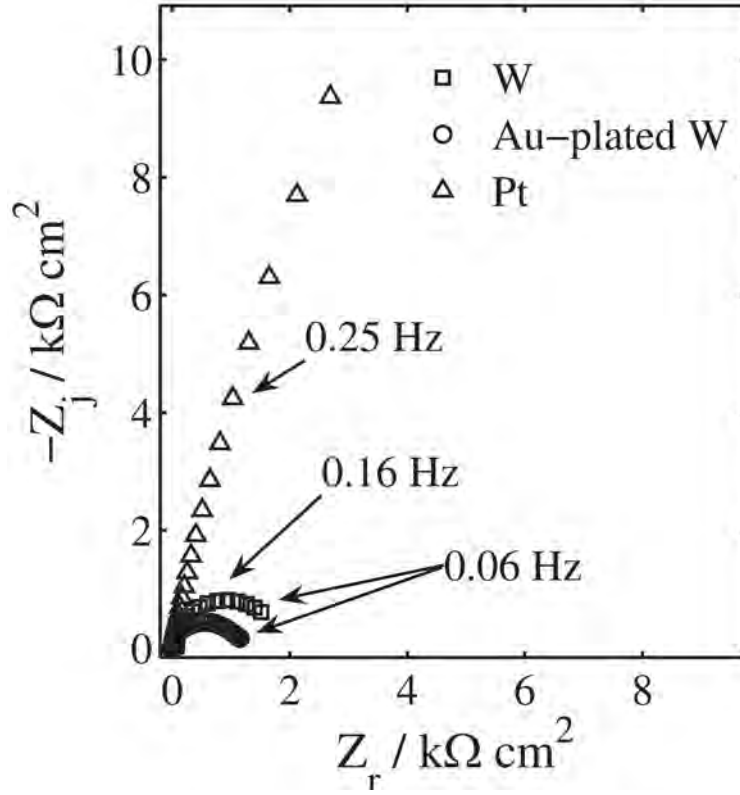
Figure 3-2. Impedance response of platinum, gold plated tungsten and tungsten measured from 0.1 Hz to 20 kHz. The impedance response clearly delineates the blocking (nonreactive) behavior of the platinum electrode from the Faradaic reactive behavior of the two tungsten electrodes.[43]

represented by the sum of the components,

$$U = R_e i + V \tag{3–4}$$

In order to understand the interfacial impedance, we must not only consider the charging current, but we must also account for the Faradaic current as well. At the open circuit potential (corrosion potential) the sum of the anodic and Faradaic currents must be zero,

$$i_a + i_c = 0 \tag{3–5}$$

This means the current paths shown in Figure 3-3B will be a parallel sum of Z_a and Z_c. Furthermore, we must consider the contribution of the double layer capacitance $C_d l$ which
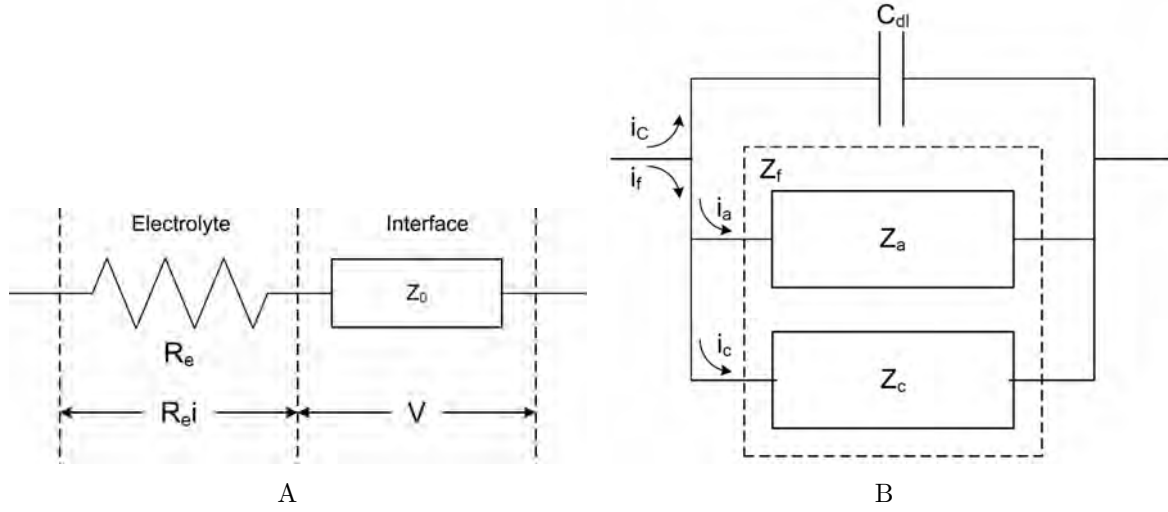
Figure 3-3. Analogous circuits of an electrochemical interface susceptible to corrosion at the open-circuit potential: A) electrical circuit in series to account for Ohmic resistance and interfacial impedance; B) electrical circuit showing how the interfacial impedance can be represented by the addition of impedances in parallel to account for current contributions associated with charging the interface, the anodic (corrosion) reaction, and the cathodic reaction.[41]

is added in parallel.

$$Z_0 = \frac{1}{\frac{1}{Z_a} + \frac{1}{Z_c} + j\omega C_{dl}} \tag{3--6}$$

The anodic impedance of the corroding copper nanowick Z_a will be small and easily seen in the impedance response Z_0, therefore making impedance spectroscopy a viable technique for investigating the mechanisms leading to the corrosion of the nanowicks.

CHAPTER 4

CORROSION OF COPPER IN DEAERATED WATER

The need for increasingly more-functional electronics and the industry's ability to fabricate high density integrated circuits have led to an ever-increasing generation of waste heat in advanced electronics systems. The increases in power generation has often been handled by improvements in materials or components configuration. However, it is now generally acknowledged that the cooling requirements for advanced electronics exceed the heat-removal capability of conventional cooling techniques. Liquid-based cooling[44,45,46,47,48,49,50] may remedy thermal management issues that have plagued development and deployment of enhanced electronic systems.

4.1   Heat Sinks used to Cool High Performance Electronics

Due to its exceptional heat transfer characteristics, particularly in the phase change process, water is considered to be a suitable cooling fluid, so long as issues related to its electrical properties can be addressed. Numerous studies have been conducted to develop high performance water heat sinks.[51,52,53,54,55,56] These studies often utilize micro- or nanostructures to enhance heat transfer at the solid-liquid interface. Traditionally, copper has been the material of choice in water heat exchangers, and, as it is generally understood that copper does not corrode in deaerated deionized water, copper micro/nanostructures are implemented to benefit from the associated enhanced heat transfer characteristics.

The performance of micro/nanoscale copper structures has, however, been observed to degrade with time. Ju et al. [6] reported that corrosion in copper microfluidic channels used in a two-phase cooling system caused performance degradation. Since the cooling performance is intricately related to functionality of the liquid-vapor interface and fluid flow through a structure,[5] even small rates of corrosion can impair performance of a micro/nanostructured interface. Thus, an ability to predict and mitigate copper corrosion is needed.

4.2   Stability of Copper in Different Media

The corrosion of copper in aerated media is relatively well understood. In acidic chloride solutions, for example, the corrosion of copper takes place by a mechanism that involves formation of $CuCl_2^{-1}$ from a CuCl intermediate.[17] The reaction process is reported to be diffusion controlled with no evidence of a protective oxide layer.[57] This mechanism has been presented as valid for temperatures as high as 165 °C.[18]

In contrast to the mechanism accepted for acidic chloride solutions, direct formation of Cu^+ and Cu^{2+} has been observed for corrosion of copper in acidic sulphate media.[20,21,22] Jardy et al. [21] used a quartz crystal microbalance, impedance spectroscopy, and electrocoulometry to show that copper dissolves to the monovalent Cu^+ at low current densities ($10^{-5}A/cm^2$) and to the divalent Cu^{2+} at higher current densities ($10^{-2}A/cm^2$). The Cu^+ species is unstable and participates in a homogeneous reaction according to

$$2Cu^+ \rightarrow Cu^{2+} + Cu \qquad\qquad (4\text{--}1)$$
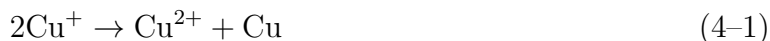
where solid and divalent copper are disproportionately favored over the less stable Cu^+.[21]

In extreme alkaline environments, electrochemically formed anodic films act as a barrier to protect the copper from corrosion. In-situ Raman spectroscopy was used to study the passivating films of copper in 1M and 6M KOH at different potentials.[22] Based on the anodic voltammetric peaks, in conjunction with in-situ Raman spectroscopy, the authors identified surface films composed of Cu_2O, $Cu(OH)_2$, and CuO. Once formed, the anodic surface films become more difficult to reduce and doing so requires a high cathodic potential. Alternatively, one could lower the pH of the electrolyte to facilitate the dissolution of the passive film to recover the copper surface. In alkaline solutions, the first and second oxidation states are typically reported but in a study by Miller,[23] a soluble Cu^{3+} species was identified in the anodic region at the onset of oxygen evolution.

Of particular interest to naval vessels, copper and copper alloy heat exchangers cooled with seawater are subject to corrosion under high velocity flow.[28,29] The large shear stress

at tube and inlet walls was found to remove loosely adherent salt films, causing formation of galvanic cells.[26, 24, 27] This effect has been described as resulting from erosion-corrosion.[58]

Bojinov et al. provided a mechanistic study of copper interactions with a deoxygenated neutral aqueous borate buffer solution.[60] Their preliminary conclusions were that no sustained corrosion of copper was found, but that the impedance results were consistent with an adsorbed CuOH intermediate associated with reduction of Cu(II) species. In an earlier study, Bojinov et al. used an on-line resistance probe to discover that copper corroded at an appreciable rate of 16 μm/y during short-time exposure to 1 M NaCl that contained very small amounts of oxygen.[61] After longer exposure, the corrosion rate decreased and back-deposition of copper was reported. As part of the analysis of the suitability of copper for nuclear waste storage, Sharifi-Asla and Macdonald[62] have performed studies of the hydrogen evolution reaction on copper in deoxygenated neutral aqueous borate buffer solutions.

Incidence of copper corrosion in deaerated deionized water has also been reported in the heat exchangers used to cool the synchrotron at Argonne National Labs. A study of corrosion rates as a function of oxygen content in neutral deionized water revealed that the corrosion rate was greater than 8 mg/m^2/day (0.9 nm/day), even at dissolved oxygen concentrations as low as 15 ppb.[63, 64] These results were confirmed by subsequent analysis based on a non-stationary finite-difference simulation used to represent the processes of corrosion, erosion, dissolution, precipitation and deposition for the length of a 1-D cooling circuit. In this work, Parro found a corrosion rate of 1 g/m^2/year (0.3 nm/day).[65] These corrosion rates were considered to be sufficiently small as to pose no long-term problems with the operation of the synchrotron.

4.3 Disposal of Spent Nuclear Rods

A similar body of work does not exist for corrosion of copper micro/nanoscale structures in heat exchangers, though this area may be closely related to the body of work associated with plans for encasing nuclear waste in copper cladding. The standard

32

equilibrium potential for the copper dissolution reaction has a value of 0.337 V with reference to the hydrogen reaction;[59] therefore, copper is commonly believed to be immune to corrosion in neutral deionized deaerated media. The proposed stability of copper in deaerated environments has motivated investigation of the feasibility for underground storage of nuclear waste in copper-lined containers.[35,36,37,38,39,40,33] Concern has been expressed over results presented by Hultquist[2] who showed that copper foil, stored for 15 years in an Erlenmeyer flask filled with deaerated deionized water and capped with permeable membrane, selectively permitting the egress of hydrogen, revealed significant corrosion. Corrosion was not observed for a similar foil enclosed in a hermetically sealed flask that did not allow the effusion of hydrogen (or any gas). In a critique, King and Lilja identify some inconsistencies and indicate that other groups have been unable to reproduce Hultquist's results. Macdonald and Sharifi-Asl state, however, that Hultquist's results are not at odds with thermodynamics, provided that the concentration of Cu^{2+} and the partial pressure of hydrogen are suitably low.[40]

Small rates of corrosion may, however, be significant for heat exchangers in which surface nano-structure posts are utilized to fundamentally change the physics of liquid-surface interactions and to greatly enhance the phase-change heat transfer process. Small rates of corrosion may also compromise safe storage of nuclear waste where structural integrity must be assured for periods exceeding one million years.

The objective of this work is to use electrochemical techniques to quantify corrosion of copper in pure deaerated water. The experimental techniques employed in this study include impedance spectroscopy and linear sweep voltammetry. From these measurements, corrosion rates were determined and further validated with the use of kinetic modeling, and thermodynamic simulations.

4.4   Experimental

The experimental protocol, instrumentation, and electrodes are presented in this section.
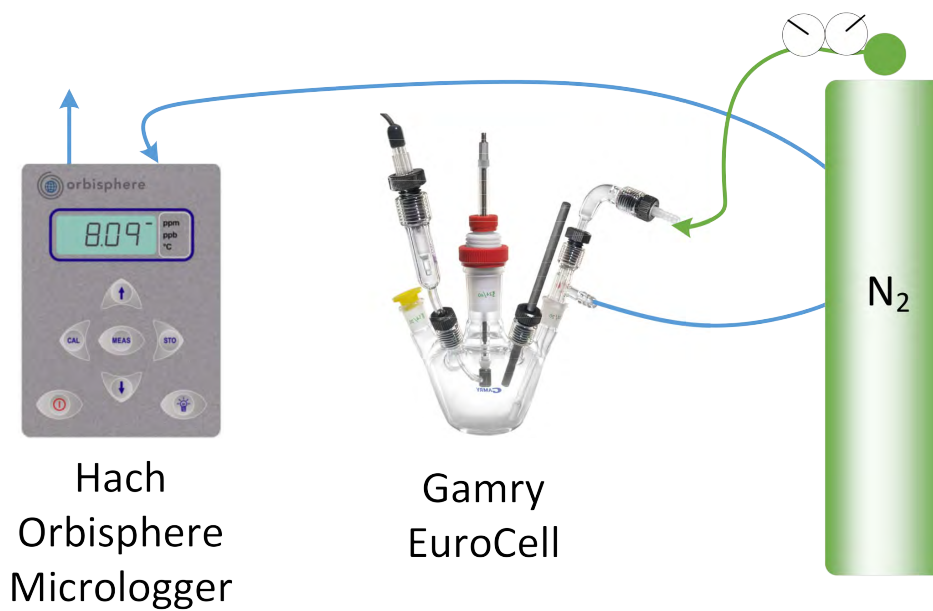
Figure 4-1. Schematic diagram showing the deaeration process used to achieve 1-2 ppb gas-phase O_2 concentration levels, resulting in a substantially lower concentration in the water.[1]

4.4.1   De-Aeration Procedure

A five port 200 ml glass vessel (Gamry EuroCell®), shown in Figure 4-2, was used as the electrochemical cell. The volume of electrolyte was 30 cm^3. The deionized water (Barnstead E-Pure D4631) had a resistivity of 17.6 MΩcm. BIP® grade nitrogen gas (Airgas), with guaranteed 99.9999% purity was used to deaerate the system through a microporous glass frit for at least 1.5 h. A Hach Orbisphere 3650 micrologger, with a sensitivity of 0.1 ppb O_2, was used to monitor the O_2 concentration of the gas emanating from the cell, continuously until a stable 1-2 ppb gas-phase oxygen level was achieved. Under these conditions, the large Henry's Law constant for oxygen in water ensured that the oxygen level in the electrolyte was lower than 1 ppb.

To ensure that measurement of gas-phase O_2 concentration reflected the concentrations in the liquid phase, an experiment was devised in which the water from the electrochemical cell was conveyed under pressure to the oxygen detector. The water was de-aerated as discussed above until a stable 1-2 ppb gas-phase oxygen level was achieved. Pressure from

the nitrogen tank was used to force the water from the vessel to the detector through Tygothane® tubing (Saint-Gobain). Oxygen readings were taken after the 30 minute equilibration period recommended by the manufacturer for liquids having ppb levels of dissolved O_2. This measurement was repeated four times and the measured oxygen levels ranged from 8 ppb to 18 ppb. These values represent an upper limit to the oxygen content achieved in the electrolyte as the process introduced the potential ingress of small amounts of atmospheric oxygen. Indeed, the impedance response shown in a subsequent section indicates that the oxygen concentration in the water must have been less than 6.5 ppb.

4.4.2 Instrumentation

Electrochemical experiments were performed for a three-electrode configuration using either a Gamry Reference 3000 or a Gamry Reference 600 potentiostat. For impedance measurements, open circuit potential(OCP) measurements were recorded until the OCP changed less than 0.1 mV/min. A grounded home-built Faraday cage was used to reduce electromagnetic interference. Impedance measurements were performed from 100 kHz to 200 mHz for experiments that explored the high-frequency dielectric response reported in a subsequent section. For studies of electrochemical reactivity, measurements were performed from 1 kHz to 50 mHz. The perturbation amplitude was 10 mV.

Linear sweep voltammetry was performed with a Gamry Reference 3000 using a sweep rate of 0.06 mV/s. Sweeps were performed from the open circuit potential in both anodic and cathodic directions. The working electrode for this experiment was a 0.1 mm diameter annealed 99.9% copper. The reference electrode and counterelectrode were Ag/AgCl as reported below.

4.4.3 Electrodes

The counterelectrode and reference electrodes were solid AgCl pellets embedded in a acrylic tube, sealed with epoxy, and attached to a silver wire. Two hours prior to impedance measurements, the Ag/AgCl electrodes were immersed in pure deionized water (with a resistivity of 17.6 MΩcm) and shorted together to reduce polarizing effects. The
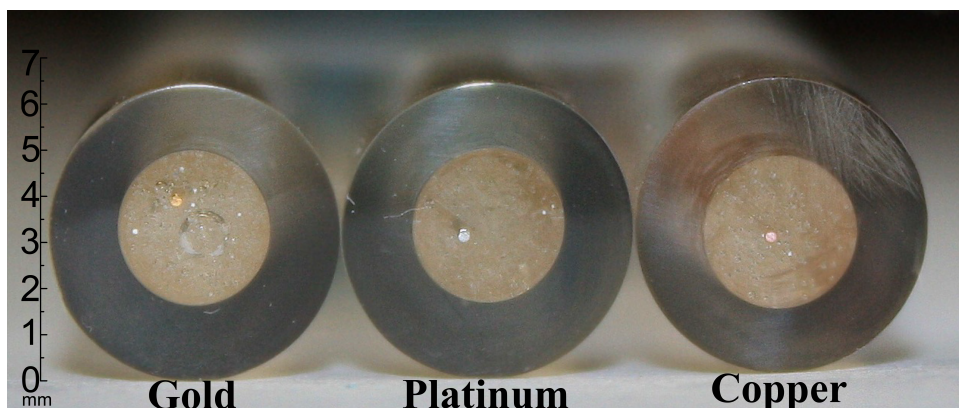
Figure 4-2. Cu, Au and Pt working electrodes with the exposed 0.25 mm disk diameter shown. The outside diameter of the acrylic tube was 6.5 mm.[1] *(Source: Photo courtesy of author.)*

Ag/AgCl electrodes were used in this application to avoid electrochemical reactions that would change the electrolyte pH. The use of solid electrodes prevented contamination of the electrolyte by filling solutions used in conventional reference electrodes.

The working electrodes were composed of annealed 99.9% copper, hard-tempered 99.99+% gold, and annealed 99.9+% platinum (Goodfellow, UK) wires with 0.25 mm and 0.1 mm diameters. The wires were embedded in an epoxy mold to expose only a disk cross-section, as shown in Figure 4-2. Electrode surfaces were polished mechanically with the final polish performed using an alumina suspension with a 0.1 μm particle size until a fine mirror-like finish was visible. A series of organic solvents in increasing polarity (methanol, isopropanol, and acetone) followed by deionized water were used to clean and degrease the surface.

The impedance response for electrodes of diameter exceeding 0.5 mm was dominated by a high-frequency loop that, as discussed in a subsequent section, was attributed to the dielectric response of water. The 0.25 mm diameter electrodes were used in the present work to minimize the portion of the measured frequency range associated with the high-frequency loop, and thereby maximize the response associated with charging and faradaic currents at the electrode.
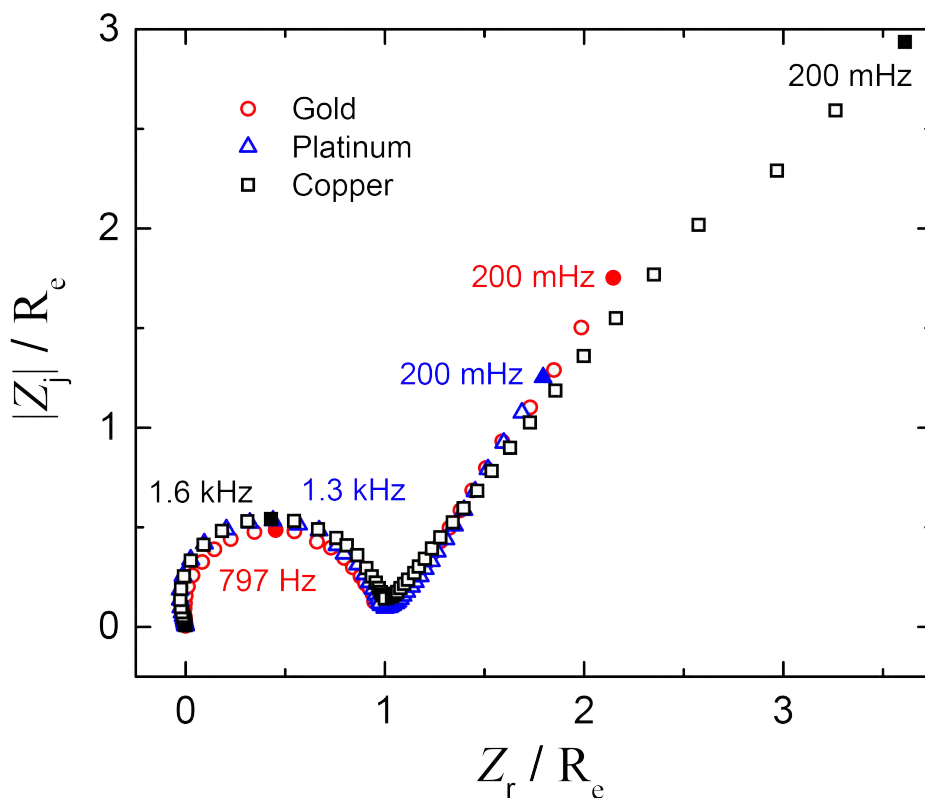
Figure 4-3. Scaled impedance response of copper, gold and platinum 0.25mm diameter electrodes in deaerated deionized water. The frequency range was 100 kHz to 40 mHz.

4.5   Experimental Results

The electrochemical measurements included impedance spectroscopy and linear sweep voltammetry. Impedance measurements on copper electrodes were repeated with inert gold and platinum electrodes in order to reveal differences in electrochemical behavior.

4.5.1   Impedance Spectra

Scaled impedance results, measured at the open-circuit condition, are presented in Figure 4-3 with electrode material as a parameter. The data shown were collected on a frequency range of 100 kHz to 200 mHz. The data were scaled by the apparent Ohmic resistance, obtained at the intersection between the high-frequency and the low-frequency loops, to emphasize the similarity in the high-frequency response for copper, gold, and

platinum electrodes. As this feature is unaffected by the electrode, it can be attributed to the dielectric response of water.

The values of the ohmic resistance obtained from the impedance response were 15.0 kΩcm^2 for the copper electrode, 19.5 kΩcm^2 for the gold electrode, and 12.8 kΩcm^2 for the platinum electrode. Slight differences in these values can be attributed to minute leaching of ions from the glassware. Following the formula for the ohmic resistance of a disk electrode presented by Newman,[66]

$$R_{\mathrm{e}} = \frac{\rho}{4r_0} \tag{4–2}$$

the water resistivity was calculated to be 1.53, 1.98, and 1.30 MΩcm, respectively. This estimated water resistivity is an order of magnitude lower than the initial 17.6 MΩcm water resistivity. A decrease in water resistivity is expected for experiments in highly deionized water.

A second set of experiments, which emphasize the low-frequency behavior, are presented in Figure 4-4. The frequency range, chosen to eliminate the influence of the high-frequency dielectric loop, is 54.5 Hz to 46.5 mHz. The Nyquist representation, shown in Figure 4-4A, indicates that the gold and platinum electrodes had lower electrochemical reactivity than the copper electrode. The imaginary impedance is presented on logarithmic scale as a function of frequency in Figure 4-4B. The slope of the imaginary impedance with respect to frequency indicates that the impedance data for the gold and platinum electrodes may be represented by a constant-phase-element model; whereas, the copper data indicates the presence of two time constants. As both anodic and cathodic electrochemical reactions are required to have an impedance response at open circuit, the impedance data presented for copper in Figure 4-4 suggest that corrosion may be taking place.
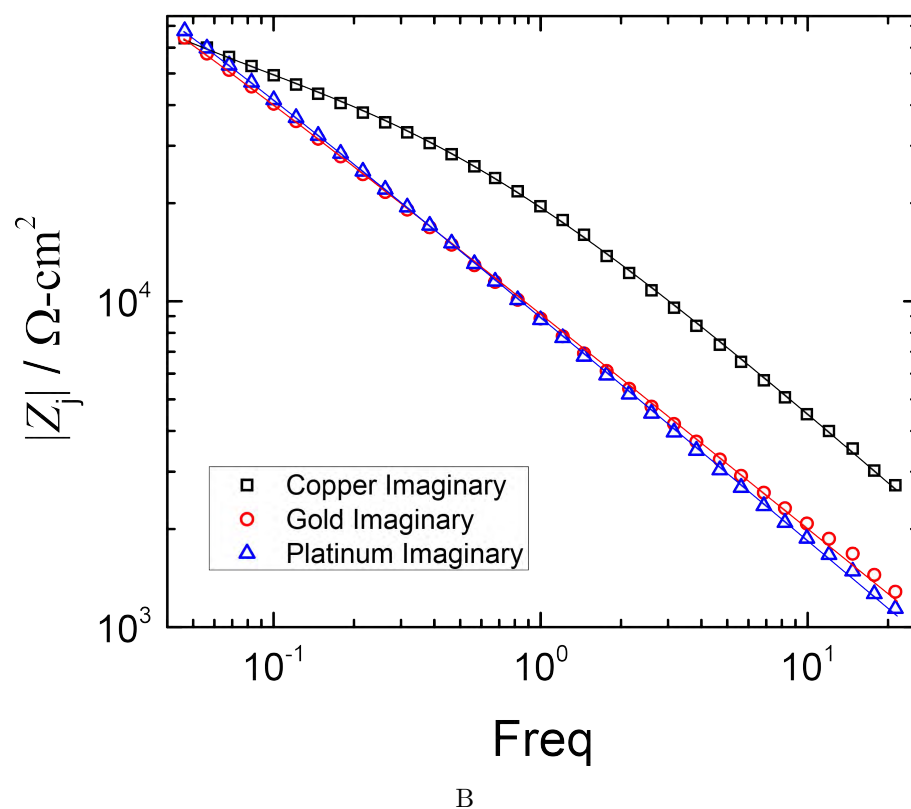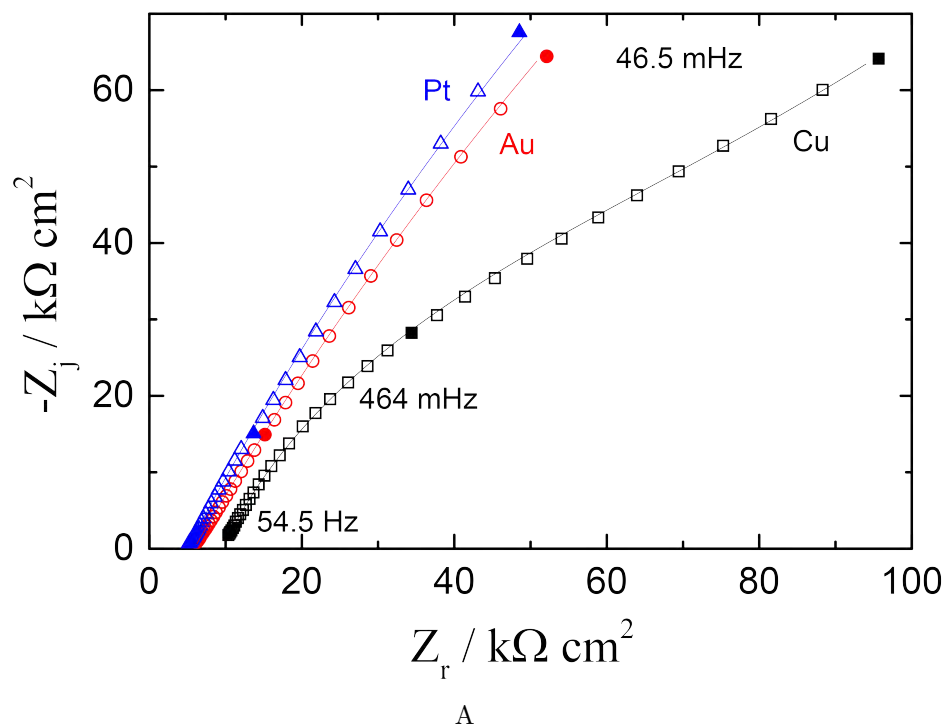
Figure 4-4. Low frequency impedance response of copper, gold and platinum 0.25mm diameter electrodes measured from 40 mHz to 100 kHz (Cu and Au) and from 200 mHz to 100 kHz (Pt): A) Nyquist Plot, and B) imaginary impedance as a function of frequency. The lines correspond to regression results corresponding to the models shown in Figure 4-8.
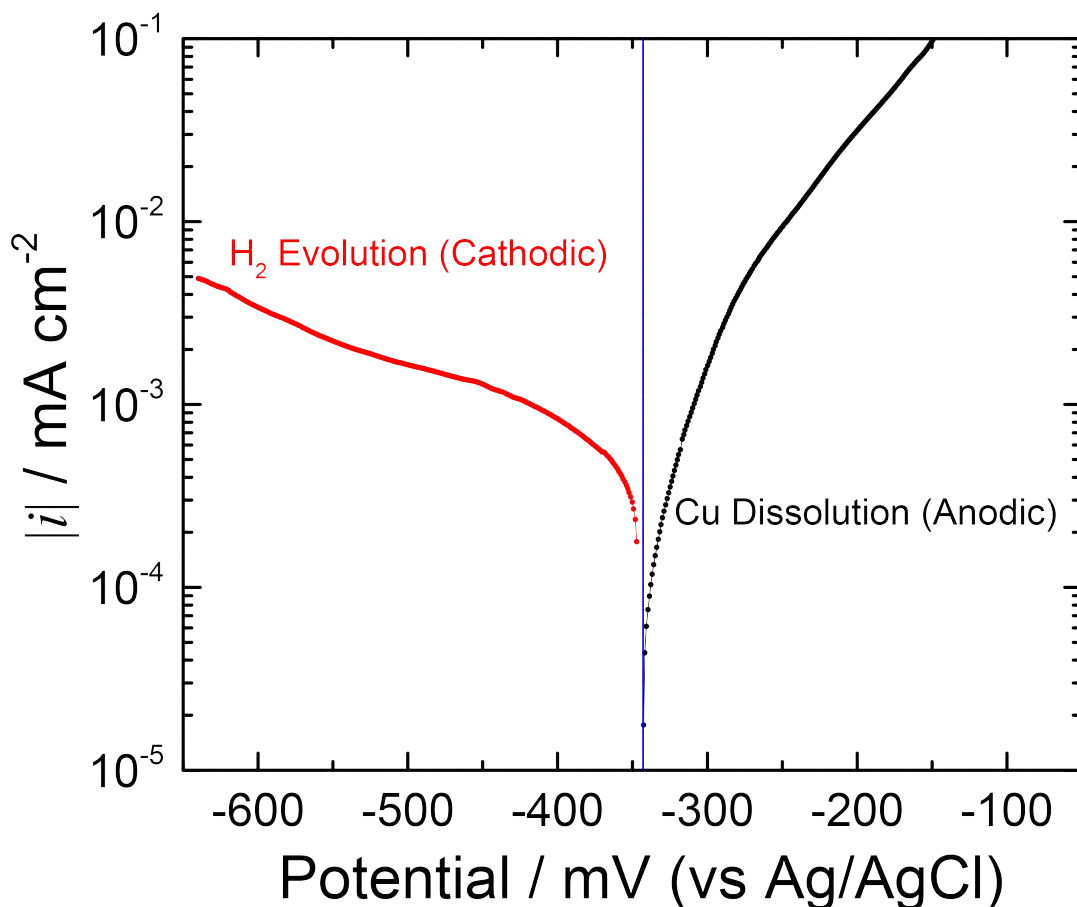
Figure 4-5. Polarization curve for copper deaerated with N_2 and obtained using a sweep
rate of 0.06 mV/s from the open circuit potential in both anodic and cathodic
directions.

4.5.2 Polarization Curves

Polarization curves resulting from linear sweep voltammetry experiments are
presented in Figure 4-5 for a copper electrode. The results were obtained using a
sweep rate of 0.06 mV/s from the open circuit potential in both anodic and cathodic
directions. The polarization curve in the anodic direction indicates both the presence of
corrosion and the absence of oxide films. The composition and resistivity of the electrolyte
changed in response to the electrochemical reactions. IR compensation could therefore
not be performed, and a reliable Tafel slope could not be identified, precluding use of the
polarization curve for accurate identification of the corrosion current. The polarization

curve in the cathodic direction included reduction of species resulting from the anodic reaction at the Ag/AgCl counterelectrode. The measurement of polarization curves caused changes in electrolyte composition that, while small, caused significant changes in the properties of the deionized water. The modifications to electrolyte properties were avoided in the impedance measurements by using a small perturbation amplitude at open circuit.

4.6   Simulations

The observation of corrosion is supported by a series of numerical simulations, including calculation of associated Pourbaix diagrams, kinetic simulation accounting for potential reactions, and regression analysis of the impedance results.

4.6.1   Thermodynamic Analysis

The possibility for corrosion under the conditions tested was explored by calculation of Pourbaix diagrams, presented in Figure 4-6, for pure copper in deaerated deionized water at 25°C. The titrants were assumed to be NaOH and HNO_3. The diagrams were generated by CorrosionAnalyzer 2.0 (Build 2.0.16) by OLI Systems Inc. The computational approach is described in greater detail by Anderko and co-workers.[67,68] The species considered in the thermodynamic analysis are presented in Table 4-1.

The Pourbaix diagrams presented in Figure 4-6 are in good agreement with the Pourbaix diagrams presented by Beverskog and Puigdomenech for copper at 25 °C.[69] The solid color marked $Cu_{(s)}$ represents the region in which copper is stable. The lines marked a and b are the equilibrium lines for evolution of hydrogen and oxygen, respectively, and the region between a and b can be described as the stability region for water. The natural pH, at which no titrants are added, is equal to 7. The redox potential for water, shown in Figure 4-6 by the lower filled circle at pH=7, is on the equilibrium line a for hydrogen when the water is saturated with H_2 at 1 atm pressure. This falls within the stability region for copper. For aerated electrolyte, the redox potential for water lies on the equilibrium line b for oxygen, the upper filled circle at pH=7, where copper is not

41
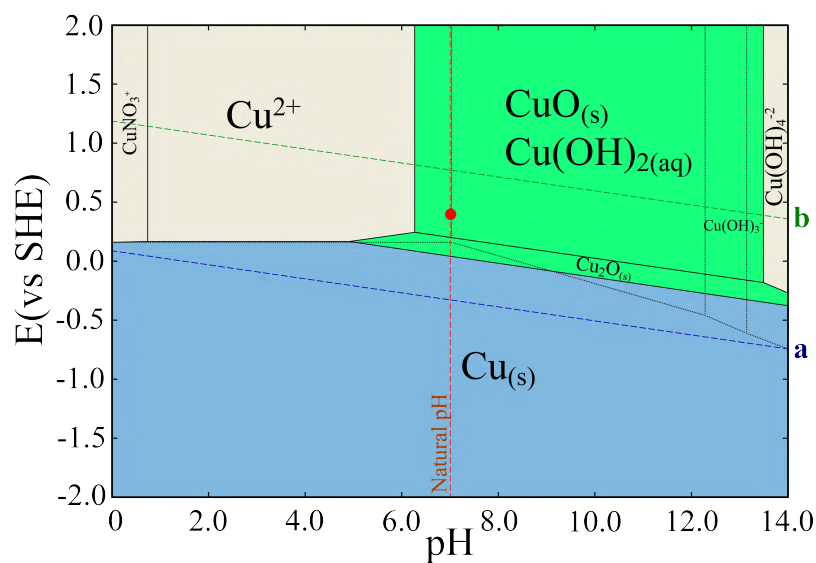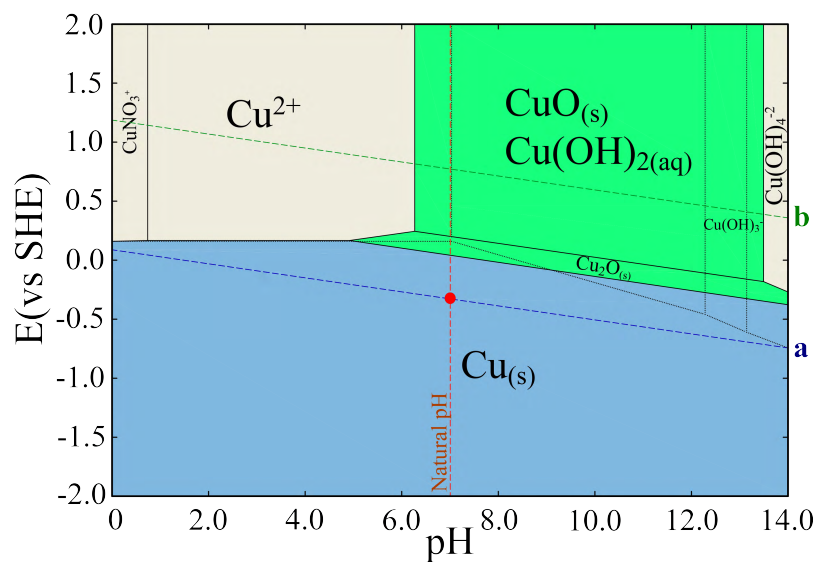
Figure 4-6. Calculated potential-pH (Pourbaix) diagram for copper in deaerated deionized water. The titrants were assumed to be NaOH and HNO$_3$. The marked points correspond to the natural condition for copper deaerated with N$_2$ (upper) and N$_2$ followed by saturation by H$_2$ (lower). The diagrams were generated by CorrosionAnalyzer 2.0 (Build 2.0.16) by OLI Systems Inc.

Table 4-1. List of species considered in the thermodynamic analysis presented as Figure 4-6.

Aqueous Species	Vapor Species	Solid Species
H_2O	H_2O	Cu
Cu^+	H_2	Cu_2O
$Cu(OH)_2$	HNO_3	$Cu(OH)_2$
Cu^{+2}	O_2	$Cu(NO_3)_2 \cdot \frac{5}{2}H_2O$
$Cu(OH)^+$		$Cu(NO_3)_2 \cdot 6H_2O$
$Cu(NO_3)^+$		CuO
$Cu(NO_3)_2$		$NaOH$
$Cu(OH)_4^{-2}$		$NaOH \cdot H_2O$
$Cu(OH)_3^{-1}$		$NaNO_3$
H_2		$Cu(NO_3)_2$
H^+		$Cu(OH)$
OH^-		
NO_3^-		
HNO_3		
O_2		
Na^+		
$NaNO_3$		
$Na(OH)$		
$Na(OH) \cdot H_2O$		

stable. For deaerated water in the absence of hydrogen, the redox potential, shown by the middle marked circle in Figure 4-6, lies between the lines a and b.

The redox potential is not the corrosion potential; but, it may be used as an indicator for the stability of copper. When hydrogen is present, the system may be considered to be at equilibrium, and copper is indicated to be stable. In the absence of hydrogen, the hydrogen evolution reaction may take place until sufficient hydrogen is formed to stabilize the copper. The thermodynamic simulations support the interpretation that the impedance and voltammetry results show corrosion of copper when deaerated with N_2 and that corrosion is suppressed by saturation with H_2. These results are consistent with the experimental observations reported by Hultquist[2] and with the thermodynamic analysis reported by Macdonald and Sharifi-Asl.[40]

4.6.2   Kinetic Simulation

Kinetic simulations were performed to explore the manner in which copper may react in deaerated water. In the absence of oxygen, the reactions were assumed to include dissolution of copper

$$\text{Cu} \rightarrow \text{Cu}^{2+} + 2\text{e}^- \tag{4–3}$$

and hydrogen reduction at the cathode

$$2\text{H}^+ + 2e^- \rightarrow \text{H}_2 \tag{4–4}$$
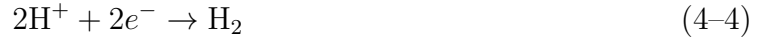
As the concentration of corrosion product increases, the cathodic reaction

$$\text{Cu}^{2+} + 2\text{e}^- \rightarrow \text{Cu} \tag{4–5}$$

begins to play a role. Generation of hydrogen may be expected to result in hydrogen oxidation

$$\text{H}_2 \rightarrow 2\text{H}^+ + 2\text{e}^- \tag{4–6}$$

The corresponding rate expressions were used to construct a time dependent model for the system.

A simulation was performed using the kinetic expressions for reactions presented in Eq. (4–3), Eq. (4–4) and Eq. (4–5).[59] At open circuit potential the net current is equal to zero; thus,

$$i_{\text{a,Cu}} + i_{\text{c,Cu}} + i_{\text{c,H}_2} = 0 \tag{4–7}$$

The anodic current density for copper dissolution is given by

$$i_{\text{a,Cu}} = i_{0,\text{Cu}} e^{b_{\text{a,Cu}}\left(V - V_{0,\text{Cu}}\right)} \tag{4–8}$$

where $V_{0,Cu}$ is the equilibrium potential for the copper reaction. The corresponding cathodic current density can be expressed as

$$i_{\text{c,Cu}} = -i_{0,\text{Cu}} \left(\frac{c_{\text{Cu}^{2+}}(0)}{c_{\text{Cu}^{2+},\text{ref}}} \right)^{\gamma} e^{-b_{\text{c,Cu}}\left(V - V_{0,\text{Cu}}\right)} \tag{4–9}$$

Table 4-2. Summary of the time dependent reactions considered for modeling Cu corrosion kinetics.

Reaction Number	Case I: At Time=0 No O_2	Case II: For Time> 0 No O_2	Case III: For Time> 0 No O_2 and H_2 Enriched
(4–3)	$Cu \rightarrow Cu^{2+} + 2e^-$	$Cu \rightarrow Cu^{2+} + 2e^-$	$Cu \rightarrow Cu^{2+} + 2e^-$
(4–4)	$2H^+ + 2e^- \rightarrow H_2$	$2H^+ + 2e^- \rightarrow H_2$	$2H^+ + 2e^- \rightarrow H_2$
(4–5)		$Cu^{2+} + 2e^- \rightarrow Cu$	$Cu^{2+} + 2e^- \rightarrow Cu$
(4–6)			$H_2 \rightarrow 2H^+ + 2e^-$

where the concentration term accounts for the concentration of cupric ion at the electrode surface, $c_{Cu^{2+},ref}$ is the concentration at which the exchange current density was obtained, and γ was assigned a value of 0.75. The cathodic hydrogen evolution reaction was expressed as

$$i_{c,H_2} = -i_{0,H_2} e^{-b_{c,H_2}\left(V - V_{0,H_2}\right)} \tag{4–10}$$

where V_{0,H_2} is the equilibrium potential for the hydrogen evolution reaction. The concentration of copper at the electrode surface was assumed to be controlled by spherical diffusion from the electrode,[70] thus,

$$\left(i_{a,Cu} + i_{c,Cu}\right) = \frac{4n\mathrm{F}D_{Cu^{2+}}r_0}{A}\left(c_{Cu^{2+}}(0) - c_{Cu^{2+}}(\infty)\right) \tag{4–11}$$

The three cases shown in Table 4-2 were considered. Case (I) corresponds to an initial condition in which copper dissolution is balanced by hydrogen evolution. For Case (II), accumulation of copper ions at the electrode surface allows copper dissolution and reduction reactions to occur in tandem with the reduction of hydrogen. Case (III) accounts for saturation by H_2 gas.

The set of equations was solved simultaneously under a pseudo-steady-state approximation in which the concentration $c_{Cu^{2+}}(\infty)$ was increased incrementally by

Table 4-3. Values for the equilibrium potential for the copper dissolution reaction were taken from Figure 1 of reference[71] and adjusted to be referenced to the Normal Hydrogen Electrode. The electrolyte pH for the hydrogen reaction reported in reference[62] was obtained by adding NaOH. Corrosion rates represent calculated values averaged over a one-year period.

Reaction	pH	p_{H_2}, atm	E_0, V(NHE)	i_0, A/cm^2	b_a, V^{-1}	b_c, V^{-1}	i_{corr}, nm/day
rxn (4–3)[a]	–	–	-0.1876	9×10^{-4}	20	53.56	–
rxn (4–4)[b]							
A	5.72	1	-0.331	3.46×10^{-7}	–	23.03	7.94
B	8	1	-0.465	6.76×10^{-7}	–	23.50	1.12
C	9.2	1	-0.535	1.01×10^{-6}	–	23.03	0.45
D	8	0.5	-0.456	5.43×10^{-7}	–	23.03	1.16
E	8	0.3	-0.450	4.73×10^{-7}	–	24.24	1.05
F	8	0.1	-0.436	3.28×10^{-7}	–	24.24	1.02

a) The electrolyte was 0.7 M CuSO$_4$ in 1.5 M H$_2$SO$_4$. Data taken from reference.[71]
b) NaOH was titrated to achieved desired pH in 0.03 H$_3$BO$_3$. The electrolyte temperature was 20°C. Data taken from reference.[62]

a material balance. The kinetic parameters used for the simulations are presented in Table 4-3.

As parameters from pure water were not found in the literature, data were taken for environments associated with similar reaction mechanisms. Formation of CuCl was not expected in the present system; therefore, parameters for the copper dissolution and deposition were taken from a reference reporting experiments in a sulphate electrolyte. The exchange current density used in our simulations was adjusted for the cupric ion concentration at which the exchange current was measured, as shown in Eq. (4–9). Buffered borate electrolytes have been used as a surrogate for waters associated with nuclear repositories.[60,62] The parameters for the hydrogen evolution reaction at 20°C were taken from Sharifi-Asla and Macdonald, who reported results in a boric acid electrolyte with pH adjusted by addition of NaOH.[62] The resulting calculated corrosion rates, averaged over a one year period, are a strong function of pH. For the system under investigation, under the assumption that hydrogen was removed by deaeration, the corrosion rate for parameter set A obtained at a pH of 5.72 was calculated to be 7.9

nm/day. The average corrosion rate for parameters obtained at a pH of 8 (sets B, D, E, F) was calculated to be 1 nm/day. The calculated corrosion rate for hydrogen parameters obtained at a pH of 9.2 was 0.45 nm/day. In the presence of a saturated pressure of hydrogen, the net rate of corrosion (not shown in Table 4-3) was calculated to be equal to zero. These results are in agreement with the thermodynamic results presented in Figure 4-6.

An understanding of the results presented in Table 4-3 may be obtained from the Evan's diagram presented in Figure 4-7 that was taken from the simulation D at $t = 0$, for which $c_{Cu^{2+}}(\infty) = 0$. The solid lines correspond to the total cathodic current, $i_{c,Cu} + i_{c,H_2}$, and the anodic current $i_{a,Cu}$. The dashed lines represent the contributions of $i_{c,Cu}$ and i_{c,H_2}. The vertical line at the intersection of total cathodic and anodic current (point ① in Figure 4-7) yields the corrosion potential $V_{corr} = -0.3399$ V. At the corrosion potential, $i_{a,Cu} = 2.582 \times 10^{-7}$ A/cm^2 and the sum of cathodic current densities has the value $i_{c,Cu} + i_{c,H_2} = -2.582 \times 10^{-7}$ A/cm^2. The cathodic copper deposition current density, seen at point ②, has the value $i_{c,H_2} = -2.208 \times 10^{-7}$ A/cm^2. The cathodic hydrogen evolution current density, seen at point ③, has the value $i_{c,H_2} = -3.745 \times 10^{-8}$ A/cm^2. The corrosion current density obtained from the sum of copper dissolution and deposition current densities is $i_{corr} = 3.745 \times 10^{-8}$ A/cm^2, corresponding to 1.2 nm/day. The calculated concentration at the electrode surface was $c_{Cu^{2+}}(0) = 2.646 \times 10^{-10}$ mol/cm^3.

The anodic copper dissolution reaction is balanced at the corrosion potential V_{corr} by the sum of hydrogen evolution and copper deposition reactions. The back deposition of copper occurs due to the accumulation of copper ions at the electrode surface. The copper dissolution and deposition reactions were not equal in magnitude because, as shown by Eq. (4–11), some of the copper ions diffuse away from the surface. In the usual application of Evan's diagrams, the cathodic reaction does not involve metal deposition and the corrosion current would be found from the intersection of the metal dissolution current and the cathodic current. In the present case, the cathodic current contains a dominant
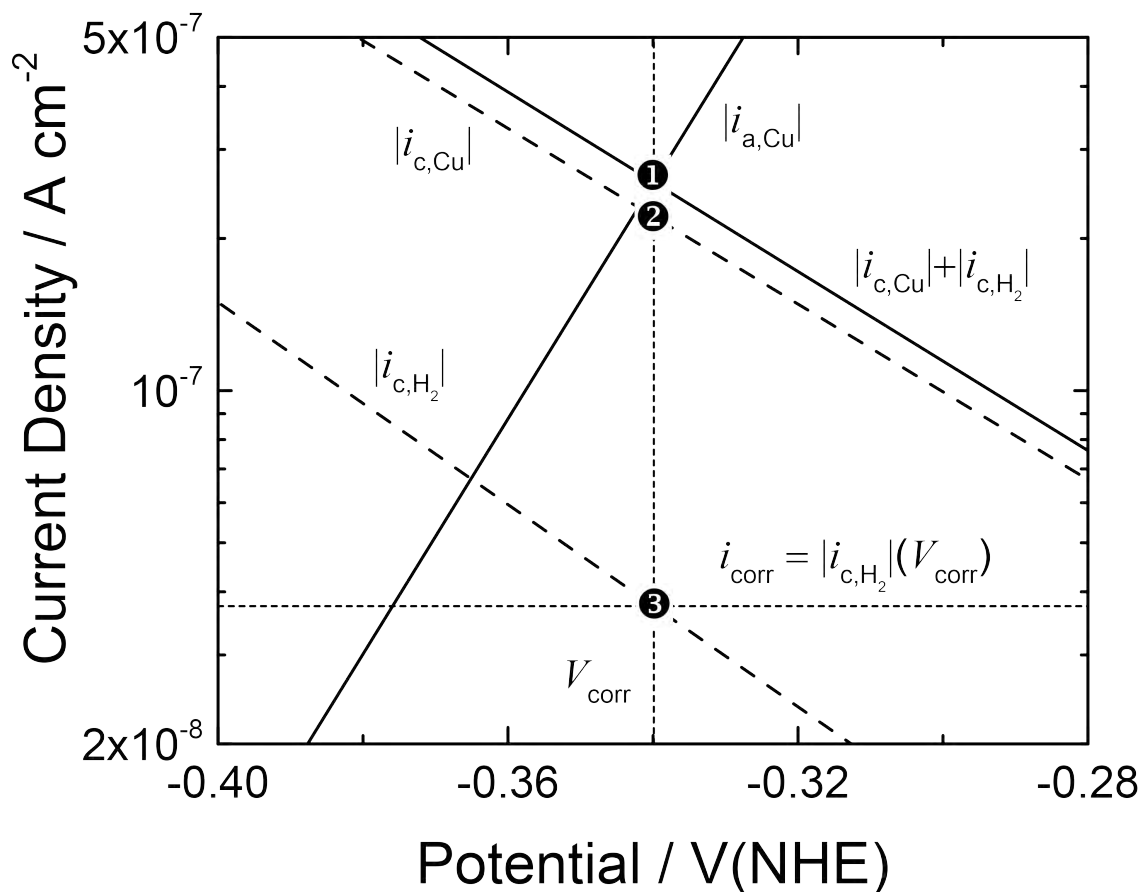
Figure 4-7. corresponding to parameter set D in Table 4-3. The solid lines correspond to the total cathodic current, $i_{c,Cu} + i_{c,H_2}$, and the anodic current $i_{a,Cu}$. The dashed lines represent the contributions of $i_{c,Cu}$ and i_{c,H_2}. The vertical line at the intersection of total cathodic and anodic current (point ①) represents the corrosion potential. The cathodic copper deposition current density at the corrosion potential is seen at point ②. The cathodic hydrogen evolution current density is seen at point ③. The corrosion current density, obtained from the difference between the copper dissolution current density at point ① and the copper deposition current density at point ②, is equal in magnitude to the cathodic hydrogen evolution reaction at the corrosion potential (point ③).
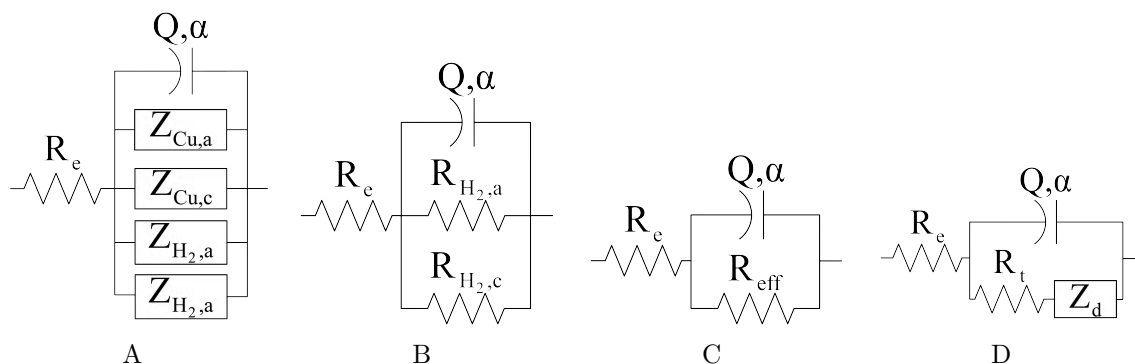
Figure 4-8. Equivalent electrical circuit models for the impedance data presented in Figure 4-4: A) general model showing the parallel contributions of all potential reactions; B) reduced model corresponding to the impedance data for gold and platinum electrodes; C) model corresponding to the impedance data for gold and platinum electrodes in terms of an effective resistance; D) model for the copper electrode.

contribution from the reverse reaction to metal dissolution. Thus, the corrosion current density is obtained from the difference, measured at the corrosion potential, between the copper dissolution current density and the magnitude of the copper deposition current density. The corrosion current is equal in magnitude to the cathodic hydrogen evolution reaction at the corrosion potential.

The oxidation of hydrogen formed by the cathodic hydrogen evolution reaction was not found to be significant, and inclusion of this reaction did not change the results presented in Figure 4-7. Once the hydrogen partial pressure is sufficient, the corrosion rate was found to be equal to zero. These results are in agreement with the observations of Macdonald and Sharifi-Asl.[40]

4.6.3 Impedance Regression Analysis

An impedance model for the data presented in Figure 4-8A should account for parallel contributions of the impedances associated with the charging current and the other reactions occurring for this system. An electrical circuit that provides a framework for such a model is presented could be expressed as Figure 4-8A.

Table 4-4. Regression results for the data presented in Figure 4-8A

Parameter	Au	Pt	Cu
R_{e}, kΩcm^2	5.85±0.07	4.93±0.05	9.6±0.5
Q, μF/s$^{(1-\alpha)}$cm^2	27.6±0.3	27.6±0.3	9.6±0.2
α, dimensionless	0.66±0.01	0.69±0.01	0.73±0.02
R_{eff}, kΩcm^2	790±210	750±170	–
R_{t}, kΩcm^2	–	–	95±12
k_{W}, μS s$^{1/2}$/cm^2	–	–	24± 0.2
C_{eff}, μF/cm^2	10.9	11.2	3.9

For the gold and platinum electrodes, the feasible reactions are hydrogen evolution and oxidation of the hydrogen thus produced. The circuit of Figure 4-8A is therefore reduced to Figure 4-8B, where charge-transfer resistances were used to describe the electrochemical reactions. As the two resistances in parallel cannot be distinguished, the circuit of Figure 4-8B must be expressed as Figure 4-8C where

$$R_{\text{eff}} = \frac{R_{\text{H}_2,\text{a}}R_{\text{H}_2,\text{c}}}{R_{\text{H}_2,\text{a}} + R_{\text{H}_2,\text{c}}} \tag{4–12}$$

The impedance is expressed as

$$Z_{\text{Au}} = R_{\text{e}} + \frac{R_{\text{eff}}}{1 + (2\pi\text{j}f)^\alpha Q R_{\text{eff}}} \tag{4–13}$$

and the fitting results are presented as lines in Figure 4-8A. The resulting parameters are provided in Table 4-4.

Several models were considered for the copper electrode. The circuit that provided the best representation of the experimental data is presented in Figure 4-8D, i.e.,

$$Z_{\text{Cu}} = R_{\text{e}} + \frac{R_{\text{t}} + 1/k_{\text{W}}\sqrt{2\pi\text{j}f}}{1 + (2\pi\text{j}f)^\alpha Q \left(R_{\text{t}} + 1/k_{\text{W}}\sqrt{2\pi\text{j}f}\right)} \tag{4–14}$$

The fitting results are presented as lines in Figure 4-8A, and the resulting parameters are provided in Table 4-4. This model suggests that the impedance associated with the corrosion and hydrogen evolution reactions were too large to contribute to the impedance response. The diffusion contribution presented in the model given as Figure 4-8D may
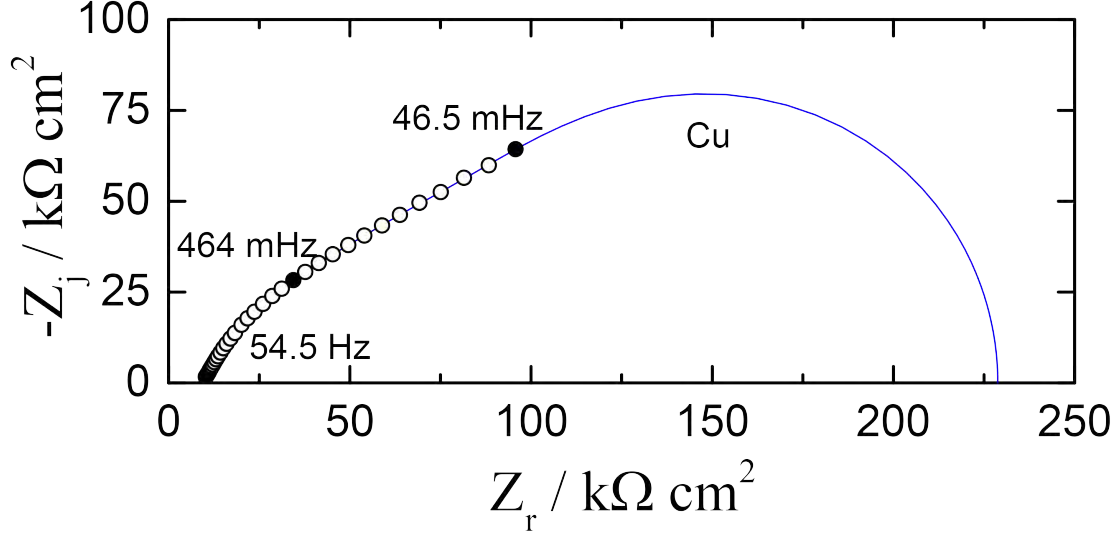
Figure 4-9. Measurement model extrapolation (blue line) of the copper impedance (circle) showing the predicted zero frequency limit.

be attributed to the deposition of copper, as shown in Figure 4-7. This hypothesis is supported by Bojinov et al.,[61] who observed back deposition of copper. As the measured frequency range was insufficient to allow determination of the diffusion time constant, the diffusing species could not be identified. At the zero-frequency limit, the polarization resistance is related to the corrosion density, i_{corr}, using the Stern-Geary equation,[72]

$$i_{\text{corr}} = \frac{-\beta_{\text{H}_2}\beta_{\text{Cu}}}{2.303 R_{\text{p}} \left(\beta_{\text{Cu}} - \beta_{\text{H}_2} \right)} \tag{4–15}$$

where β_{H_2} and β_{Cu} are the Tafel slope parameters obtained from literature.[62,71] As zero-frequency limit cannot be readily discerned from the impedance data, the regression results cannot provide an estimate for the corrosion rate. An estimation of an upper bound to the corrosion rate may, however, be provided. A measurement model[73] extrapolation of the data is presented in Figure 4-9. The estimation of the polarization resistance obtained from the measurement model for copper suggests that the corrosion rate must be smaller than 2.5 nm/day.

Three approaches were used to assign a physical meaning to the CPE parameters obtained by regression. As the absence of passivation behavior in the polarization curve

51

shown in Figure 4-5 suggests the absence of oxide films, the Brug formula[74]

$$C_{\text{eff}} = Q^{1/\alpha} R_e^{(1-\alpha)/\alpha} \qquad (4\text{--}16)$$

was used to estimate the capacitance associated with the CPE parameters Q and α. The use of the Brug formula is further supported by analysis of the geometry-induced nonuniform current and potential distributions expected for the electrode. Huang et al.[75] showed for a disk electrode that, above a dimensionless frequency

$$K = Q(2\pi f)^\alpha r_0 \rho = 1 \qquad (4\text{--}17)$$

nonuniform current and potential distributions influence the impedance response. The resulting impedance was described as a pseudo-CPE that was best modeled by the Brug formula.[76] The dimensionless frequency K is written in Eq. (4–17) as a function of the CPE coefficient Q, the angular frequency $2\pi f$ raised to the power of the CPE exponent α, the disk radius r_0, and the electrolyte resistivity ρ. For the present system, the characteristic frequency obtained from Eq. (4–17) was 1.6 Hz, meaning that above this frequency, the impedance was influenced by a surface distribution of ohmic resistance.

The values obtained for gold and platinum electrodes, shown in Table 4-4, are in good agreement with expected values for electrodes in deionized water. The capacitance obtained for copper was, however, smaller than expected for an electrode-electrolyte interface. A different set of calculations were performed to explore the hypothesis that the capacitance should be associated with an oxide film. If the CPE behavior is caused by the axially-distributed properties of an oxide film, the power-law model[77,78] provides the best method to associate CPE parameters to film properties.[79] Under the assumption that the film is Cu_2O (with a dielectric constant of 7.6)[80] and that the lower limit of the film resistivity is 1000 Ωcm, the film thickness would be on the order of 190 nm. Under the assumption that the film is CuO, with a dielectric constant of 18.1,[80] the film thickness

Table 4-5. Estimated values for copper corrosion rates.

Method	i_{corr}, mA/cm^2	i_{corr}, nm/day
Measurement model extrapolation of impedance	$< 7.9 \times 10^{-5}$	< 2.5
Kinetic Simulations	3.2×10^{-5}	1.1

would be on the order of 350 nm. As oxide films on copper are not expected to be thicker than 6 nm,[81] the interpretation based on the Brug formula seems most appropriate.

A third approach is to attribute the capacitance obtained from the Brug equation to a film. The film thickness so obtained would range from 1.7 for Cu_2O to 4.1 nm for CuO, which is within the range of expected values for an oxide on copper. If an oxide film is present, the polarization curve indicates that it is not protective.

4.7 Discussion

Several methods were employed in the present work to quantify the rate of copper corrosion in deaerated deionized water. The impedance analysis showed that the copper electrode behaved in a manner that was strikingly different from the gold and platinum electrodes. Thus, the impedance results suggest that the electrochemistry of copper must play a role. As the gold and platinum results were almost identical, the impedance response for these two materials should not be associated with the respective electrochemistry. The impedance data, therefore, support the hypothesis that corrosion of copper takes place in deaerated deionized water.An extrapolation of the impedance diagram to the zero-frequency limit suggests that the corrosion rate must be less than 2.5 nm/day (see Table 4-5).

The polarization curves presented in Figure 4-5 provided additional verification for the electrochemical activity of copper, but changes in the electrolyte during the experiment precluded accurate assessment of a corrosion current density. As shown in Table 4-5, the kinetic simulations suggest a corrosion rate of 1 nm/day, where kinetic parameters were obtained from electrolytes that may be considered surrogates for deionized water. The hypothesis that copper corrodes in deaerated deionized water

is further supported by the Pourbaix diagram calculated for the environment under investigation. In the present work, copper was shown to be thermodynamically unstable in deaerated deionized water; whereas, thermodynamic stability was predicted for copper in deaerated deionized water equilibrated with hydrogen gas at a pressure of 1 atm. A slight increase in the concentration of dissolved hydrogen at the electrode surface is suggested by the impedance response for the inert gold and platinum electrodes, but this was apparently not sufficient to stabilize the copper.

The result of the kinetic analysis is that, in the absence of hydrogen, a corrosion rate of 1 nm/day is predicted under anaerobic conditions. The impedance measurements did not provide an estimate of the corrosion rate, but yielded instead an upper bound of 2.5 nm/day. If oxygen were present in the experimental system, the concentration associated with the upper bound of 2.5 nm/day would have been 6.5 ppb. The dissolved oxygen concentration in the experimental system reported here was therefore less than 6.5 ppb and, likely, based on Henrys law arguments, substantially less. The oxygen concentration yielding a corrosion rate of 1 nm/day, equal to that predicted in the absence of oxygen, would be 2.5 ppb. The corrosion rate in water containing dissolved oxygen concentrations much lower than 2.5 ppb would still be 1 nm/day, so long as hydrogen is absent. Thus, the present work shows that, in the absence of hydrogen, copper will corrode on the order of 1 nm/day in deionized water with an O_2 concentration on the order of, or less than, 1 ppb.

The corrosion rates in the present work (under anaerobic conditions) are comparable in magnitude to the corrosion rate of the copper (at 15+ ppb O_2) cooling system used at the Argonne National Laboratory synchrotron.[63,64] Here we demonstrate that a detectable copper corrosion rate (under anaerobic conditions) still occurs and does so to a measurable degree. The present work also supports the claim that copper in deaerated deionized water will corrode if hydrogen is removed from the electrolyte, as was previously observed by Hultquist[2] and discussed as a theoretical possibility by Macdonald and Sharifi-Asl.[40] The

estimated corrosion rate is sufficiently small that it can be neglected for most technological applications. This rate, however, may be sufficient to cause failure of copper nanowicks employed in heat exchangers for high-performance electronics.

4.8   Concluding Remarks

A combination of impedance and polarization experiments and thermodynamic, kinetic, and impedance models were used to assess the tendency of copper to corrode in deaerated deionized water that did not contain hydrogen. The present work shows that copper will corrode at a very small rate. Kinetic simulations indicate that, for the present experimental conditions, the average rate over a period of one year would be on the order of 1 nm/day. The impedance analysis suggests that the corrosion rate is less than 2.5 nm/day. This corrosion rate will decrease as the concentration of hydrogen and copper increases. While the estimated corrosion rate may be inconsequential for most technological applications, the corrosion rate is large enough to influence the functionality of nanostructure utilized in emerging applications.

CHAPTER 5
REFINED KINETIC MODEL FOR COPPER CORROSION

In this chapter a refined kinetic model is developed to explore the influence of mass transfer, surface area to volume ratio, exchange current density and equilibrium potential have on the corrosion of copper in deaerated water. To explore the influence of system parameters, the simulations presented in Chapter 4 are extended in here to include the oxidation of hydrogen and diffusion of dissolved hydrogen away from the electrode surface.

5.1 Mathematical Development

The reactions considered at the copper electrode were dissolution and electroplating of copper

$$Cu \rightleftarrows Cu^{2+} + 2e^- \tag{5--1}$$

and hydrogen evolution and oxidation

$$2H^+ + 2e^- \rightleftarrows H_2 \tag{5--2}$$

Kinetic parameters were obtained from Stanković and Vuković[82] and Sharifi-Asla and Macdonald.[62]

The anodic current density for reaction (5--1) was expressed as

$$i_{a,Cu} = i_{0,Cu} \exp\left(b_{a,Cu}\left(V - V_{0,Cu}\right)\right) \tag{5--3}$$

where $V_{0,Cu}$ is the equilibrium potential for the copper reaction. The corresponding cathodic current density was expressed as

$$i_{c,Cu} = -\left(\frac{c_{Cu^{2+}}(0)}{c_{Cu^{2+}}(\text{ref})}\right)^{\gamma_{Cu}} i_{0,Cu} \exp\left(-b_{c,Cu}(V - V_{0,Cu})\right) \tag{5--4}$$

where the concentration term $c_{Cu^{2+}}(0)$ accounts for the concentration of cupric ion at the electrode surface and $c_{Cu^{2+}}(\text{ref})$ represents the concentration of cupric ion at which the exchange current density was obtained. The anodic hydrogen oxidation in Eq. (5--2) was

expressed as

$$i_{a,H_2} = \left(\frac{c_{H_2}(0)}{c_{H_2}(\text{ref})}\right)^{\gamma_{H_2}} i_{0,H_2} \exp\left(b_{a,H_2}(V - V_{0,H_2})\right) \tag{5-5}$$

where $c_{H_2}(0)$ is the concentration of dissolved hydrogen at the electrode surface and $c_{H_2}(ref)$ represents the concentration of hydrogen at which the exchange current density was obtained. The corresponding cathodic reaction was expressed as

$$i_{c,H_2} = -i_{0,Cu} \exp\left(-b_{c,H_2}(V - V_{0,H_2})\right) \tag{5-6}$$

where V_{0,H_2} is the equilibrium potential for the hydrogen evolution reaction.

The net rate of reaction (5–1) was expressed in terms of the concentrations at the electrode surface and far from the electrode surface by

$$i_{a,Cu} + i_{c,Cu} = nFk_{Cu^{2+}}\left(c_{Cu}(0) - c_{Cu}(\infty)\right) \tag{5-7}$$

where $k_{Cu^{2+}}$ is the mass transfer coefficient for cupric ions. The net rate of reaction (5–2) was expressed as

$$i_{a,H_2} + i_{c,H_2} = nFk_{H_2}\left(c_{H_2}(0) - c_{H_2}(\infty)\right). \tag{5-8}$$

where k_{H_2} is the mass transfer coefficient for dissolved hydrogen. The total current for the system was set equal to zero, i.e.,

$$i_{a,Cu} + i_{c,Cu} + i_{a,H_2} + i_{c,H_2} = 0 \tag{5-9}$$

The nonlinear set of equations Eq. (5–3) to Eq. (5–9) were solved at each time step for variables $i_{a,Cu}$, $i_{c,Cu}$, i_{a,H_2}, i_{c,H_2}, $c_{Cu^{2+}}(0)$, $c_{H_2}(0)$, and V.

An open system is defined here to be one in which the flow of inert gas removes the hydrogen formed by reaction (5–2). For an open system, the concentration of hydrogen far from the electrode at time step k was obtained from the corresponding value at time step $k-1$ from

$$c_{H_2}^{k}(\infty) = c_{H_2}^{k-1} \tag{5-10}$$

As the initial hydrogen concentration was equal to zero, Eq. (5–10) ensured that the concentration far from the electrode was fixed to a zero value. A closed system allowed the accumulation of hydrogen. For the closed system, the concentration of hydrogen far from the electrode at time step k was obtained from the corresponding value at time step $k - 1$ from

$$c_{H_2}^k(\infty) = c_{H_2}^{k-1}(\infty) - \frac{i_{a,H_2}^{k-1} + i_{c,H_2}^{k-1}}{nF} \frac{A}{V} \Delta t \tag{5–11}$$

For both open and closed systems, the concentration of cupric ions far from the electrode at time step k was obtained from the corresponding value at time step $k - 1$ from

$$c_{Cu^{2+}}^k(\infty) = c_{Cu^{2+}}^{k-1}(\infty) + \frac{i_{a,Cu}^{k-1} + i_{c,Cu}^{k-1}}{nF} \frac{A}{V} \Delta t \tag{5–12}$$

A time step of 1000 seconds was used for these simulations. For the closed system, the partial pressure of hydrogen in equilibrium with $c_{H_2}(\infty)$ was obtained using Henry's law, i.e.,

$$p_{H_2} = \frac{c_{H_2}(\infty)}{k_H^\circ} \tag{5–13}$$

where $k_H^\circ = 0.00078$ mol/kg bar.[83] The kinetic study was carried out using the 7 equations summarized in Table 5-1.

5.2   Mass-Transfer Coefficients

Mass–transfer coefficients were obtained from published correlations for the microelectrode used in our work[1] and the copper foils used in the work by Hultquist et al.[2] The relationship between the mass–transfer coefficient for cupric ions and dissolved hydrogen differed for the two cases because transport for the microelectrode was assumed to be controlled by diffusion and transport for the foils was assumed to be controlled by natural convection.

5.2.1   Microelectrode

For the microelectrode the mass transfer coefficient was obtained from the expression[84]

$$Sh_i = \frac{k_i d_{disk}}{D_i} = \frac{8}{\pi} \tag{5–14}$$

Table 5-1. Summary of equations used for the kinetic study. Time stepping used for this system is shown in the lower half of the table.

Description	Equation	Ref.
Anodic Current, Cu	$i_{a,Cu} = i_{0,Cu} e^{b_{a,Cu}(V - V_{0,Cu})}$	5–3
Cathodic Current, Cu	$i_{c,Cu} = -\left(\frac{c_{Cu^{2+}}(0)}{c_{Cu^{2+}}(ref)}\right)^{\gamma_{Cu}} i_{0,Cu} e^{-b_{c,Cu}(V - V_{0,Cu})}$	5–4
Anodic Current, H_2	$i_{a,H_2} = \left(\frac{c_{H_2}(0)}{c_{H_2}(ref)}\right)^{\gamma_{H_2}} i_{0,H_2} e^{b_{a,H_2}(V - V_{0,H_2})}$	5–5
Cathodic Current, H_2	$i_{c,H_2} = -i_{0,H_2} e^{-b_{c,H_2}(V - V_{0,H_2})}$	5–6
Mass Transfer, Cu	$i_{a,Cu} + i_{c,Cu} = nFk_{Cu^{2+}}(c_{Cu^{2+}}(0) - c_{Cu^{2+}}(\infty))$	5–7
Mass Transfer, H_2	$i_{a,H_2} + i_{c,H_2} = nFk_{H_2}(c_{H_2}(0) - c_{H_2}(\infty))$	5–8
Zero Net Current	$i_{a,Cu} + i_{c,Cu} + i_{a,H_2} + i_{c,H_2} = 0$	5–9
k-th Time Step, Open $H_2(\infty)$	$c_{H_2}^k(\infty) = c_{H_2}^{k-1}$	5–10
k-th Time Step, Closed $H_2(\infty)$	$c_{H_2}^k(\infty) = c_{H_2}^{k-1}(\infty) - \frac{i_{a,H_2}^{k-1} + i_{c,H_2}^{k-1}}{nF}\frac{A}{V}\Delta t$	5–11
k-th Time Step, $Cu(\infty)$	$c_{Cu^{2+}}^k(\infty) = c_{Cu^{2+}}^{k-1}(\infty) + \frac{i_{a,Cu}^{k-1} + i_{c,Cu}^{k-1}}{nF}\frac{A}{V}\Delta t$	5–12

where Sh_i is the dimensionless Sherwood number, k_i is the mass transfer coefficient of species i, d_{disk} is the diameter of the disk, and D_i is the diffusivity of species i. The mass transport represented in Eq. (5–14) is mathematically equivalent to spherical diffusion for a microelectrode. Thus, the mass transfer coefficients for cupric ions and dissolved hydrogen were related by

$$k_{H_2} = k_{Cu^{2+}} \frac{D_{H_2}}{D_{Cu^{2+}}} \tag{5–15}$$

The electrode diameter was 0.025 cm and the volume of water was 30 cm^3 yielding an area to volume ratio of $A/V = 1.64 \times 10^{-5}$ cm^{-1}. From Eq. (5–14), the mass transfer coefficient for cupric ions can be estimated to have a value of $k_{Cu^{2+}} = 7.33 \times 10^{-4}$ cm/s.

5.2.2 Hultquist Foils

The experimental systems reported by Hultquist et al.[2] consisted of copper foils with an exposed area of 85 cm^2 placed upright in a sealed vessel and immersed in anoxic water with a volume of 50 cm^3. Such a system may be expected to be driven by natural convection. A correlation for natural convection to a vertical plate is given as[85]

$$Sh_i = \frac{k_i L}{D_i} = 0.677 \, (Sc \, Gr)^{1/4} \tag{5–16}$$

where L is the length of the plate, $\mathrm{Sc} = \nu/D_i$ is the Schmidt number, and ν is the kinematic viscosity of the electrolyte. The term Gr is the Grashof number defined for $\rho(0) > \rho(\infty)$ as

$$\mathrm{Gr} = \frac{gL^3}{\nu^2}\left(1 - \frac{\rho(\infty)}{\rho(0)}\right) \tag{5–17}$$

where g is gravitational acceleration, ν represents the average electrolyte kinematic viscosity, $\rho(\infty)$ is the electrolyte density far from the electrode, and $\rho(0)$ is the electrolyte density at the electrode surface. Thus, for a system controlled by natural convection, the mass transfer coefficients for cupric ions and dissolved hydrogen were related by

$$k_{\mathrm{H}_2} = k_{\mathrm{Cu}^{2+}}\left(\frac{D_{\mathrm{H}_2}}{D_{\mathrm{Cu}^{2+}}}\right)^{3/4} \tag{5–18}$$

The electrode area to volume ratio was $A/V = 1.7~\mathrm{cm}^{-1}$. Under the assumption that the dimensionless density difference $1 - \rho(\infty)/\rho(0)$ is on the order of 10^{-9}, the mass transfer coefficient for cupric ions can be estimated to have a value of $k_{\mathrm{Cu}^{2+}} = 1 \times 10^{-5}~\mathrm{cm/s}$.

5.3   Results

The calculated results are presented for both open and closed systems. In the open system, hydrogen is removed by the flow of inert gas such that the bulk concentration of dissolved hydrogen may be assumed to be equal to zero. In the closed system, the accumulation of hydrogen results in the buildup of hydrogen partial pressure. Parameters used in the simulation are presented in Table 5-2.

5.3.1   Open System

The corrosion rate calculated for the microelectrode is compared to that obtained for the Hultquist cell in Figure 5-1 with mass–transfer coefficient as a parameter. For both the microelectrode and the Hultquist cell, results are presented as well for mass–transfer coefficients that are an order of magnitude larger and smaller than the corresponding calculated value. The calculated corrosion rate for the microelectrode was 1.1 nm/day and reached a value of 0.74 nm/day after 15 years; whereas, for the Hultquist cell, the calculated corrosion rate was initially about 0.37 nm/day and reached a value of 0.053
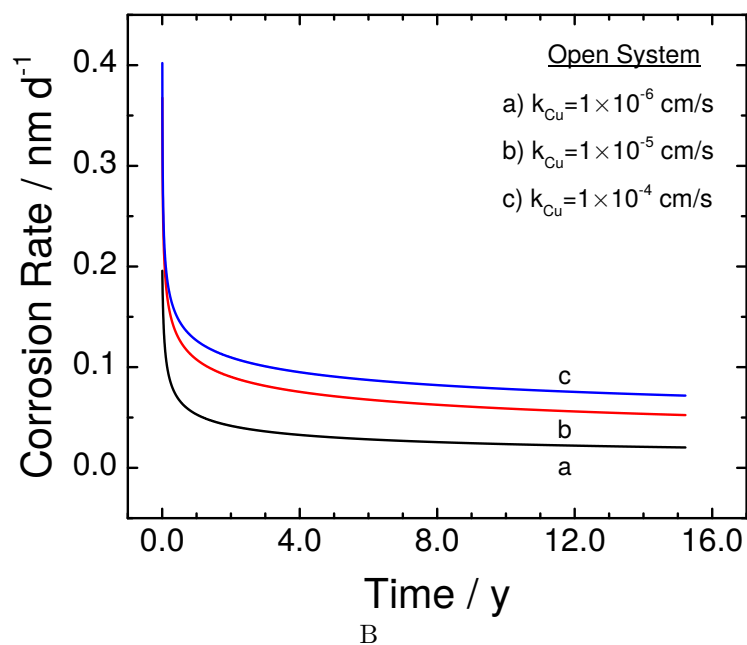
Figure 5-1. Calculated open–system corrosion rates as a function of time with mass–transfer coefficient as a parameter: A) for the microelectrode with $A/V = 1.64 \times 10^{-5}$ cm^{-1}; B) for the Hultquist cell with $A/V = 1.7$ cm^{-1}.

Table 5-2. Mass–transfer coefficients used in the simulations are presented as legends in the respective figures. Values for the equilibrium potential for the copper dissolution reaction were taken from Figure 1 of Stankovic[82] and adjusted to be referenced to the Normal Hydrogen Electrode. The kinetic parameters for the hydrogen evolution reaction were taken from Sharifi[62] for pH=0 and $p_{H_2} = 0.1$ atm. See Table III in Cleveland et al.[1]

Parameter	Value	Units
$V_{0,Cu}$	-0.1876	V(NHE)
$i_{0,Cu}$	9×10^{-4}	A/cm^2
$b_{a,Cu}$	20	1/V
$b_{c,Cu}$	53.56	1/V
γ_{Cu}	0.75	
V_{0,H_2}	-0.436	V(NHE)
i_{0,H_2}	3.28×10^{-7}	A/cm^2
b_{a,H_2}	38.38	1/V
b_{c,H_2}	24.24	1/V
γ_{H_2}	1	

nm/day after 15.2 years. The corrosion rate is shown to depend on the electrode area to volume ratio and on the mass–transfer coefficients.

The cumulative corrosion is presented as a function of time in Figure 5-2 for the microelectrode and Hultquist cells. After an elapsed time of 15 years, the cumulative corrosion for the microelectrode was estimated to be 4700 nm; whereas, the cumulative corrosion for the Hultquist cell was calculated to be 390 nm. Thus, using the same model for the kinetics, the calculation for cumulative corrosion that accounted for mass transfer and the electrode area to volume ratio yielded a cumulative corrosion for the microelectrode that was 12 times larger than for the Hultquist cell.

The influence of electrode area to volume ratio is evident in the concentration of cupric ion presented in Figure 5-3 for the microelectrode and Hultquist cells. The calculated bulk concentration of cupric ion reached a value of 9.3 μmol/cm^3 after 15 years in the Hultquist cell. In contrast, the calculated bulk concentration of cupric ion for the microelectrode reached a value of 1.0 nmol/cm^3 after 15 years in the Hultquist cell, which is 10,000 times smaller than that obtained for the Hultquist cell. The difference
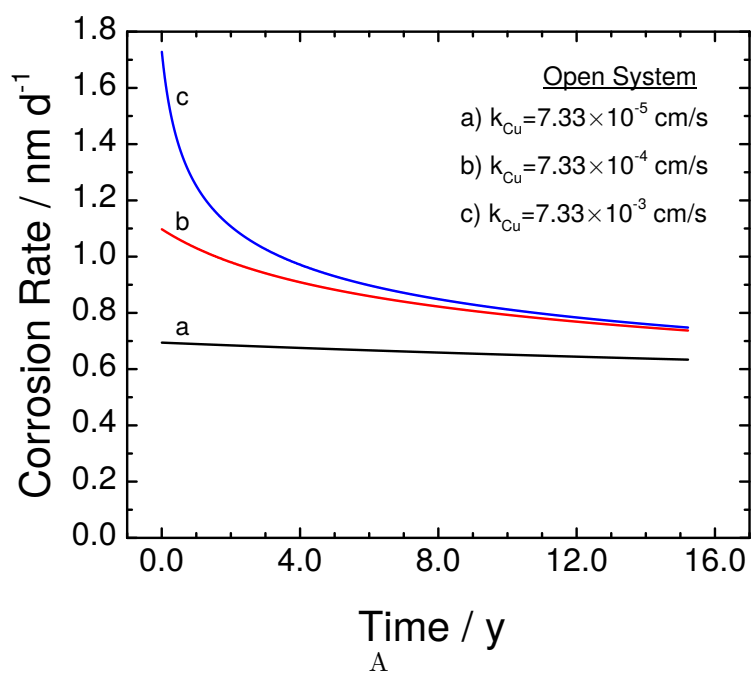
A

B

Figure 5-2. Calculated open–system cumulative corrosion as a function of time with mass–transfer coefficient as a parameter: A) for the microelectrode with $A/V = 1.64 \times 10^{-5}$ cm^{-1}; B) for the Hultquist cell with $A/V = 1.7$ cm^{-1}.

A

B

Figure 5-3. Calculated open–system bulk concentration of cupric ion as a function of time with mass–transfer coefficient as a parameter: A) for the microelectrode with $A/V = 1.64 \times 10^{-5}$ cm^{-1}; B) for the Hultquist cell with $A/V = 1.7$ cm^{-1}.

can be attributed to the different electrode area to volume ratios and to the difference in mass–transfer coefficients. For the open system, the bulk concentration of dissolved hydrogen was assumed to be equal to zero. Thus, the corrosion continues in both the microelectrode and Hultquist systems, even after a period of 15 years.

5.3.2   Closed System

The behavior of an open system may be expected to differ from that of a closed system, in which the concentration of dissolved hydrogen and the corresponding hydrogen partial pressure increases with time. The closed–system corrosion rate calculated for the microelectrode is compared to that obtained for the Hultquist cell in Figure 5-4 with mass–transfer coefficient as a parameter. For both the microelectrode and the Hultquist cell, results are presented as well for mass–transfer coefficients that are an order of magnitude larger and smaller than the corresponding calculated value. The calculated corrosion rate for the microelectrode was 1.1 nm/day and reached a value of 0.74 nm/day after 15 years, essentially unchanged from the results of the open system shown in Figure 5-1A. In contrast, the corrosion rate calculated for the Hultquist cell was initially about 0.35 nm/day and dropped to a value near zero in less than 60 days. The insensitivity to the open or closed condition for the microelectrode may be attributed to the small electrode area to volume ratio. The sharp decrease in the corrosion rate in the closed Hultquist cell can be attributed to the larger electrode area to volume ratio.

The corresponding cumulative corrosion is presented as a function of time in Figure 5-5 for the microelectrode and Hultquist cells. After an elapsed time of 15 years, the cumulative corrosion for the closed–system microelectrode was unchanged from that in the open system; whereas, the cumulative corrosion for the Hultquist cell was calculated to be 2.7 nm. Thus, using the same model for the kinetics, the calculation for cumulative corrosion that accounted for mass transfer and the electrode area to volume ratio yielded a cumulative corrosion for the microelectrode that was 1700 times larger than for the Hultquist cell.
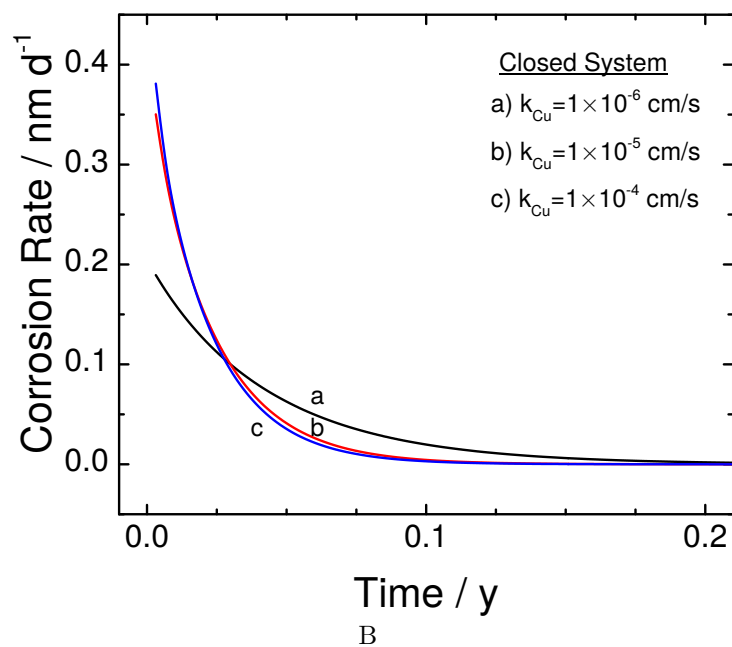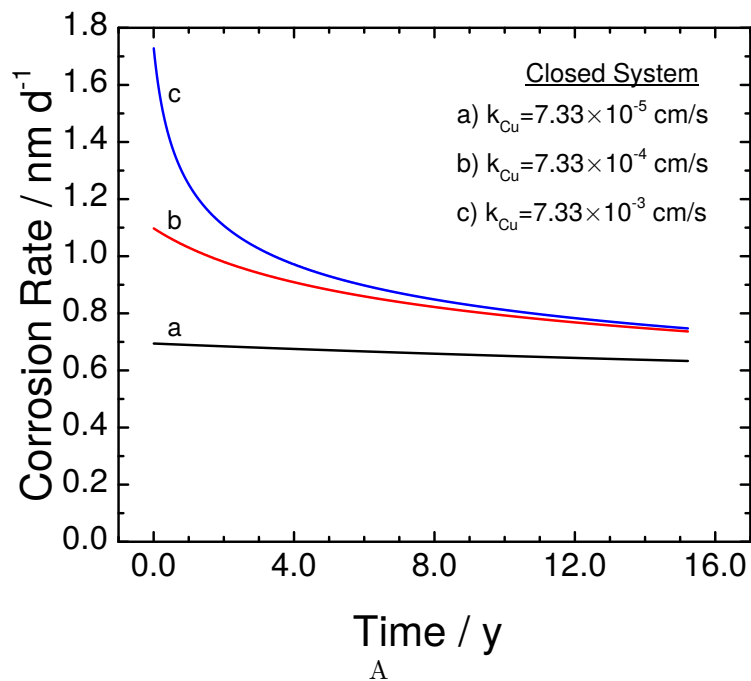
Figure 5-4. Calculated closed–system corrosion rates as a function of time with mass–transfer coefficient as a parameter: A) for the microelectrode with $A/V = 1.64 \times 10^{-5}$ cm^{-1}; B) for the Hultquist cell with $A/V = 1.7$ cm^{-1}.
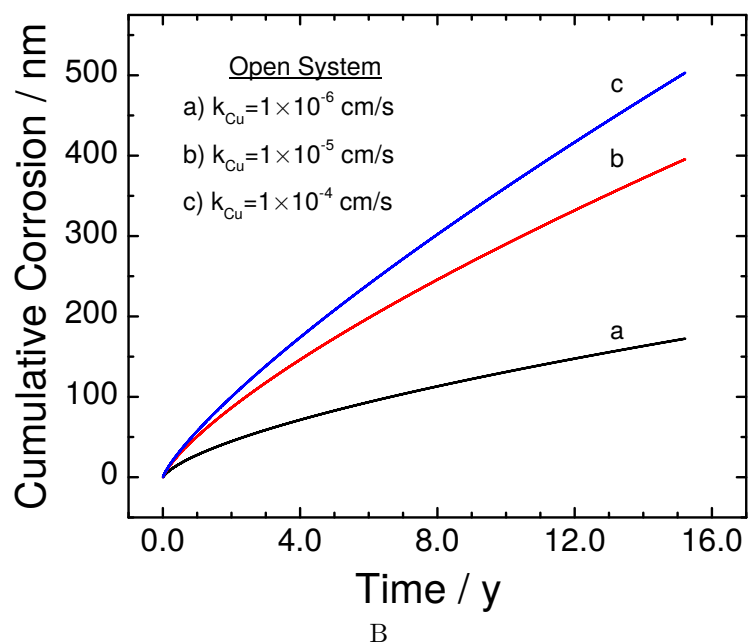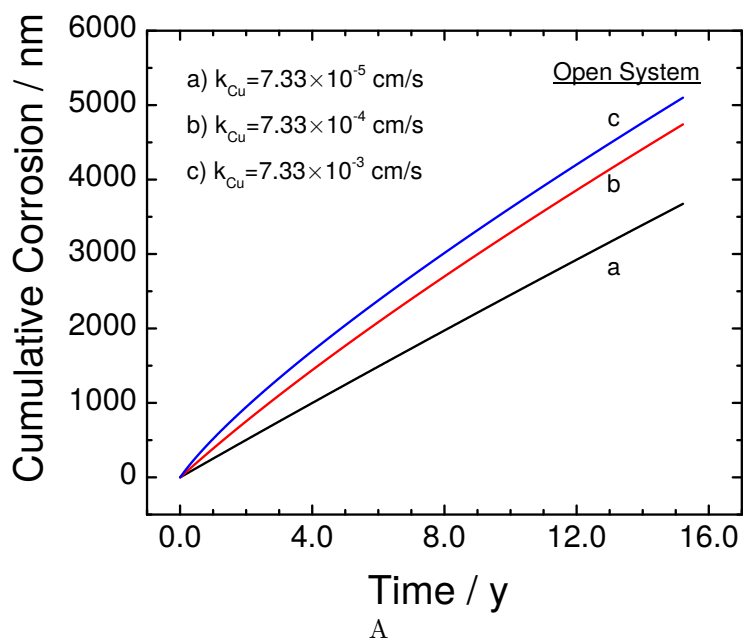
66
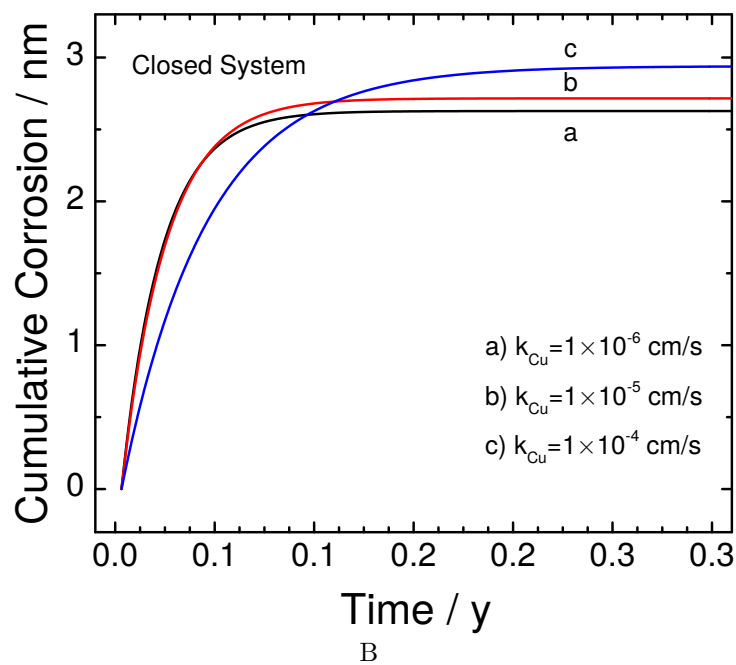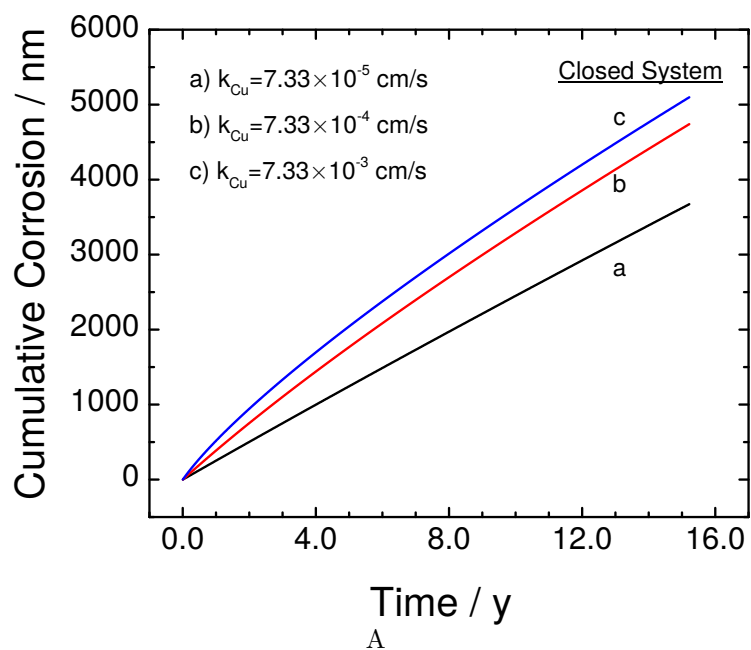
Figure 5-5. Calculated closed–system cumulative corrosion as a function of time with mass–transfer coefficient as a parameter: A) for the microelectrode with $A/V = 1.64 \times 10^{-5}$ cm^{-1}; B) for the Hultquist cell with $A/V = 1.7$ cm^{-1}.
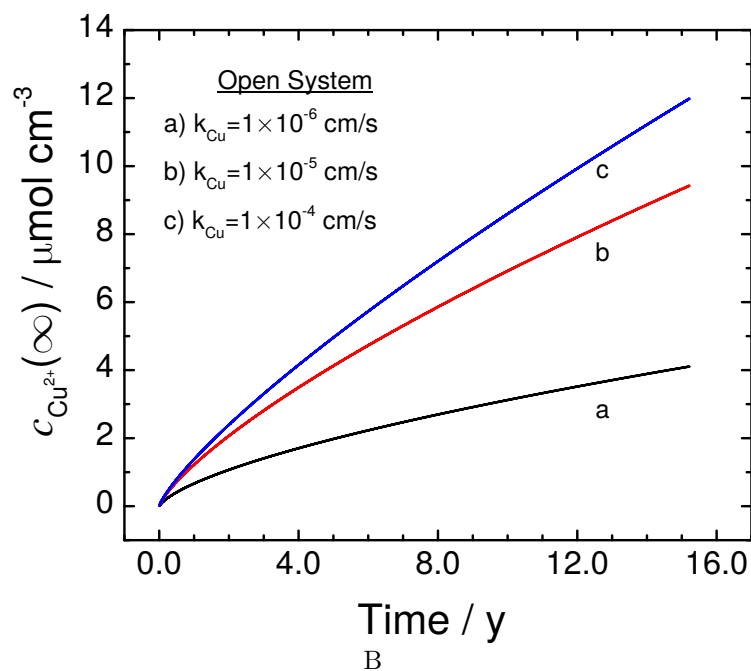
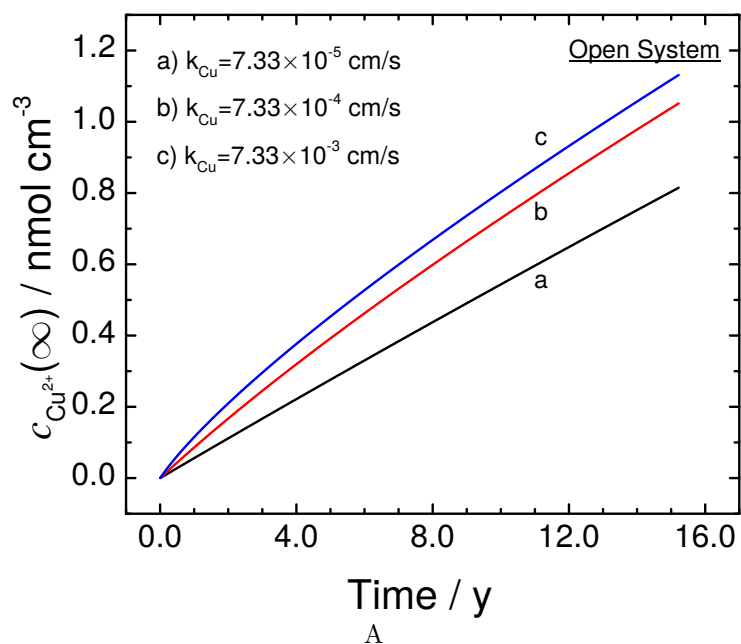The influence of electrode area to volume ratio is evident in the concentration of cupric ion presented in Figure 5-6 for the microelectrode and Hultquist cells. The calculated bulk concentration of cupric ion in the Hultquist cell reached a value of 75 nmol/cm^3, much smaller than the 9.3 μmol/cm^3 reached in the open system after 15 years. In contrast, the calculated bulk concentration of cupric ion for the microelectrode after 15 years was unchanged as compared to the open system. The difference in behavior between the microelectrode and Hultquist systems is due to the difference in electrode area to volume ratio.

The major difference between the open and closed system is that the hydrogen partial pressure is allowed to increase in a closed system. The hydrogen partial pressure, calculated from the bulk concentration of dissolved hydrogen, is presented in Figure 5-7 as a function of time for the microelectrode and Hultquist cells. The Henry's law constant used for this calculation were obtained from Sander.[83] After less than 60 days, the calculated closed–system hydrogen partial pressure reached a limiting value of 0.096 atm; whereas, in the closed microelectrode system, the hydrogen partial pressure did not reach a limiting value and, after 15 years, reached a value of 0.0013 atm. The limiting value of hydrogen partial pressure was found to be independent of mass–transfer coefficient and exchange current density, but did depend on the equilibrium potential used.

A clearer understanding of the calculations performed in the present work may be obtained from the calculated corrosion current–potential relationship presented in Figure 5-8 for the Hultquist cell under open and closed condition. For the closed system, the corrosion current density approaches a value of zero at a potential of -0.284 V(NHE). This value is independent of mass–transfer coefficient and is in good agreement with the Pourbaix diagrams presented in Figure 5-9. For the open system, the corrosion current density decreases as the potential increases. The equilibrium condition is not achieved as the accumulation of hydrogen is prevented.
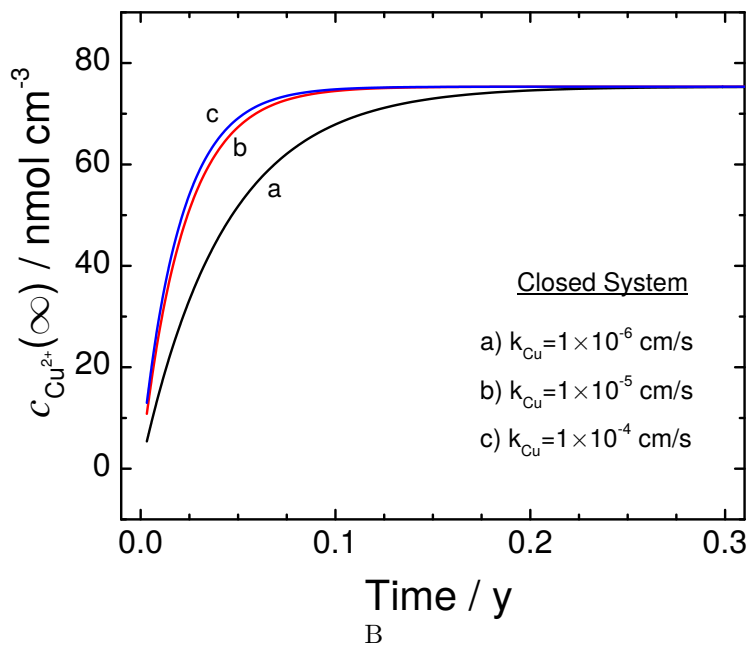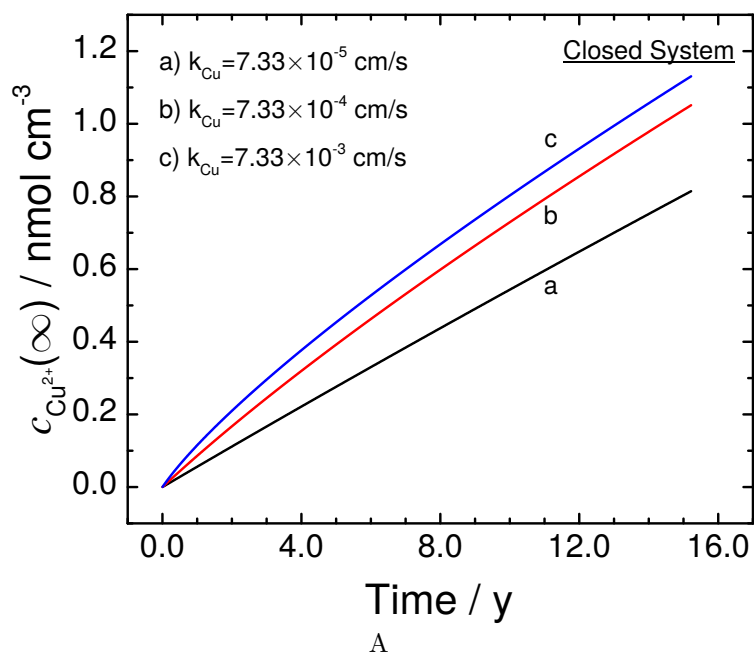
Figure 5-6. Calculated closed–system bulk concentration of cupric ion as a function of time with mass–transfer coefficient as a parameter: A) for the microelectrode with $A/V = 1.64 \times 10^{-5}$ cm^{-1}; B) for the Hultquist cell with $A/V = 1.7$ cm^{-1}.
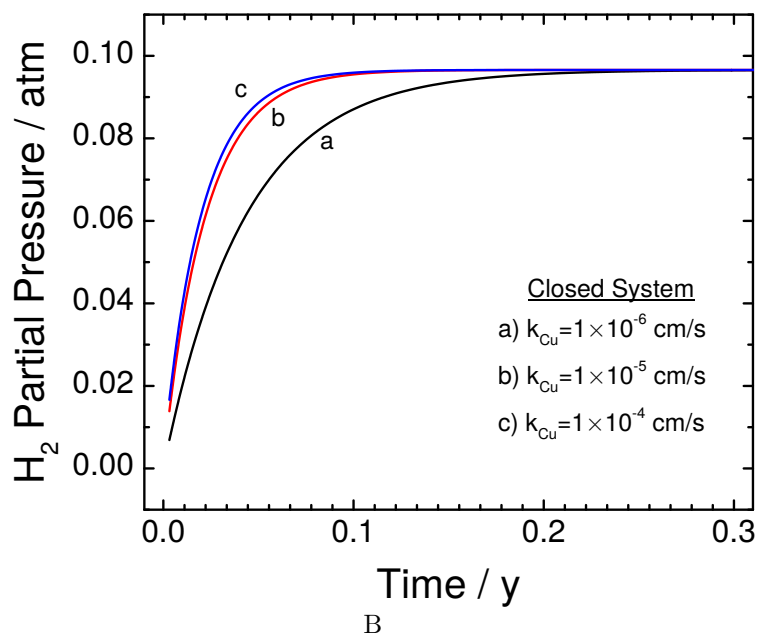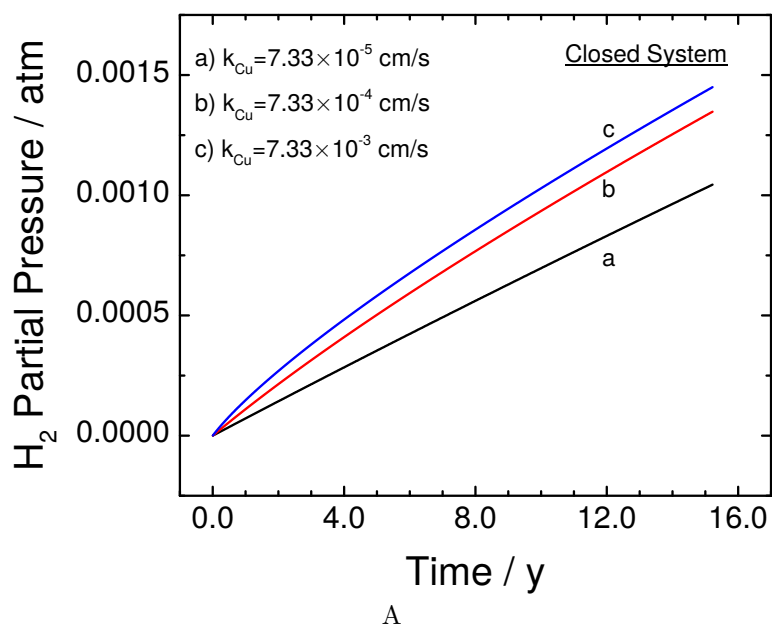
Figure 5-7. Calculated closed–system bulk hydrogen partial pressure as a function of time with mass–transfer coefficient as a parameter: A) for the microelectrode with $A/V = 1.64 \times 10^{-5}$ cm^{-1}; B) for the Hultquist cell with $A/V = 1.7$ cm^{-1}.
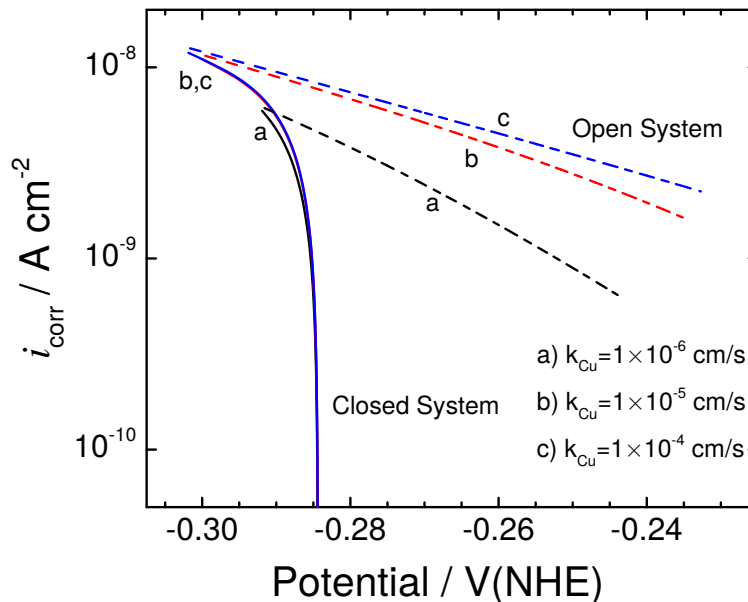
Figure 5-8. Calculated corrosion current density as a function of potential for the Hultquist cell under open and closed condition with mass–transfer coefficient as a parameter.

The calculated limiting hydrogen partial pressure of 0.096 atm is substantially larger than the value of 0.45 mbar reported by Hultquist et al.[86] In addition, the corrosion rate estimated in the present work for the Hultquist system is smaller than the rate reported by Hultquist et al.[86] This discrepancy may be attributed to experimental issues or to the need to modify the model parameters. The model reported in the present work did not account for the contribution of the head space. The hydrogen pressure was assumed to be that in equilibrium with the bulk concentration of dissolved hydrogen. Thus, the measured hydrogen pressure may be expected to be lower than that calculated. The presence of a large head space would cause the system to behave as an open system at short times and as a closed system as the partial pressure of hydrogen increases in the head space.

The agreement between the simulations performed in the present work to those presented in Cleveland et al.[1] validate the assumption made that the hydrogen oxidation reaction could be neglected for the small electrode area to volume ratio and short times considered. The hydrogen oxidation reaction plays an essential role in simulating

the behavior of the Hultquist cell with its larger electrode area to volume ratio and experiments of longer duration. For both the open and closed systems, the cumulative corrosion is reduced for larger electrode area to volume ratios.

The difference in estimated corrosion rates between our work[1] and that Hultquist et al.[2] is shown in the present work to be the natural consequence of the manner in which kinetics, mass transfer, and electrode area to volume ratio influence the progression toward the equilibrium condition.

5.4 Controversy Surrounding Nuclear Waste Storage

Proponents to the storage of spent nuclear waste believe that copper provides a suitable waste containment for periods exceeding a million years. One of these proponents raised concerns to the copper corrosion work discussed in Chapter 4. The revised kinetic model provided in this chapter was carried out to address the concerns raised by K. Spahiu and I. Puigdomenech at the Swedish Nuclear Fuel and Waste Management Company. This section will highlight the objections raised by Spahiu and Puigdomenech and address these objections with the results from the revised kinetic model.

In their *Comment on Nanometer-scale corrosion of copper in de-aerated deionized water [J. Electrochem. Soc., 161, C107 (2014)]*, Spahiu and Puigdomenech raise three principal objections:

1. Figure 5 in Cleveland et al.[1] does not properly represent the dependence of line "b" on the partial pressure of oxygen. In addition, the middle redox potential (ORP) presented in Figure 5 differs from the value calculated by Spahiu and Puigdomenech;

2. Spahiu and Puigdomenech suggest that trace amounts of oxygen in the experiment may be sufficient to explain the derived corrosion rates from the experiments performed;

3. Spahiu and Puigdomenech express concern that the observed corrosion rate by Cleveland et al.[1] is around three orders of magnitude higher than the rate that may be derived from the observations published by Hultquist et al.[2,86]

From these criticisms, Spahiu and Puigdomenech posit that the work of Cleveland et al.[1] "may not be considered to support the claim that copper will corrode in deaerated

deionized water if hydrogen is removed." Our response to these critiques are presented below.

5.4.1 Thermodynamic Analysis

Spahiu and Puigdomenech are correct to observe that line (b) shown in Figure 5 of our work does not properly represent the three cases discussed. Our presentation of a single Pourbaix diagram with three oxidation/reduction potentials overlaid was intended to show that copper is stable in anoxic water in the presence of hydrogen but has a tendency to corrode in water containing oxygen or in anoxic water that is free of hydrogen. Cleveland et al. agree that presentation of three Pourbaix diagrams individually would have lessened cause for confusion.

The original Pourbaix diagrams for the three cases, generated by CorrosionAnalyzer 2.0 (Build 2.0.16) by OLI Systems Inc.,[67,68] are shown in Figure 5-9. As Spahui and Puigdomenech state, the potential for the oxygen line (b) is dependent on the pH and partial pressure of O_2 following

$$E_{\text{SHE}} = 1231 \text{ mV} - 59.16 \text{ pH} + 59.16 \left(\log \text{ p}_{O_2} \right) / 4 \qquad (5\text{--}19)$$

Line (b) moves in the negative direction as the partial pressure of O_2 is decreased. Our calculations show the potential is 1.185 V(NHE) at a pH of 0 when the partial pressure of O_2 is minimized by a N_2 blanket. At a partial pressure of 0.21 atm, the potential is 1.219 V(NHE) at pH=0. The model used to produce the (b) line is in agreement with Eq. (5–19).

It is important to understand the distinction between the ORP and the lines represented by the letters (a) and (b). The ORP is a mixed potential with simultaneous forward and backward components with contributions from the metal/metal ion/multiple metal ion oxidation states (e.g. Cu/Cu[I]/Cu[II]), H_2/H^+, and some additional $O_2/OH^-/H_2O$ reactions. The lines (a) and (b) describe only one half-reaction each, and, therefore, describe only a thermodynamic limit in the absence of polarization. The ORP is the
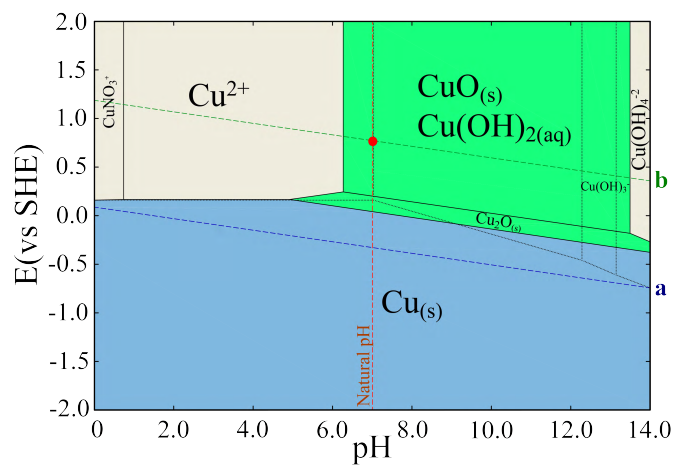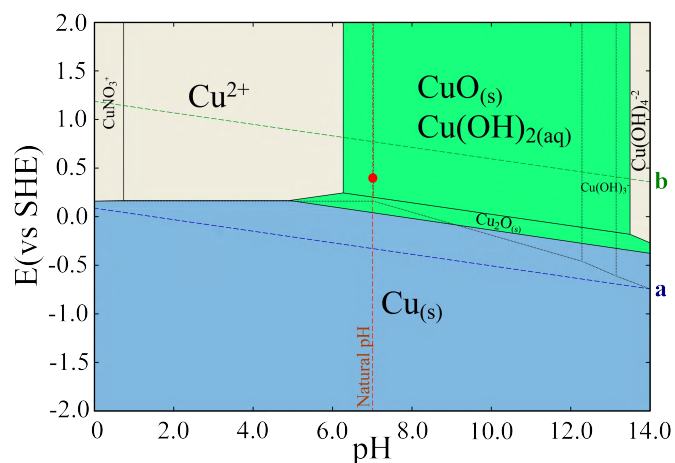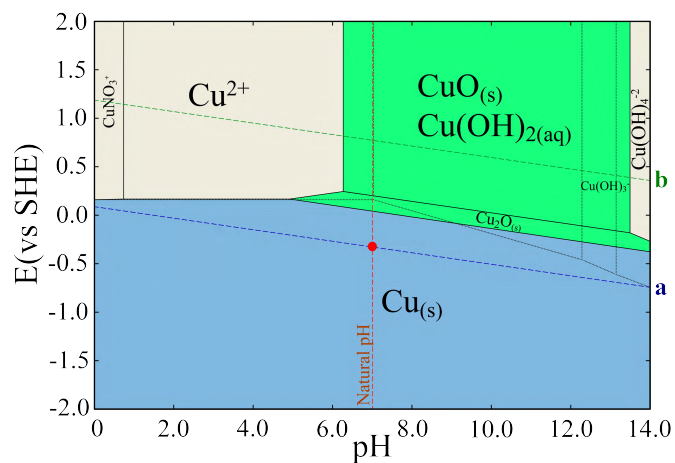
Figure 5-9. Calculated potential-pH (Pourbaix) diagrams for copper in deaerated deionized water generated by CorrosionAnalyzer 2.0 (Build 2.0.16) by OLI Systems Inc:[67,68] A) in the presence of 8ppm dissolved O_2; B) in the absence of dissolved H_2 and O_2; and C) in the absence of dissolved O_2 and in the presence of dissolved H_2. The titrants were NaOH and HNO_3.

potential associated with the equilibrium state between several such reactions such that the charge is balanced among all participating reactions.

The ORP of the system calculated by the OLI software includes effects of the copper metal activity as well as the partial pressures of O_2 and H_2. The ORP shown as circles in Figure 5-9 includes the effects of the redox reaction required to get the solution to the stated Cu activity (1×10^{-6} M by default) and includes the influence of the generated H_2 and/or O_2. In the absence of dissolved oxygen and hydrogen, as shown in Figure 5-9B, the ORP has a value of 0.403 V(NHE).

Spahiu and Puigdomenech correctly point out that the species Cu^+ identified in the upper left corner in our Pourbaix diagram was in error. As shown in Figure 5-9, the correct species is $CuNO_3^+$ when using NaOH and HNO_3 as titrants.

In summary, the concerns raised by Spahiu and Puigdomenech that the use of a single Pourbaix diagram oversimplified the thermodynamics and that a species was incorrectly labeled are justified. The calculation of the ORP in our work, however, is correct. The calculation of the ORP in the Pourbaix diagrams was used to demonstrate that, in the absence of hydrogen, copper may corrode in anoxic water. The concerns raised by Spahiu and Puigdomenech do not invalidate the results presented in Cleveland et al.[1]

5.4.2 Trace Amounts of Oxygen

The copper microelectrode system was maintained under positive pressure with high-purity nitrogen and the oxygen content of the gas phase leaving the system was measured to be on the order of 1 ppb. The Henry's constant for this system (see reference Sander[83]) would suggest that, under equilibrium conditions, the dissolved oxygen concentration in water should be less than 1 ppt. Nevertheless, it is widely recognized that it is difficult to achieve perfect anoxic conditions.

The main features of the experimental results found in Cleveland et al.[1] can be summarized as follows:

1. Impedance diagrams showed reactivity that was not present for gold or platinum electrodes.

2. The impedance diagrams could not be used to extract a corrosion rate. Only an upper bound for the corrosion rate could be estimated.

3. The high-frequency part of the impedance spectrum was analyzed to show that the constant-phase element evident in the impedance response could not be attributed to an oxide film on the copper. The constant-phase element parameters were shown to be consistent with a surface distribution.

The impedance results motivated the kinetic analysis that was used to estimate a corrosion rate. The impedance was not used to quantify a corrosion rate. The absence of an oxide film and the inability to quantify a corrosion rate suggests, however, that deaeration was achieved to a high degree.

In summary, the concern on trace amounts of oxygen expressed by Spahiu and Puigdomenech have no bearing on the conclusions drawn in our paper.

5.4.3   Comparison to Work of Hultquist et al.

The concern expressed by Spahiu and Puigdomenech was that our estimated corrosion rate is around three orders of magnitude higher than that derived from the observations published by Hultquist et al[2,86] This discrepancy may be readily understood by recognizing that the approach to the equilibrium condition is governed by kinetic parameters such as rate constants, mass-transfer coefficients, and the electrode area to volume ratio. To explore the influence of system parameters, the simulations presented in our paper[1] were extended to include the oxidation of hydrogen and diffusion of dissolved hydrogen away from the electrode surface.

5.5   Concluding Remarks

We consider the comment on the thermodynamic analysis to be justified in the sense that, while our thermodynamic analysis was correct, it could have been presented more clearly. The comment on the possible presence of oxygen in our experiments does not

influence the conclusion of our paper as our conclusion was based on simulation results using parameters extracted from the literature. The impedance results were used only to show that an oxide film was not present on the copper electrode and to provide an upper bound for the corrosion rate of 2.5 nm/day. The comment that the difference in estimated corrosion rates between our system and that of Hultquist somehow invalidates our results is shown in the present work to be without basis. The difference in estimated corrosion rates is the natural consequence of differences between the two systems.

CHAPTER 6
INFLUENCE OF RING ELECTRODE ON EIS

6.1   Frequency Dispersion in Electrochemical Systems

Electrode geometry has been demonstrated to cause frequency dispersion in the electrochemical impedance response for various systems of different electrode geometry.[87] In 1970, Newman[88] showed frequency dispersion was present for the disk electrode system. Frequency dispersion has been shown to be associated with surface roughness[89] and with distribution of electrode properties.

It has been shown that there is a characteristic dimension associated with the electrode geometry that indicates the frequency at which dispersion is seen. For a disk electrode the characteristic dimension is the radius of the disk.[87,90,91] For roughness, the characteristic dimension is a function of the rugosity and the period of the roughness.[89] For distribution of the capacitance it has been shown to be period of the capacitance distribution.[92]

Frequency dispersion arises in a system with a nonuniform current distribution across the electrode surface. For the case of a disk working electrode embedded in an infinite insulate plane with a hemispherical counterelectrode located at infinity, Alexander et al.[89] define a characteristic frequency to be

$$K = \frac{\pi}{4} \frac{\omega C_0 r_0}{\kappa}.$$
(6–1)

where C_0 is the interfacial capacitance, κ is the solution conductivity and r_0 is the radius of the disk. The characteristic length of the disk electrode may be expressed as

$$\ell_{c,\text{disk}} = \frac{\pi}{4} r_0$$
(6–2)

The usefulness of Eq. (6–1) becomes apparent when determining the characteristic frequency at which dispersion influences the impedance response for a disk electrode. Huang et al.[87] showed the characteristic frequency for a disk electrode occurs near

$K = 1$. For $K > 1$ frequency dispersion occurs due to a nonuniform current distribution. Therefore, frequency dispersion may be eliminated in a desired frequency range by choosing the appropriate parameters C_0, r_0 and κ to ensure $K < 1$.

The characteristic dimension for a rough electrode is expressed as[89]

$$\ell_{c,\text{rough}} = f_r^2 P \tag{6--3}$$

where P is defined as the period of the roughness. Alexander et al.[92] showed that a capacitance distribution gave rise to frequency dispersion, but that the effect was seen at frequencies higher than that associated with the disk geometry. The characteristic length for a periodic distribution as a function of the radial coordinate was the period of the distribution such that

$$\ell_{c,\text{cap}} = P \tag{6--4}$$

and, as the period decreased, the frequency dispersion occurred at higher frequencies.

The objective of this work is to develop a relation for the characteristic dimension associated with the impedance response of a ring electrode. Edge effects from a nonuniform current distribution will be considered for primary resistance and impedance. Identification of a characteristic dimension can be used to avoid frequency dispersion in a carefully chosen system matching a set of parameters.

6.2 Rotating Electrodes

6.2.1 Steady State Response

Rotating disk electrodes (RDE), rotating ring electrodes (RRE), and rotating ring-disk electrodes (RRDE) all play an important role in the study of electrochemical systems. Origins of the ring-disk electrode can be traced back to experiments performed by Frumkin et al.[93] and Frumkin and Nekrasov[94] where a rotating disk electrode fitted with an isolated metal ring was found to be a suitable modification for investigating the formation of intermediate electrochemical products. Under convective-diffusion conditions, reduction of oxygen was carried out in an alkaline solution. The purpose of these early

experiments was to detect and identify the electroactive intermediate species and final products. Subsequent theory was developed by Ivanov and Levich[95] that expressed the limiting current density distribution on the ring electrode. Albery and Bruckenstein[96] improved upon the solution for the collection efficiency of a ring-disk electrode system using different boundary conditions.

Smyrl and Newman[97] investigated the error involved in treating the ring-disk system as a sectioned electrode for measuring the current distribution. Integrals were evaluated for the rotating ring-disk electrode for three cases and the concentration and current distributions were derived for each region on the RRDE surface. Miksis and Newman[98] calculated the primary current distribution for the ring-disk system. In this work they provided the three primary resistances for the ring-disk system as a function of two geometric ratios. Pierini and Newman[99] investigated the current distribution and concentration profiles on a RRDE below the limiting current.

The limiting behavior for a thick ring electrode was observed by Gregory and Riddiford[100, 101] which was initially investigated by blocking off a center portion of a disk electrode. Levich[102] (p. 107) derived the diffusional flux to the surface of a ring electrode (disk electrode with a lacquer coated center) remarking that the solutions are analogous to those for the semi-infinite plate. Pierini and Newman[103] presented the primary and secondary current distributions for the "isolated" ring or RRE system.

6.2.2   Impedance Response

Early AC theory for the ring-disk electrode was developed by Albery et al.[104] The phase shift and amplitude factor was studied at different rotational speeds and AC frequencies. At the time experimental results for the ring-disk system under AC modulation could only be achieved for frequencies up to 70 Hz.[105] Since then very little theoretical work has been done for the impedance response of RRE or RRDE.

Numerous experimental studies are presented in the literature. Absorption of reacting intermediates were studied using AC impedance at different potentials in the

active-to-passive transition range of Fe-Cr in 0.5 M H_2SO_4.[106,107] The cycling behavior of Li-ion batteries was studied using a 3-electrode system.[108] Ring counter and working electrodes were aligned concentrically to a disk reference electrode and the impedance response was measured. Gold rotating ring-disk electrodes were used to determine the diffusion coefficient of the borohydride anion commonly used as the analyte in Direct Borohydride Fuel Cells (DBFC).[109]

Gabrielli et al.[110] investigated the dissolution mechanism of copper in a chloride medium using a RRDE to simultaneously measure impedance and mass changes using a quartz microbalance. Cimenti[111,112] investigated distortions in the impedance based on cell geometry, electrode reactivity and relaxation times in SOFC. Two parallel disk electrodes were arranged concentrically to a thin ring reference electrode.

Thin concentric ring electrodes were used to model epidermal and subdermal impedances.[113] Results from this study were used in developing protocol for concentric ring experiments and in the rejection of results based on the presence of artifacts. Ring-shaped interdigital electrodes (RSIDEs) were used as an electrochemical biosensor for measuring the concentration of HbA1c levels in diabetic patients.[114] Impedance simulations of segmented cylindrical electrodes were used to study edge effects and edge-to-edge current interactions.[115] Using a finite element model the authors were able to quantify the effects geometry had on current and potential distributions for segmented deep brain stimulation electrodes used for targeting neuronal excitation during therapy.

Thermally and electrochemically induced interfacial surface alterations were studied by Jiang[116] using a ring-disk system. In this work the ring was treated as the reference electrode. Kovacs et al.[117] demonstrated that ac perturbation based detection is possible for the ring-disk electrodes. In this work the authors correlate the capacitance changes of a gold ring to the polarization of the thin polymer film on the disk.

Frequency dispersion effects due to current distribution resulting in error of the reaction resistance were modeled using ring-disk electrode.[118] A comparison in Ref. 118

to Ref. 87 is made where the authors indicate that the frequency dispersion can not be described as CPE behavior since the phase angle is changing continuously in the intermediate frequency range. No alternative to the use of apparent Constant-Phase-Element behavior is provided.

6.3 Mathematical Development

In this section expressions are developed for the primary resistance of the ring electrode. Presented here is an empirical expression describing the dimensionless frequency of the ring electrode in terms the geometric parameters r_1 and r_2. The expression for the dimensionless frequency of a ring is analogous to the disk dimensionless frequency in Eq. (6–1). The ring serves as the working electrode, which is embedded in an infinite, insulated plane with a hemispherical counterelectrode located at infinity.

6.3.1 Ring Electrode Primary Resistance

For the present work, the ring electrode is most naturally described using an axisymmetric cylindrical coordinate system where the solution is dependent on the radial position r along the electrode surface and the normal to the electrode surface, y. The ring electrode has an inner and outer radius of r_1 and r_2, respectively.

The current distribution on a ring proposed by Miksis and Newman[98] varies with the radial position and is described by

$$\frac{i_r}{i_{ave}} = \frac{2}{\sqrt{1 - x^2}} \tag{6–5}$$

where

$$x = \frac{r - r_1 - r_2}{r_2 - r_1} \tag{6–6}$$

Total current to the ring electrode is obtained by directly integrating Eq. (6–5) from r_1 to r_2

$$I_r = 2\pi i_{ave} \int_{r_1}^{r_2} i_r r dr = \pi^2 i_{ave}(r_2^2 - r_1^2) \tag{6–7}$$

The potential in the plane of the ring is expressed as

$$\Phi_0(r) = \frac{2}{\pi \kappa} \int_{r_1}^{r_2} i_r(r') \frac{K(m)}{r + r'} r' dr' \tag{6-8}$$

where i_r is defined in Eq. (6–5), K is the complete elliptical integral of the first kind[98] and m is the elliptic parameter. The complete elliptical integral of the first kind, K, shown in Eq. (6–8) is defined by

$$K(m) = \int_0^{\frac{\pi}{2}} \frac{d\alpha}{\left(1 - m \sin^2\alpha\right)^{1/2}} \tag{6-9}$$

where α is the eccentricity.

The ratio of the potential shown in Eq. (6–8) to the total current shown in Eq. (6–7) is often defined as the primary resistance. For this system the primary resistance can be expressed in terms of two limiting cases. The primary resistance for a thick ring where $0 \le \frac{r_1}{r_2} < 0.909$

$$
\begin{aligned}
\kappa r_2 R_{\text{ring}} = \frac{\pi}{8} &\left[\cos^{-1}\left(\frac{r_1}{r_2}\right) + \left(1 - \left(\frac{r_1}{r_2}\right)^2\right)^{1/2} \tanh^{-1}\left(\frac{r_1}{r_2}\right) \right]^{-1} \\
&\times \left[1 + 0.0143\left(\frac{r_1}{r_2}\right) \tanh^3\left(1.28\frac{r_2}{r_1}\right)\right]^{-1}
\end{aligned}
\tag{6-10}
$$

The primary resistance for a thin ring where $0.909 \le \frac{r_1}{r_2} \le 1$

$$\kappa r_2 R_{\text{ring}} = \frac{1}{\pi^2}\left(1 + \frac{r_1}{r_2}\right)^{-1} \ln 16 \left(\frac{1 + \frac{r_1}{r_2}}{1 - \frac{r_1}{r_2}}\right) \tag{6-11}$$

equation 6–10 and equation 6–11 represent the primary resistance for the two limiting cases of the ring electrode. These equations account for the real component of the impedance associated with the ring electrode seen at high frequency.

Similar limiting expressions have been developed by Miksis and Newman[98] and Pierini and Newman[103] where the dimensionless resistance of the thick ring approaches the

dimensionless resistance of the disk electrode.

$$\kappa r_2 R_{\mathrm{ring}} = 0.25 \qquad (6\text{--}12)$$

Miksis and Newman[98] use a thin ring limit that is assumed to approach the behavior of the finite length plane electrode embedded in an insulator.

$$\kappa r_2 R_{\mathrm{ring}} + \frac{1}{2\pi^2}\ln\left(1 - \frac{r_1^3}{r_2^3}\right) = \frac{\ln 96}{2\pi^2} \qquad (6\text{--}13)$$

Bruckenstein and Martinchek[119] provide an expression for the limiting behavior of the primary resistance without assuming a finite length plane electrode.

The expressions for the limiting primary resistance for the ring electrode are equivalent to those presented by Bruckstein and Martinchek[119] and can be verified with the physics handbook Gray.[120]

6.3.2 Ring Electrode Impedance Response

The potential distribution of an electrolyte with uniform conductivity is governed by Laplace's equation

$$\nabla^2 \Phi = 0. \qquad (6\text{--}14)$$

On the surface a disk working electrode embedded in an infinite, insulated plane with a hemispherical counterelectrode located at infinity. The disk is most naturally described using an axisymmetric cylindrical coordinate system where the solution is dependent on the radial position r along the electrode surface and the normal to the electrode surface, y.

The potential is zero for distances far away from the disk,

$$\Phi \to 0 \;\; \mathrm{as} \;\; r^2 + y^2 \to \infty \qquad (6\text{--}15)$$

and because the current density on the insulating plane embedding the ring is zero, the normal of the potential gradient must also be zero,

$$\left.\frac{\partial \Phi}{\partial y}\right|_{y=0} = 0 \;\; \forall \;\; r > r_1 \qquad (6\text{--}16)$$

The potential can be expressed in terms of steady-state $\bar{\Phi}$ and oscillating $\tilde{\Phi}$ components

$$\Phi = \bar{\Phi} + \mathrm{Re}\{\tilde{\Phi}e^{\mathrm{j}\omega t}\}. \tag{6–17}$$

Similarly, the potential applied at the electrode surface can be expressed in terms of steady-state $\bar{V}$ and oscillating $\tilde{V}$ components

$$V = \bar{V} + \mathrm{Re}\{\tilde{V}e^{\mathrm{j}\omega t}\}. \tag{6–18}$$

For a blocking electrode, Huang et al.[87] show the flux condition at the surface of a disk electrode can be expressed as,

$$i = \mathrm{C}_0 \frac{\partial\,(V - \Phi_0)}{\partial t} = -\kappa \frac{\partial \Phi}{\partial y}\Big|_{y=0} \tag{6–19}$$

where C_0 is the interfacial capacitance and κ is the solution conductivity.

Using equations Eq. (6–17), Eq. (6–18) and Eq. (6–19) the flux boundary condition for the blocking electrode surface can be expressed in the frequency domain as

$$\tilde{i} = \mathrm{j}\omega\mathrm{C}_0\left(\tilde{V} - \tilde{\Phi}\right) \tag{6–20}$$

where the oscillating component $\tilde{V}$ represents the applied potential perturbation at the electrode to a system with an oscillating potential in the electrolyte represented by $\tilde{\Phi}$.

6.4 Numerical Method

The finite element analysis (FEA), solver and simulation software COMSOL Multiphysics was used to solve Laplace's equation in cylindrical coordinates for the ring electrode. The governing equation is provided in Eq. (6–14) and is subject to the boundary conditions at infinity shown in Eq. (6–15). The boundary condition for the insulating plane is provided in Eq. (6–16) and the boundary conditions at the electrode surface shown in Eq. (6–20).

Due to the singularities that arise near the ring electrode's edges, a nonuniform meshing scheme was implemented near the surface of the ring electrode. A schematic
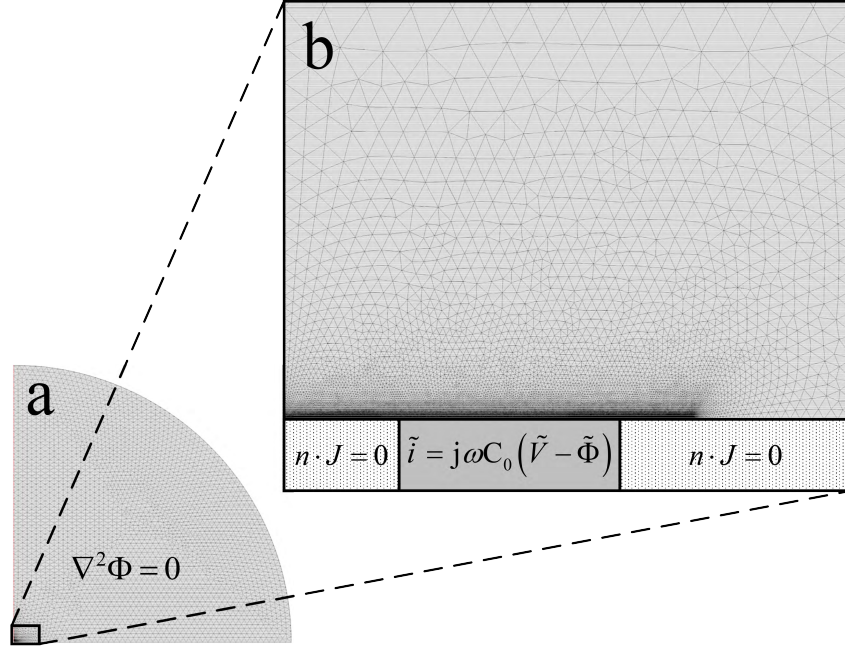
Figure 6-1. Schematic representation of finite element mesh used for the ring electrode simulations: a) entire domain ; b) enlarged region depicting the two insulating surfaces and the ring electrode surface.

representation of finite element mesh used for the ring electrode simulations is provided in Figure 6-1 detailing: a) entire domain; b) enlarged region depicting the two insulating surfaces with boundary condition $n \cdot J = 0$ and the ring electrode surface with boundary condition $\tilde{i} = \mathrm{j}\omega \mathrm{C}_0 \left(\tilde{V} - \tilde{\Phi} \right)$.

The counter electrode in figure 6-1 (a) for these simulations at a distance 500-1000 times that of the outer ring radius as to avoid errors associated with a nonuniform current distribution. A nonuniform free triangular mesh was chosen where the mesh density increases the closer to the ring electrode. The ring electrode consists of two edges r_1 and r_2. The exposed ring electrode surface is coplanar to the inner and outer insulating surfaces.

6.5   Results and Discussion

The results of the COMSOL simulations are presented to show the influence geometry has on the impedance response for the ring electrode. An approximate characteristic dimension is proposed and then improved upon to achieve greater accuracy with

Table 6-1. Parameters, values, and description used for the FEA simulations.

Parameter	Value	Description
C_0	0.02 F/m^2	interfacial capacitance
κ	2 S/m	electric conductivity
$\tilde{V}$	0.01 V	potential perturbation
r_1/r_2	Table 6-2	ring inner radius to outer radius

Table 6-2. Computed values of primary resistance as a function of the geometric parameters r_1 and r_2.

r_1/r_2	$\kappa r_2 R_{thick\ ring}$ (Eq. 6–10)	$\kappa r_2 R_{thin\ ring}$ (Eq. 6–11)	$\kappa r_2 R_{rr}$ (Ref. 98)	$Z_r(\omega \to \infty)$ (FEA)
0.10000	0.24998	-	0.2500	0.24997
0.25000	0.25034	-	0.2503	0.25029
0.33333	0.25109	-	-	0.25110
0.40000	0.25215	-	0.2523	0.25219
0.50000	0.25485	-	-	0.25490
0.60000	0.25944	-	0.2590	0.25946
0.66667	0.26402	-	-	0.26397
0.75000	0.27229	-	-	0.27231
0.80000	0.27932	-	0.2785	0.27925
0.90	-	-	0.3045	-
0.90909	-	0.30873	-	0.30871
0.95	-	-	0.3343	-
0.95238	-	0.33661	-	0.33661
0.97561	-	0.36757	-	0.36757
0.98	-	-	0.3770	-

the introduction of a correction factor ϵ_{corr}. The parameter values characterizing the electrochemical system used for the simulations are provided in Table 6-1.

6.5.1 Validation of Primary Resistance for the Ring Electrode

The purpose of this section is to validate the primary resistances calculated with that found in the literature. Our contributions are provided in Figure 6-2 which include the FEA simulations and theory resulting in the limiting cases provided in Eq. (6–10) and Eq. (6–11). These results are compared with the work of Miksis and Newman.[98] All of these values are summarized in Table 6-2.
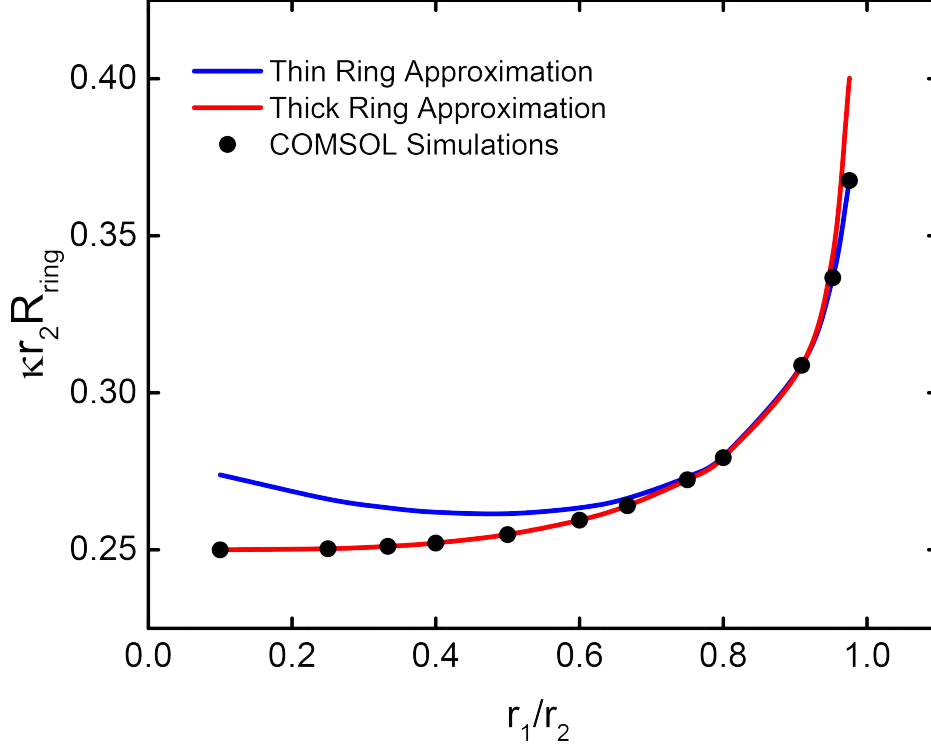
Figure 6-2. Computed values of primary resistance as a function of the geometric parameters r_1 and r_2 obtained from Eq. (6–10) and Eq. (6–11). Primary resistances in Table 6-2.

6.5.1.1 Thick Ring, Thin Ring and FEA Results

Computed values of primary resistance as a function of the geometric parameters r_1 and r_2 are provided in Table 6-2. Columns 2 and 3 represent the theoretical results obtained from Eq. (6–10) and Eq. (6–11) which are in excellent agreement with the FEA simulations at high frequency shown in column 5 of Table 6-2. The resistance values calculated from Eq. (6–10) and Eq. (6–11) and shown in Table 6-2 are in agreement for 4 to 5 significant digits with the FEA simulations performed for the ring electrode.

Justification for the use of two limiting cases for the thick and thin ring resistances is provided in Figure 6-2. The blue line represents the thin ring primary resistances limiting solution calculated using Eq. (6–10) and is valid for $0.909 \leq \frac{r_1}{r_2} \leq 1$. The red line represents the thick ring primary resistances limiting solution calculated using Eq. (6–11) and is valid for $0 \leq \frac{r_1}{r_2} < 0.909$. Our COMSOL simulations demonstrate the need for

the two limiting cases considered in Eq. (6–10) and Eq. (6–11). The blue thin line is in excellent agreement with our simulation results. However, when thin ring approximation is used for thick rings ($r_1/r_2 < 0.909$), the blue line is no longer valid which is clear from the deviation in Figure 6-2. Similarly, the thick ring limiting behavior is only representative of the FEA results for $\frac{r_1}{r_2} \geq 0.909$.

6.5.1.2   Thick Ring, Thin Ring and FEA Results

Miksis and Newman[98] tabulate primary resistance values as dimensionless correlations as functions of the ratio of radii for the disk and ring electrode. It should be noted that the values in Table 6-2 column 4 from the work of Miksis and Newman are for a ring electrode with the presence of a very small disk. The disk is sufficiently small to have a negligible effect on a ring electrode resistance values used for this comparison.

For thick rings ($r_1/r_2 = 0.1, 0.25$) the resistance values calculated from Eq. (6–10) and the FEA simulations are in agreement for the 4 significant figures tabulated by Miksis and Newman.[98] For rings having intermediate thicknesses ($r_1/r_2 = 0.4, 0.6, 0.8$) the resistance values calculated from Eq. (6–10) and the FEA simulations are in agreement for 3 significant figures to those tabulated by Miksis and Newman.[98]

The thin ring work of Miksis and Newman[98] is not directly comparable since the parameter ratios r_1/r_2 are not exactly the same. For our work we use thick ring ratios of $r_1/r_2 = 0.90909, 0.95238, 0.97561$ whereas Miksis and Newman use $r_1/r_2 = 0.90, 0.95, 0.98$. Nonetheless, thick rings with thicknesses ($r_1/r_2 = 0.90909, 0.95238, 0.97561$) have resistance values calculated from Eq. (6–11) and the FEA simulations are in agreement for 2 significant figures to those tabulated by Miksis and Newman.[98]

6.5.2   Interpretation of Impedance Response

Impedance simulations are presented to show the influence geometry has on ring electrodes embedded within an insulating plane. Impedance results are shown for a ring electrode as a function of frequency and as a function dimensionless frequency. Dimensionless results are used to determine the characteristic lengths and frequencies
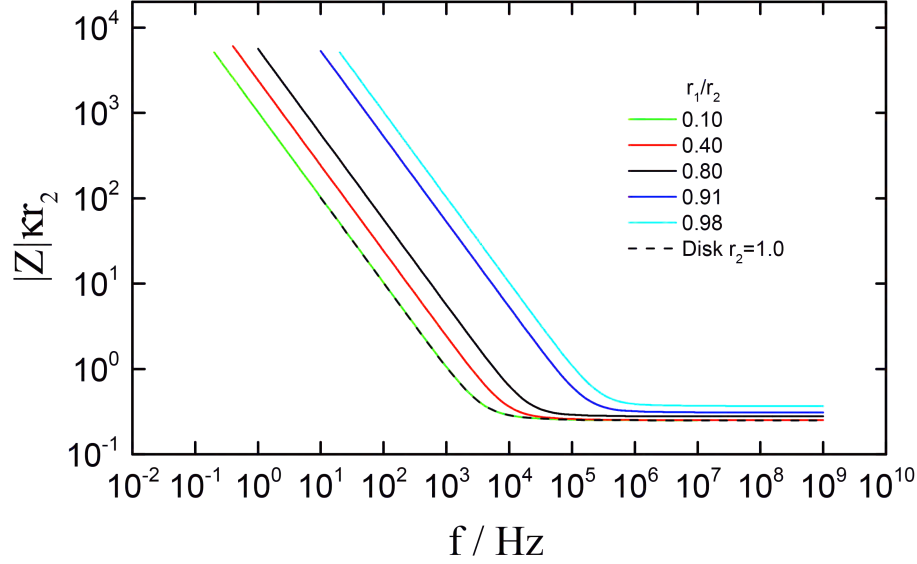
Figure 6-3. Ring electrode scaled modulus impedance as a function of frequency.
Frequency dispersion is dependent on the geometric parameter r_1/r_2.

associated with dispersion. Characteristic frequencies for the ring electrode are compared to the characteristic frequencies for the disk electrode.

The impedance of a ring electrode was simulated to show the effect of geometric parameters r_1 and r_2 has on the nonuniform current distributions resulting from ring geometry. The dimensionless scaled modulus impedance was calculated as a function of dimensional frequency is provided in Figure 6-3. The dimensionless modulus impedance for thickest ring electrodes at low frequency was smaller than the impedance of the thicker ring electrodes. The smaller impedance of the thick ring electrodes can be attributed to the larger surface area. Furthermore, the thick ring dimensionless modulus impedance should approach the impedance seen for a disk electrode. For a fixed outer radius r_2 and as $r_1 \rightarrow 0$ (ie $r_1/r_2 \rightarrow 0$) the impedance of the thick ring approached the impedance of the disk electrode. Similarly, the ring electrode dimensionless modulus impedance increases as $r_1 \rightarrow r_2$ (ie $r_1/r_2 \rightarrow 1$).
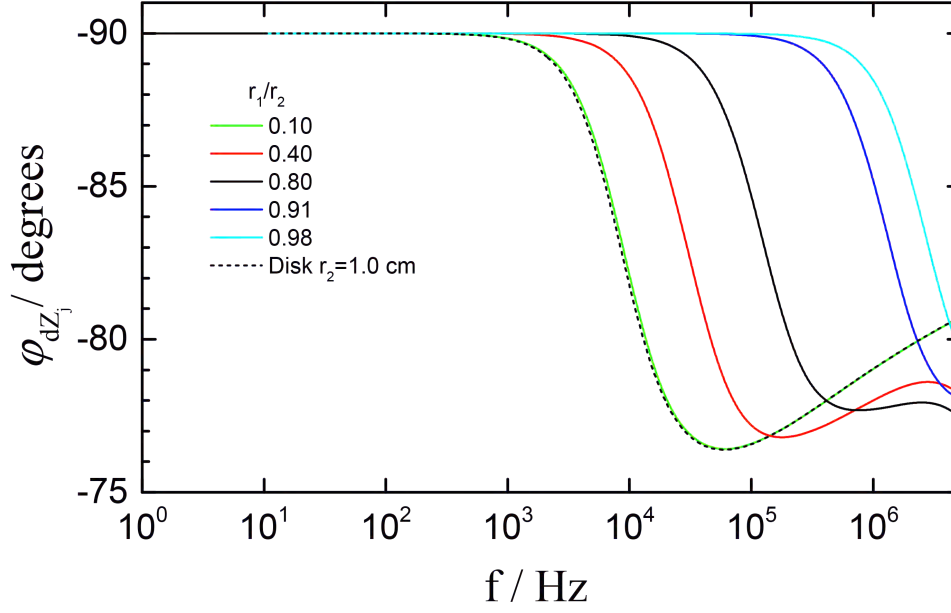
Figure 6-4. Ring electrode imaginary-impedance-derived phase angle as a function of
frequency shown for the ratio of radii, r_1/r_2.

6.5.2.1 Imaginary-Impedance-Derived Phase Angle

The imaginary-impedance-derived phase angle was defined by Alexander et al.[89] as

$$\varphi_{\mathrm{d}Z_j} = \frac{\mathrm{dlog}(Z_j)}{\mathrm{dlog}(f)} \times 90°.\qquad(6\text{–}21)$$

When compared to other definitions of phase angle, the imaginary-impedance-derived
phase angle is more sensitive to the onset of frequency dispersion.

The ring electrode imaginary-impedance-derived phase angle as a function of
frequency is presented in Figure 6-4. Frequency dispersion is dependent on the geometric
parameter r_1/r_2. At frequencies less than 1000 Hz the geometry of the ring does not
introduce any frequency dispersion. However, the onset of frequency dispersion for
frequencies greater than 1000 Hz occurs first for the thickest ring with $r_1/r_2 = 0.1$. As
the ring band distance decreases the observed onset of frequency dispersion occurs at a
higher frequency. This trend is consistent with imaginary-impedance-derived phase result
presented in Figure 6-4 and the scaled modulus impedance presented in Figure 6-3.

6.5.2.2 Empirical Formula

Based strictly on the observation that the onset of frequency dispersion varies according to the ring electrode's thickness divided by a factor accounting for curvature, we propose the following empirical formula. This is presented as an approximation for the dimensionless frequency

$$K = \frac{\pi}{4} \frac{\omega C_0}{\kappa} \left(\frac{r_2 - r_1}{1 + r_1^2/r_2^2} \right) \tag{6–22}$$

where r_1 and r_2 are the inner and outer radius of the ring, respectively. Comparing the dimensionless frequency for the ring in Eq. (6–25) to that of the disk in Eq. (6–1) it can be seen that the geometric parameter r_0 has been replaced by the estimated characteristic length

$$\ell_{c,ring} = \frac{\pi}{4} \left(\frac{r_2 - r_1}{1 + r_1^2/r_2^2} \right). \tag{6–23}$$

The estimated characteristic length in Eq. (6–23) is a ratio of the ring thickness $(r_2 - r_1)$ to a factor accounting for the ratio of the radii $(1 + r_2^2/r_1^2)$. The imaginary-impedance-derived-phase angle as a function of dimensionless frequency for ring electrode is presented in Figure 6-5 and is shown for five radii ratios, r_1/r_2 and a disk electrode with $r_2 = 1.0$ cm. Figure 6-5A is shown for the dimensionless frequency range 10 mHz to 10 Hz and Figure 6-5B is shown for the dimensionless frequency range 100 mHZ to 1.8 Hz.

In Figure 6-5B at $K = 1$, all 5 ring electrodes have an imaginary–impedance–derived phase angle greater than that of the disk electrode (limiting case of $r_1 \rightarrow 0$). At the edge of the disk electrode the presence of a nonuniform current and potential distribution results in a frequency dispersion for $K > 1$. For a ring electrode the edge effects are enhanced by the contribution of the inner ring edge and outer ring edge. The presence of more edge distance along both circumferences of the ring when compared to the disk results in a higher contribution to frequency dispersion at lower frequencies as is seen in Figure 6-5. The opposite trend is observed when plotted for a dimensional frequency as is seen in Figure 6-4. When plotting the dimensional frequency, as is done in Figure 6-4, it is

Figure 6-5. Ring electrode imaginary–impedance–derived phase angle as a function of dimensionless frequency illustrating the frequency dispersion for dimensionless frequency K > 1. Impedance is shown for five radii ratios, r_1/r_2 and a disk electrode with $r_2 = 1.0$ cm for dimensionless frequency range: (A) 10 mHz to 10 Hz; (B) 100 mHZ to 1.8 Hz

difficult to compare ring geometries directly as this does not account for the physical and geometric parameters for each case.

The approximate characteristic length shown in Eq. 6–23 can be further improved upon by introducing a correction factor. The correction factor

$$ g = -2.2755x^6 + 5.1002x^5 - 3.4095x^4 - 0.5242x^3 + 1.6789x^2 - 0.7333x + 1 \qquad (6\text{–}24) $$

where $x = r_1/r_2$. This correction factor was obtained by fitting a polynomial to the data for different geometric ratios r_1/r_2 versus the characteristic length. Figure 6-6 shows how the approximate characteristic length Eq. (6–23) (red) compares to the simulated ring data (blue) and the polynomial fit of the simulated ring data (black).

Using the correction factor obtained from the polynomial fit, a more suitable dimensionless frequency is provided by K*. Dividing the characteristic length by g allows for the defining of a revised dimensionless frequency

$$ \mathrm{K}^* = \frac{\pi}{4} \frac{\omega \mathrm{C}_0}{\kappa} \left(\frac{r_2 - r_1}{1 + r_1^2/r_2^2} \right) \left(\frac{\ell_{c,ring}}{g} \right) \qquad (6\text{–}25) $$
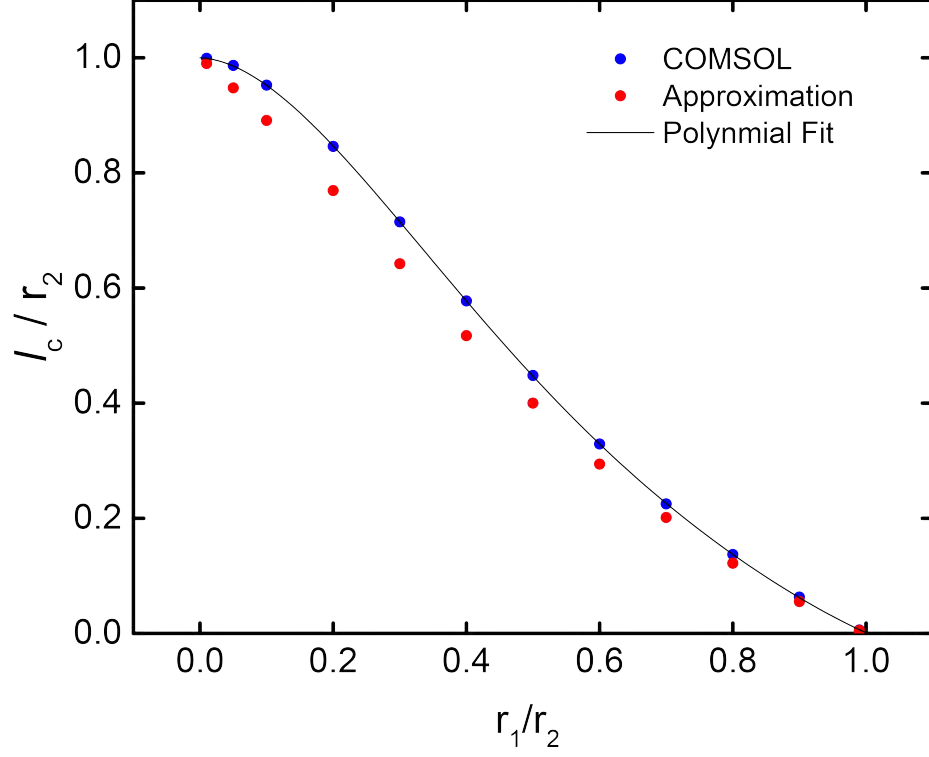
Figure 6-6. Characteristic length as a function of the geometric ratio r_1/r_2. COMSOL simulation results are shown in blue, empirical approximation Eq. (6–23) is in red, and polynomial fit is in black.

The ring electrode imaginary-impedance-derived phase angle as a function of dimensionless frequency, K^*, is provided in Figure 6-7. Similar to the previous figures, these represent impedance response and illustrating the frequency dispersion for dimensionless frequency $K^* > 1$. Unlike the previous figures, these provide for a more reasonable comparison. Specifically, the onset of frequency dispersion can be seen to occur for a dimensionless frequency $K^* > 1$ using an established characteristic length of $\ell_{c,ring}^*$.

A characteristic frequency of the ring electrode for each geometric ratio for the simulated ratios provided in Table 6-2 was found to range from 1 to 100. Figure 6-8A shows ratio of the characteristic frequency of the ring electrode $f_{c,ring}$ to the characteristic frequency of the disk electrode $f_{c,disk}$ as a function of the characteristic length $\ell_{c,ring}$ plotted on a log-scale. In these results the ring electrode has a characteristic frequency greater than the characteristic frequency of the disk for all geometric ratios.
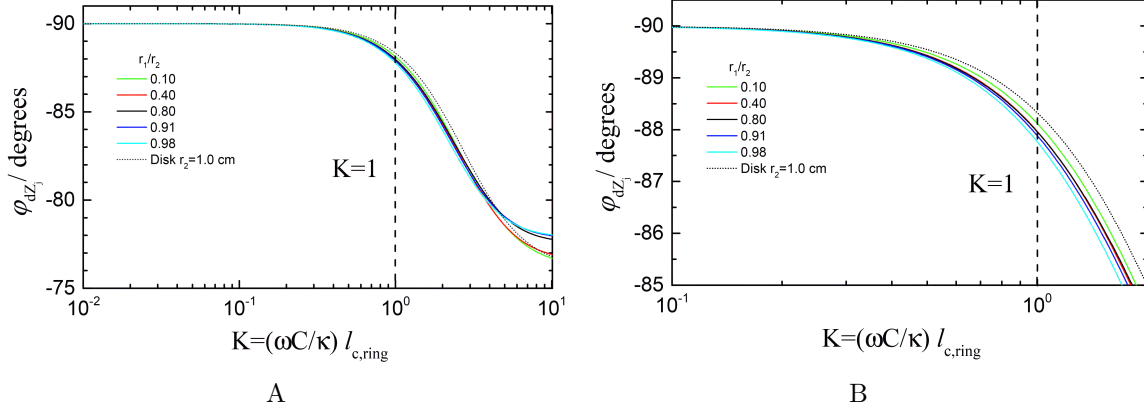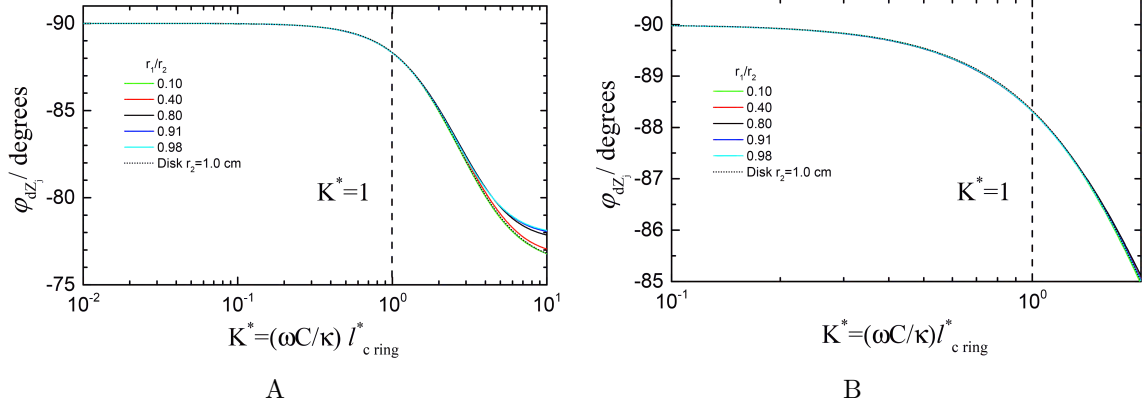
Figure 6-7. Ring electrode imaginary–impedance–derived phase angle as a function of dimensionless frequency illustrating the frequency dispersion for dimensionless frequency $K^* > 1$.
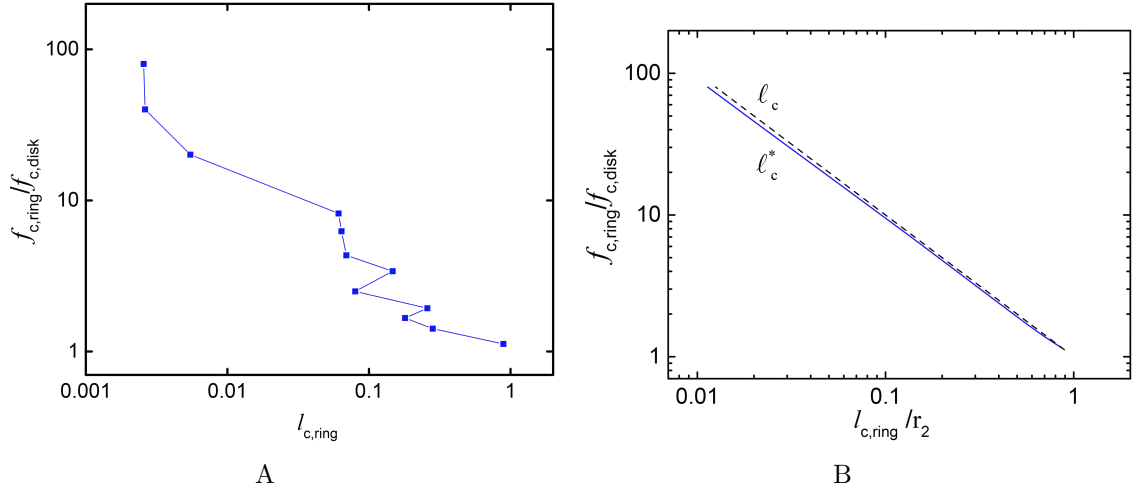
Figure 6-8. Ring electrode imaginary–impedance–derived phase angle as a function of dimensionless frequency illustrating the frequency dispersion for dimensionless frequency $K^* > 1$.

Another way to consider the same set of data is to plot it scaled by the outer radii of the disk, r_2. Figure 6-8B shows the ratio of the characteristic frequency of the ring electrode $f_{c,ring}$ to the characteristic frequency of the disk electrode $f_{c,disk}$ as a function of the characteristic length $\ell_{c,ring}$ and the corrected characteristic length $\ell^*_{c,ring}$ scaled by the outer radii of the disk, r_2. The result is a straight line for both the approximate characteristic length $\ell_{c,ring}$ and the corrected characteristic length $\ell^*_{c,ring}$.

95
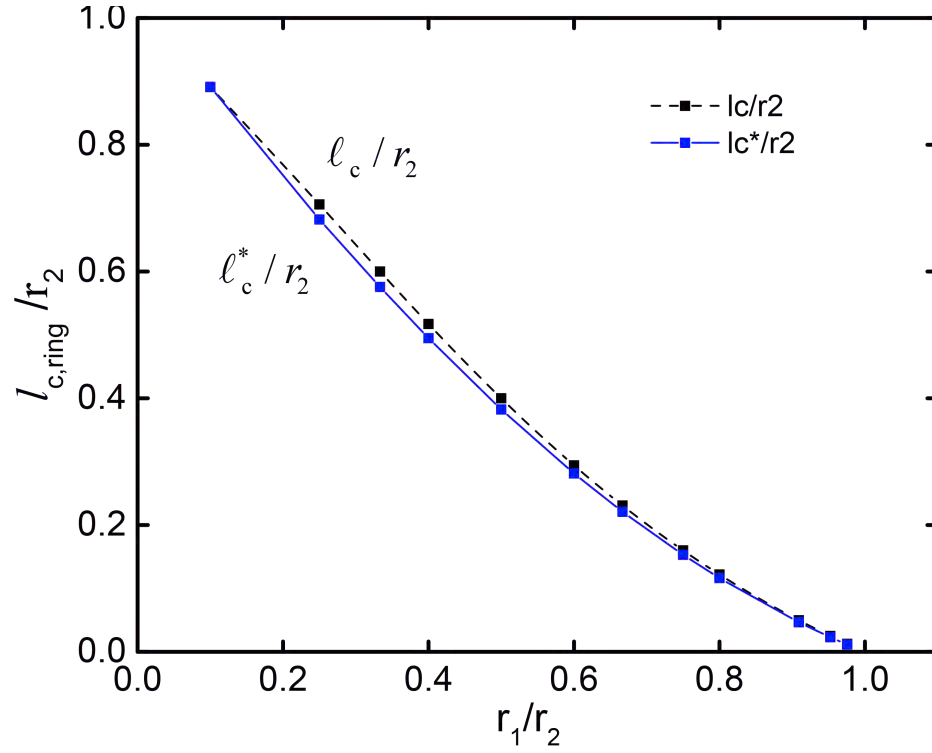
Figure 6-9. Ratio of the characteristic frequency of the ring electrode $f_{c,ring}$ to the characteristic frequency of the disk electrode $f_{c,disk}$ associated with the characteristic length $\ell_{c,ring}$ and the corrected characteristic length $\ell_{c,ring}^*$ scaled by the outer radii of the disk, r_2.

Figure 6-9 provides ratio of the characteristic frequency of the ring electrode fc,ring to the characteristic frequency of the disk electrode fc,disk associated with the characteristic length $\ell_{c,ring}$ lc,ring and the corrected characteristic length $\ell_{c,ring}^*$ scaled by the outer radii of the disk, r_2.

6.6   Concluding Remarks

The extent ring electrode geometry has on the frequency dispersion at high frequency was studied using finite element analysis for constant interfacial capacitance, electrolyte conductivity, and potential perturbation. Ratios of radii used in the numerical simulations were chosen to provide a range of results to assess the effect ring electrode geometry has on the impedance response. These scenarios included the limiting cases of a thin ring $r_1 \to r_2$, a thick ring $r_1 \to 0$ and intermediate geometric ratios.

Finite-element simulations were performed for different ring-electrode configurations to identify the frequency at which the electrode geometry causes frequency dispersion. Calculations were performed for uniform interfacial capacitance and electrolyte conductivity. An expression was developed for the characteristic dimension of the ring electrode. The frequency at which a ring electrode causes frequency dispersion was found to be larger than the frequency at which a disk of radius equal to the outer ring radius causes frequency dispersion. This work provides guidance to the development of impedance-based sensors employing ring geometries.

CHAPTER 7
CONCLUSIONS

A combination of impedance and polarization experiments and thermodynamic, kinetic, and impedance models were used to assess the tendency of copper to corrode in deaerated deionized water that did not contain hydrogen. The present work shows that copper will corrode at a very small rate. Kinetic simulations indicate that, for the present experimental conditions, the average rate over a period of one year would be on the order of 1 nm/day. The impedance analysis suggests that the corrosion rate is less than 2.5 nm/day. This corrosion rate will decrease as the concentration of hydrogen and copper increases. While the estimated corrosion rate may be inconsequential for most technological applications, the corrosion rate is large enough to influence the functionality of nanostructure utilized in emerging applications. Simulations performed for a microelectrode and copper foil showed that differences in estimated corrosion rates is the consequence of the different mass transfer rates and different electrode area to electrolyte volume ratios.

Finite-element simulations were performed for different ring-electrode configurations to identify the frequency at which the electrode geometry causes frequency dispersion. Calculations were performed for uniform interfacial capacitance and electrolyte conductivity. An expression was developed for the characteristic dimension of the ring electrode. The frequency at which a ring electrode causes frequency dispersion was found to be larger than the frequency at which a disk of radius equal to the outer ring radius causes frequency dispersion. This work provides guidance to the development of impedance-based sensors employing ring geometries.

CHAPTER 8
FUTURE WORK

The corrosion of copper microelectrodes at room temperature in deaerated water is presented in Chapter 4. Further work in the area of thermal corrosion could provide additional insight into the mechanism by which corrosion occurs. Experiments to measure the extent of copper corrosion under thermal cycling conditions were attempted by monitoring the OCP. These experiments were unsuccessful due to stability of the system at high temperate. The use of SEM images verified the presence of corrosion, however quantifying the corrosion rate was not possible by this method.

In Chapter 5 a refined kinetic model is developed to investigate the influence of mass transfer, surface area to volume ratio, exchange current density and equilibrium potential. For both the open and closed system kinetic models only consider the liquid phase dissolved gas concentration. Incorporating the liquid-gas equilibrium for the closed system and the dynamics of the liquid-gas exchange in the open system by accounting for the volume of overhead space would be interesting to investigate.

The geometric influence on the impedance response of a ring electrode are presented in Chapter 6. The presence of frequency dispersion in the ring electrode system is observed for dimensionless frequency greater than one. From these results a semi-imperical characteristic length was determined based on the ring band thickness and a correction factor. A closed form expression that holds for all geometric parameters could not be found. It would be convenient to develop an expression that is valid for all geometric parameters.

REFERENCES

[1] C. Cleveland, S. Moghaddam, and M. E. Orazem, "Nanometer-Scale Corrosion of Copper in De-Aerated Deionized Water," *Journal of the Electrochemical Society*, **161** (2014) C107–C114.

[2] G. Hultquist, P. S. I. Szakálos, M. J. Graham, G. I. Sproule, and G. Wikmark, "Detection of Hydrogen in Corrosion of Copper in Pure Water," in *Proceedings of the 2008 International Corrosion Congress*, Paper 3884 (2008) 1–9.

[3] Y. Zhao, D. Ye, G. Wang, and T. Lu, "Designing nanostructures by glancing angle deposition," in *Proceedings of SPIE*, volume 5219 (Citeseer, 2003) 59–73.

[4] A. Majumdar, R. Karnik, and W. Kim, "NANOSTRUCTURED MICRO HEAT PIPES," (2006). US Patent App. 12/063,226.

[5] J. P. McHale, S. V. Garimella, T. S. Fisher, and G. A. Powell, "Pool Boiling Performance Comparison of Smooth and Sintered Copper Surfaces with and Without Carbon Nanotubes," *Nanoscale and Microscale Thermophysical Engineering*, **15** (2011) 133–150.

[6] Y. S. Ju, M. Kaviany, Y. Nam, S. Sharratt, G. Hwang, I. Catton, E. Fleming, and P. Dussinger, "Planar Vapor Chamber with Hybrid Evaporator Wicks for the Thermal Management of High-Heat-Flux and High-Power Optoelectronic Devices," *International Journal of Heat and Mass Transfer*, **60** (2013) 163 – 169.

[7] S. Tao and D. Y. Li, "Nanocrystallization effect on the surface electron work function of copper and its corrosion behaviour," *Philosophical Magazine Letters*, **88** (2008) 137–144.

[8] K. Amaya, J. Togashi, and S. Aoki, "Inverse Analysis of Galvanic Corrosion - Using Fuzzy a-Priori Information," *JSME International Journal Series A: Mechanics and Material Engineering*, **38** (1995) 541–546.

[9] M. G. Fontana, *Corrosion Engineering*, 3rd edition (New York: McGraw Hill, 1986).

[10] G. Pantazopoulos, "Metallurgical Observations on Fatigue Failure of a Bent Copper Tube," *Journal of Failure Analysis and Prevention*, **9** (2009) 270–274.

[11] J. Newman and K. Thomas-Alyea, *Electrochemical Systems* (Wiley Hoboken, NJ, 2004).

[12] J. C. Rushing and M. Edwards, "The role of temperature gradients in residential copper pipe corrosion," *Corrosion Science*, **46** (2004) 1883–1894. Temperature gradients;Thermogalvanic currents;.

[13] D. S. Carr and C. F. Bonilla, "Thermogalvanic Potentials," *Journal of the Electrochemical Society*, **99** (1952) 475–482.

[14] H. Lal and H. R. Thirsk, "The Anodic Behaviour of Copper in Neutral and Alkaline Chloride Solutions," *Journal of the Chemical Society (Resumed)*, (1953) 2638–2644.

[15] T. Hurlen, "Dissolution of Copper by Oxidation Agents in Acid Chloride Solution," *Acta. Chem. Scand*, **15** (1961) 1239–1245.

[16] N. Berry, ""Thermogalvanic" corrosion," *Nanostructured Materials and Nanotechnology Ii*, **2** (1946) 261 – 267.

[17] M. Braun and K. Nobe, "Electrodissolution Kinetics of Copper in Acidic Chloride Solutions," *Journal of the Electrochemical Society*, **126** (1979) 1666–1671.

[18] A. L. Bacarella and J. J. C. Griess, "The Anodic Dissolution of Copper in Flowing Sodium Chloride Solutions Between 25° and 175°C," *Journal of the Electrochemical Society*, **120** (1973) 459–465.

[19] F. King, M. Quinn, and C. D. Litke, "Oxygen Reduction on copper in neutral Nacl solution," *Journal of Electroanalytical Chemistry*, **385** (1995) 45–55.

[20] T. N. Andersen, M. H. Ghandehari, and H. Eyring, "A Limitation to the Mixed Potential Concept of Metal Corrosion," *Journal of the Electrochemical Society*, **122** (1975) 1580–1585.

[21] A. Jardy, A. L. Lasalle-Molin, M. Keddam, and H. Takenouti, "Copper Dissolution in Acidic Sulphate Media Studied by QCM and RRDE under AC Signal," *Electrochimica Acta*, **37** (1992) 2195–2201.

[22] S. T. Mayer and R. H. Muller, "An In Situ Raman Spectroscopy Study of the Anodic Oxidation of Copper in Alkaline Media," *Journal of the Electrochemical Society*, **139** (1992) 426–434.

[23] B. Miller, "Split-Ring Disk Study of the Anodic Processes at a Copper Electrode in Alkaline Solution," *Journal of the Electrochemical Society*, **116** (1969) 1675–1680.

[24] C. B. Diem, *The Influence of Velocity on the Corrosion of Copper in Alkaline Chloride Solutions*, Ph.D. dissertation, University of Virginia, Charlottesville, Virginia (1990).

[25] N. Mora, E. Cano, E. M. Mora, and J. M. Bastidas, "Influence of pH and Oxygen on Copper Corrosion in Simulated Uterine Fluid," *Biomaterials*, **23** (2002) 667–671.

[26] C. B. Diem and M. E. Orazem, "The Influence of Velocity on the Corrosion of Copper in Alkaline Chloride Solutions," *Nanostructured Materials and Nanotechnology Ii*, **50** (1994) 290–300.

[27] C. B. Diem and M. E. Orazem, "The Corrosion of Copper in Flowing Alkaline Chloride Solutions," in *Velocity Enhanced Corrosion*, K. J. Kennelley, R. H. Hausler, and D. Silverman, editors (Houston, Texas: National Association of Corrosion Engineers, 1991) 23:1–23:15.

[28] C. H. Bonfigkio, H. C. Albaya, and O. A. Cobo, "The Kinetics of the Anodic Dissolutions of Copper in Aicd Chloride Solutions," *Corr. Sci.*, **13** (1973) 717–724.

[29] P. Agarwal, O. C. Moghissi, M. E. Orazem, and L. H. García-Rubio, "Application of Measurement Models for Analysis of Impedance Spectra," *Nanostructured Materials and Nanotechnology Ii*, **49** (1993) 278–289.

[30] M. Pourbaix, *Atlas of Electrochemical Equilibria in Aqueous Solutions* (Houston, Texas, USA: NACE International: The Corrosion Society, 1974).

[31] D. M. Bastidas, E. Cano, and E. Mora, "Influence of Oxygen, Albumin and pH on Copper Dissolution in a Simulated Uterine Fluid," *European J. of Contraception and Reproductive Healthcare*, **10** (2005) 123–130.

[32] J. Zhu, N. Xu, and C. Zhang, "Characteristics of copper corrosion in simulated uterine fluid in the presence of protein," *Advances in contraception*, **15** (1999) 179–190.

[33] F. King, L. Ahonen, C. Taxen, U. Vuorinen, and L. Werme, *Copper corrosion under expected conditions in a deep geologic repository*, Technical Report TR-01-23, Swedish Nuclear Fueland Waste Management Co, Swedish Nuclear Fuel and Waste Management Co, Box 5864, SE-102 40 Stockholm Sweden (2001).

[34] Y. Feng, W.-K. Teo, K.-S. Siow, K. l. Tan, and A.-K. Hsieh, "The corrosion behaviour of copper in neutral tap water. Part I: Corrosion mechanisms," *Corrosion Science*, **38** (1996) 369 – 385.

[35] G. Hultquist, G. Chuah, and K. Tan, "Comments on hydrogen evolution from the corrosion of pure copper," *Corrosion Science*, **29** (1989) 1371 – 1377.

[36] G. Hultquist, M. Graham, P. Szakalos, G. Sproule, A. Rosengren, and L. Gråsjö, "Hydrogen Gas Production During Corrosion of Copper by Water," *Corros. Sci.*, **53** (2011) 310–319.

[37] G. Hultquist, P. Szakalos, M. Graham, A. B. Belonoshko, G. Sproule, L. Gråsjö, P. Dorogokupets, B. Danilov, T. AAstrup, G. Wikmark, *et al.*, "Water corrodes copper," *Catalysis Letters*, **132** (2009) 311–316.

[38] F. King and C. Lilja, "Scientific basis for corrosion of copper in water and implications for canister lifetimes," *Corrosion Engineering, Science and Technology*, **46** (2011) 153–158.

[39] P. Szakalos, G. Hultquist, and G. Wikmark, "Corrosion of copper by water," *Electrochemical and Solid-State Letters*, **10** (2007) C63–C67.

[40] D. D. Macdonald and S. Sharifi-Asl, *Is Copper Immune to Corrosion When in Contact with Water and Aqueous Solutions*, Technical Report TR-01-23, Swedish Radiation Safety Authority, Swedish Nuclear Fuel and Waste Management Co Box 5864 SE-102 40 Stockholm Sweden (2011).

[41] M. E. Orazem and B. Tribollet, *Electrochemical Impedance Spectroscopy* (Hoboken, NJ: John Wiley & Sons, 2008).

[42] S.-L. Wu, *Influence of Disk Electrode Geometry on Local and Global Impedance Response*, Ph.D. dissertation, University of Florida, Gainesville, FL (2010).

[43] E. Patrick, M. E. Orazem, J. C. Sanchez, and T. Nishida, "Corrosion of Tungsten Microelectrodes used in Neural Recording Applications," *Journal Of Neuroscience Methods*, **198** (2011) 158–171.

[44] A. Bar-Cohen and P. Wang, "Thermal Management of On-Chip Hot Spot," *J. Heat Transfer*, **134** (2012).

[45] S. V. Garimella and C. Sobhan, "Recent Advances in the Modeling and Applications of Nonconventional Heat Pipes," *Advances in Heat Transfer*, **35** (2001) 249–308.

[46] S. P. Gurrum, S. K. Suman, Y. K. Joshi, and A. G. Fedorov, "Thermal issues in next-generation integrated circuits," *Device and Materials Reliability, IEEE Transactions on*, **4** (2004) 709–714.

[47] M. Groll, M. Schneider, V. Sartre, M. Chaker Zaghdoudi, and M. Lallemand, "Thermal Control of Electronic Equipment by Heat Pipes," *Revue générale de thermique*, **37** (1998) 323–352.

[48] C. Zhang, *Analytical and Experimental Investigation of Capillary Forces Induced by Nanopillars for Thermal Management Applications*, Ph.D. dissertation, University of Texas (2010).

[49] R. Chen, M.-C. Lu, V. Srinivasan, Z. Wang, H. H. Cho, and A. Majumdar, "Nanowires for Enhanced Boiling Heat Transfer," *Nano Lett.*, **9** (2009) 548–553.

[50] A. S. Kousalya, J. A. Weibel, S. V. Garimella, and T. S. Fisher, "Metal Functionalization of Carbon Nanotubes for Enhanced Sintered Powder Wicks," *Int. J. Heat Mass Tran.*, **59** (2013) 372–383.

[51] R. W. Knight, D. Hall, J. Goodling, and R. Jaeger, "Heat Sink Optimization with Application to Microchannels," *Components, Hybrids, and Manufacturing Technology, IEEE Transactions on*, **15** (1992) 832–842.

[52] D. B. Tuckerman and R. Pease, "High-Performance Heat Sinking for VLSI," *Electron Device Letters, IEEE*, **2** (1981) 126–129.

[53] M. Bowers and I. Mudawar, "High Flux Boiling in Low Flow Rate, Low Pressure Drop Mini-Channel and Micro-Channel Heat Sinks," *Int. J. Heat Mass Tran.*, **37** (1994) 321–332.

[54] R. Chein and G. Huang, "Analysis of Microchannel Heat Sink Performance Using Nanofluids," *Appl Therm Eng*, **25** (2005) 3104–3114.

[55] S. P. Jang and S. U. Choi, "Cooling Performance of a Microchannel Heat Sink with Nanofluids," *Appl Therm Eng*, **26** (2006) 2457–2463.

[56] C.-J. Ho, L. Wei, and Z. Li, "An Experimental Investigation of Forced Convective Cooling Performance of a Microchannel Heat Sink With Al_2O_3/Water Nanofluid," *Appl Therm Eng*, **30** (2010) 96–103.

[57] O. E. Barcia, O. R. Mattos, N. Pébère, and B. Tribollet, "Mass-Transport Study for the Electrodissolution of Copper in 1M Hydrochloric Acid Solution by Impedance," *Journal of the Electrochemical Society*, **140** (1993) 2825–2832.

[58] K. D. Efird, "Effect of Fluid Dynamics on the Corrosion of Copper-Based Alloys in Seawater," *Nanostructured Materials and Nanotechnology Ii*, **33** (1977) 3–8.

[59] J. S. Newman and K. E. Thomas-Alyea, *Electrochemical Systems*, 3rd edition (Hoboken, NJ: John Wiley & Sons, 2004).

[60] M. Bojinov, I. Betova, and C. Lilja, "A Mechanism of Interaction of Copper with a Deoxygenated Neutral Aqueous Solution," *Corrosion Science*, **52** (2010) 2917–2927.

[61] M. Bojinov, T. Laitinen, K. Mkel, M. Snellman, and L. Werme, "Corrosion of Copper in 1 M NaCl under Strictly Anoxic Conditions," *MRS Proceedings*, **807** (2003) 459–464.

[62] S. Sharifi-Asla and D. D. Macdonald, "Investigation of the Kinetics and Mechanism of the Hydrogen Evolution Reaction on Copper," *Journal of the Electrochemical Society*, **160** (2013) H382–H391.

[63] R. Dortwegt and E. Maughan, "The Chemistry of Copper in Water and Related Studies Planned at the Advanced Photon Source," in *Particle Accelerator Conference, 2001. PAC 2001. Proceedings of the 2001*, volume 2 (IEEE, 2001) 1456–1458.

[64] R. Dortwegt, C. Putnam, and E. Swetin, "Mitigation of Copper Corrosion and Agglomeration in APS Process Water Systems," in *2nd Intl Workshop on Mechanical Engineering Design of Synchrotron Radiation Equipment and Instrumentation (MEDSI2002)* (2002) 462–468.

[65] M. Parro, P. Karditsas, A. Caloutsis, D. Iglesias, B. Brañas, and A. Abánades, "Corrosion and Activation Analysis of the LIPAC Beam Dump Cooling Circuit," *Fusion Eng. Des.*, (2013).

[66] J. S. Newman, "Resistance for Flow of Current to a Disk," *Journal of the Electrochemical Society*, **113** (1966) 501–502.

[67] A. Anderko and P. J. Shuler, "A Computational Approach to Predicting the Formation of Iron Sulfide Species Using Stability Diagrams," *Computers & Geosciences*, **23** (1997) 647–658.

[68] A. Anderko, S. J. Sanders, and R. D. Young, "Real Solution Stability Diagrams: A Thermodynamic Tool for Modeling Corrosion in Wide Temperature and Concentration Ranges," *Corrosion*, **53** (1997) 43–53.

[69] B. Beverskog and I. Puigdomenech, "Revised Pourbaix Diagrams for Copper at 25 to 300 °C," *Journal of the Electrochemical Society*, **144** (1997) 3476–3483.

[70] P. Mahon and K. Oldham, "Diffusion-controlled chronoamperometry at a disk electrode," *Analytical Chemistry*, **77** (2005) 6100–6101.

[71] Z. Stanković and M. Vuković, "The Influence of Thiourea on Kinetic Parameters on the Cathodic and Anodic Reaction at Different Metals in H_2SO_4 Solution," *Electrochim. Acta*, **41** (1996) 2529–2535.

[72] M. Stern and A. L. Geary, "Electrochemical Polarization: I. A Theoretical Analysis of the Shape of Polarization Curves," *Journal of the Electrochemical Society*, **104** (1957) 56–63.

[73] P. Agarwal, M. E. Orazem, and L. H. García-Rubio, "Measurement Models for Electrochemical Impedance Spectroscopy: 1. Demonstration of Applicability," *Journal of the Electrochemical Society*, **139** (1992) 1917–1927.

[74] G. J. Brug, A. L. G. van den Eeden, M. Sluyters-Rehbach, and J. H. Sluyters, "The Analysis of Electrode Impedances Complicated by the Presence of a Constant Phase Element," *Journal of Electroanalytical Chemistry*, **176** (1984) 275–295.

[75] V. M.-W. Huang, V. Vivier, I. Frateur, M. E. Orazem, and B. Tribollet, "The Global and Local Impedance Response of a Blocking Disk Electrode with Local CPE Behavior," *Journal of the Electrochemical Society*, **154** (2007) C89–C98.

[76] B. Hirschorn, M. E. Orazem, B. Tribollet, V. Vivier, I. Frateur, and M. Musiani, "Determination of Effective Capacitance and Film Thickness from CPE Parameters," *Electrochimica Acta*, **55** (2010) 6218–6227.

[77] B. Hirschorn, M. E. Orazem, B. Tribollet, V. Vivier, I. Frateur, and M. Musiani, "Constant-Phase-Element Behavior Caused by Resistivity Distributions in Films: 1. Theory," *Journal of the Electrochemical Society*, **157** (2010) C452–C457.

[78] B. Hirschorn, M. E. Orazem, B. Tribollet, V. Vivier, I. Frateur, and M. Musiani, "Constant-Phase-Element Behavior Caused by Resistivity Distributions in Films: 2. Applications," *Journal of the Electrochemical Society*, **157** (2010) C458–C463.

[79] M. E. Orazem, B. Tribollet, V. Vivier, S. Marcelin, N. Pébère, A. L. Bunge, E. A. White, D. P. Riemer, I. Frateur, and M. Musiani, "Dielectric Properties of Materials showing Constant-Phase-Element (CPE) Impedance Response," *Journal of the Electrochemical Society*, **160** (2013) C215–C225.

[80] W. M. Haynes, T. J. Bruno, and D. R. Lide, editors, *CRC Handbook of Chemistry and Physics*, 94th edition (CRC Press, 2014).

[81] R. Bogdanowicz, J. Ryl, K. Darowicki, and B. B. Kosmowski, "Ellipsometric Study of Oxide Formation on Cu Electrode in 0.1 M NaOH," *Journal of Solid State Electrochemistry*, **13** (2009) 1639–1644.

[82] Z. D. Stanković and M. Vuković, "The Influence of Thiourea On Kinetic Parameters on the Cathodic and Anodic Reaction at Different Metals in H_2SO_4 Solution," *Electrochimica Acta*, **41** (1996) 2529–2535.

[83] R. Sander, "Henry's Law Constants," in *NIST Chemistry WebBook, NIST Standard Reference Database Number 69*, P. Linstrom and W. Mallard, editors (Gaithersburg MD: National Institute of Standards and Technology) http://webbook.nist.gov. Retrieved November 4, 2015.

[84] H. C. Hottel, J. J. Noble, A. F. Sarofim, G. D. Sikox, P. C. Wankat, and K. S. Knaebel, "Heat and Mass Transfer," in *Perry's Chemical Engineers' Handbook*, D. W. Green and R. H. Perry, editors, 8th edition (New York, NY: McGraw-Hill, 2007) 5:1–5:84.

[85] C. R. Wilke, M. Eisenberg, and C. W. Tobias, "Correlation of Limiting Currents under Free Convection Conditions," *Journal of The Electrochemical Society*, **100** (1953) 513–523.

[86] G. Hultquist, M. Graham, O. Kodra, S. Moisa, R. Liu, U. Bexell, and J. Smialek, "Corrosion of Copper in Distilled Water without O_2 and the Detection of Produced Hydrogen," *Corrosion Science*, **95** (2015) 162–167.

[87] V. M.-W. Huang, V. Vivier, M. E. Orazem, N. Pébère, and B. Tribollet, "The Apparent CPE Behavior of a Disk Electrode with Faradaic Reactions," *Journal of the Electrochemical Society*, **154** (2007) C99–C107.

[88] J. S. Newman, "Frequency Dispersion in Capacity Measurements at a Disk Electrode," *Journal of the Electrochemical Society*, **117** (1970) 198–203.

[89] C. L. Alexander, B. Tribollet, and M. E. Orazem, "Contribution of Surface Distributions to Constant-Phase-Element (CPE) Behavior: 1. Influence of Roughness," *Electrochimica Acta*, **173** (2015) 416–424.

[90] V. M.-W. Huang, V. Vivier, M. E. Orazem, N. Pébère, and B. Tribollet, "The Apparent CPE Behavior of an Ideally Polarized Disk Electrode: A Global and Local Impedance Analysis," *Journal of the Electrochemical Society*, **154** (2007) C81–C88.

[91] C. Blanc, M. Orazem, N. Pbre, B. Tribollet, V. Vivier, and S. Wu, "The Origin of the Complex Character of the Ohmic Impedance," *Electrochimica Acta*, **55** (2010) 6313–6321.

[92] C. L. Alexander, B. Tribollet, and M. E. Orazem, "Contribution of Surface Distributions to Constant-Phase-Element (CPE) Behavior: 2. Capacitance," *Electrochimica Acta*, (2015) submitted.

[93] A. Frumkin, L. Nekrasov, B. Levich, and J. Ivanov, "Die Anwendung der rotierenden Scheibenelektrode mit einem Ringe zur Untersuchung von Zwischenprodukten elektrochemischer Reaktionen," *Journal of Electroanalytical Chemistry (1959)*, **1** (1959) 84–90.

[94] A. Frumkin and L. Nekrasov, "On the Ring-Disk Electrode," in *Dokl. Akad. Nauk. SSSR*, volume 126 (1959) 115–118.

[95] I. Ivanov and V. Levich, "Investigation of Unstable Intermediary Production of the Electrode Reaction by Means of a Rotating Disk Electrode," *Doklady Akademii Nauk SSSR*, **126** (1959) 1029–1032.

[96] W. Albery and S. Bruckenstein, "Ring-disc electrodes. Part 2.Theoretical and Experimental Collection Effciencies," *Transactions of the Faraday Society*, **62** (1965) 1920–1931.

[97] W. H. Smyrl and J. S. Newman, "Ring-Disk and Sectioned Disk Electrode," *Journal of the Electrochemical Society*, **119** (1972) 212–219.

[98] J. Joseph J. Miksis and J. S. Newman, "Primary Resistances for Ring-Disk Electrodes," *Journal of the Electrochemical Society*, **123** (1976) 1030–1036.

[99] P. Pierini and J. S. Newman, "Current Distribution on a Rotating Ring-Disk Electrode below the Limiting Current," *Journal of the Electrochemical Society*, **124** (1977) 701–706.

[100] D. Gregory and A. Riddiford, "Dissolution of Copper in Sulfuric Acid Solutions," *Journal of the Electrochemical Society*, **107** (1960) 950–956.

[101] D. Gregory and A. Riddiford, "Transport to the Surface of a Rotating Disc," *Journal of the Chemical Society*, (1956) 3756–3764.

[102] V. G. Levich, *Physicochemical Hydrodynamics* (Englewood Cliffs, NJ: Prentice Hall, 1962).

[103] P. Pierini and J. S. Newman, "Ring Electrodes," *Journal of the Electrochemical Society*, **125** (1978) 79–84.

[104] W. Albery, J. Drury, and A. Hutchinson, "Ring Disc Electrodes. Part 15.Alternating Current Measurements," *Transactions of the Faraday Society*, **67** (1971) 2414–2418.

[105] W. Albery, A. Davis, and A. Mason, "Alternating Current and Ring-Disc Electrodes," *Faraday Discussions of the Chemical Society*, **56** (1973) 317–329.

[106] I. Annergren, M. Keddam, H. Takenouti, and D. Thierry, "Modelling of the Passivation Mechanism of Fe-Cr Binary Alloys from AC Impedance and Frequency Resolved RRDE: I. Behaviour of Fe-Cr Alloys in 0.5 M H_2SO_4," *Electrochimica acta*, **41** (1996) 1121–1135.

[107] I. Annergren, M. Keddam, H. Takenouti, and D. Thierry, "Modeling of the Passivation Mechanism of Fe-Cr Binary Alloys from Ac Impedance and Frequency Resolved RRDE: II. Behavior Of Fe-Cr Alloys In 0.5 M H_2SO_4 with an Addition of Chloride," *Electrochimica Acta*, **42** (1997) 1595–1611.

[108] C. Bünzli, H. Kaiser, and P. Novák, "Important Aspects for Reliable Electrochemical Impedance Spectroscopy Measurements of Li-Ion Battery Electrodes," *Journal of The Electrochemical Society*, **162** (2015) A218–A222.

[109] M. Chatenet, M. Molina-Concha, N. El-Kissi, G. Parrour, and J.-P. Diard, "Direct Rotating Ring-Disk Measurement of the Sodium Borohydride Diffusion Coefficient in Sodium Hydroxide Solutions," *Electrochimica Acta*, **54** (2009) 4426–4435.

[110] C. Gabrielli, M. Keddam, F. Minouflet-Laurent, and H. Perrot, "Simultaneous EQCM and Ring-Disk Measurements in AC Regime Application to Copper Dissolution," *Electrochemical and solid-state letters*, **3** (2000) 418–421.

[111] M. Cimenti, A. Co, V. Birss, and J. Hill, "Distortions in Electrochemical Impedance Spectroscopy Measurements Using 3-electrode Methods In SOFC: 1. Effect of Cell Geometry," *Fuel Cells*, **7** (2007) 364 – 376. 3-electrode configuration;Area-specific polarisation resistances;Electrode geometry;Impedance distortions;Reference electrodes;.

[112] M. Cimenti, V. Birss, and J. Hill, "Distortions in Electrochemical Impedance Spectroscopy Measurements Using 3-electrode Methods In SOFC: 2. Effect of Electrode Activity and Relaxation Times," *Fuel Cells*, **7** (2007) 377 – 391. 3-electrode configuration;Planar cells;Reference electrodes;.

[113] W. Besio and A. Prasad, "Analysis of Skin-Electrode Impedance using Concentric Ring Electrode," in *Engineering in Medicine and Biology Society, 2006. EMBS'06. 28th Annual International Conference of the IEEE* (IEEE, 2006) 6414–6417.

[114] K.-M. Hsieh, K.-C. Lan, W.-L. Hu, M.-K. Chen, L.-S. Jang, and M.-H. Wang, "Glycated Hemoglobin (HbA 1c) Affinity Biosensors with Ring-Shaped Interdigital Electrodes on Impedance Measurement," *Biosensors and Bioelectronics*, **49** (2013) 450–456.

[115] X. F. Wei and W. M. Grill, "Current Density Distributions, Field Distributions and Impedance Analysis of Segmented Deep Brain Stimulation Electrodes," *Journal of Neural Engineering*, **2** (2005) 139.

[116] S. P. Jiang, "Thermally and Electrochemically Induced Electrode/Electrolyte Interfaces in Solid Oxide Fuel Cells: An AFM and EIS Study," *Journal of The Electrochemical Society*, **162** (2015) F1119–F1128.

[117] N. Kovács, M. Ujvári, G. G. Láng, P. Broekmann, and S. Vesztergom, "Characterization of the Capacitance of a Rotating Ring-Disk Electrode," *Instrumentation Science & Technology*, (2015).

[118] J. Nielsen and T. Jacobsen, "Current Distribution Effects in AC Impedance Spectroscopy of Electroceramic Point Contact and Thin Film Model Electrodes," *Electrochimica Acta*, **55** (2010) 6248–6254.

[119] S. Bruckenstein and G. Martinchek, "A Closed Form Expression for the Primary Resistance at a Ring Electrode," *Journal of The Electrochemical Society*, **126** (1979) 1307–1309.

[120] D. E. Gray, *American Institute of Physics Handbook* (McGraw-Hill, 1972).

BIOGRAPHICAL SKETCH

Christopher Cleveland matriculated at the University of St. Thomas in St. Paul, Minnesota, in August of 2005, where he graduated with honors earning his Bachelor of Science in chemistry and Bachelor of Arts in mathematics in May of 2008. Following this, Chris attended Carnegie Mellon University where he received his Master of Science in chemical engineering in May of 2010. Under the direction of Professor Mark E. Orazem, Chris has investigated the corrosion of copper in deaerated water and will receive his Doctor of Philosophy from the University of Florida in May 2017.